



# Single-atom-focused laser for photon generation and qubit control

A master's thesis submitted to the faculty of mathematics, computer science  
and physics, of the University of Innsbruck  
in partial fulfillment of the requirements for the degree of

**Master of Science (MSc)**

carried out at the Institute of Experimental Physics under the supervision of  
Dr. Ben Lanyon  
o.Univ.-Prof. Dr. Rainer Blatt,

Presented by

**Marco Canteri**



# Abstract

An ongoing project of building a three node quantum network is currently being carried out at the university of Innsbruck with ion traps being the nodes of the network. The ion traps all feature an integrated optical cavity for enhanced photon collection efficiency. To make entanglement between ions located in the three nodes, control over multiple ion-photon pairs is required in at least one of the nodes. In this thesis I present the design and implementation of a tightly-focused laser system that allows many ions in a string to be connected with many propagating photons. The optical system focuses a 393 nm laser down to address individual ions in the string and uses an acousto-optic deflector (AOD) for steering the focus to different ions in a string on the microsecond timescale. Our experiment traps  $^{40}\text{Ca}^+$  ions, the 393 nm laser triggers the generation of a photon via a cavity enhanced Raman process. The photon is emitted in a cavity and leaks out from one side. The designed setup comprises of an AOD, for steering the beam on the microsecond timescale, a set of lenses for expansion and control of the laser beam, and a custom objective for focusing the light on the ions. The system was designed and simulated with the software Zemax, and ultimately built on top of the existing experiment. We report two experiments that demonstrate the capabilities of the setup. The first experiment generated photons from a single ion in a string without changing the state of the other ions. In the second experiment we applied a phase gate on a single ion-qubit, the phase shift induced is measured with a Ramsey interferometer. In addition to realizing single qubit manipulation capability in our ion-trap for the first time, this experiment allowed for a measure of the focus spot:  $1.2\text{-}1.3 \mu\text{m}$  ( $1/e^2$  intensity radius) with an upper bound on the addressing error of  $10^{-2}$  for a 4 ion string confined with a trap frequency of 767 kHz. These experiments are a stepping stone towards the realization of the aforementioned quantum network, the next key experiment is already ongoing, photons are produced from different ions creating a photon train. Afterwards, entanglement between ion and photon has to be achieved for each ion-photon pair.



# Contents

<b>1</b>	<b>Introduction</b>	<b>1</b>
<b>2</b>	<b>Theoretical framework</b>	<b>5</b>
2.1	Quantum logic with trapped ions . . . . .	5
2.1.1	Quantum computer and quantum gates . . . . .	5
2.1.2	Ion qubits and laser-ion interactions . . . . .	7
2.1.2.1	Three-level model . . . . .	10
2.1.2.2	Dissipative processes . . . . .	12
2.2	Quantum networking with trapped ions . . . . .	12
2.2.1	General introduction . . . . .	12
2.2.2	Cavity QED . . . . .	13
2.2.3	Photon generation . . . . .	14
2.3	Basics of ion trapping . . . . .	15
2.3.1	Linear Paul trap . . . . .	15
2.3.2	Ion strings . . . . .	17
2.3.3	Doppler cooling . . . . .	18
2.4	Laser beam . . . . .	19
2.4.1	Gaussian beams . . . . .	19
2.4.2	Beam steering via Acousto-optical Deflectors . . . . .	22
2.5	Basic model of key experiments . . . . .	24
2.5.1	Addressed qubit manipulation . . . . .	24
2.5.2	Addressed photon generation . . . . .	26
<b>3</b>	<b>Experimental system and techniques</b>	<b>27</b>
3.1	Ion trap and key techniques . . . . .	27
3.1.1	Calcium Ions . . . . .	27
3.1.2	Trapping, cooling, and state readout . . . . .	28
3.2	393 nm laser . . . . .	30
3.3	Experiment control . . . . .	31
<b>4</b>	<b>Design and simulation of the addressing setup</b>	<b>33</b>
4.1	Addressing system overview and requirements . . . . .	33
4.2	Objective and AOD . . . . .	35
4.3	Design simulation . . . . .	36
4.4	Physical implementation . . . . .	40
<b>5</b>	<b>Experimental results</b>	<b>43</b>
5.1	AOD . . . . .	43

5.2	Full test setup characterization . . . . .	44
5.2.1	Waist: Knife-Edge method . . . . .	45
5.2.2	Waist: Camera . . . . .	47
5.2.3	Polarization . . . . .	48
5.2.4	Stability . . . . .	48
5.3	Final installed system . . . . .	50
5.3.1	Single qubit manipulation . . . . .	50
5.3.2	Photon production . . . . .	54
<b>6</b>	<b>Conclusions and outlook</b>	<b>57</b>
	References . . . . .	59
	<b>Appendix</b>	<b>64</b>
<b>A</b>	<b>AOD datasheet</b>	<b>65</b>
<b>B</b>	<b>Polarization characterization</b>	<b>69</b>

# Chapter 1

## Introduction

Quantum technology offers radically new approaches for the fields of computation, communication, simulation, and metrology [1]. For example, classical computers are limited in solving a range of important problems such a factorization, due to an exponential increase in computing time with the problem size. Quantum computers, however, exploit particular features of quantum mechanics that have no classical counterparts to solve the factorization problem with sub-exponential resources in problem size [2]. Moreover, simulating nature at its quantum level is a hard task for a classical computer, while quantum computers are naturally prone to the efficient simulation of quantum dynamics [3].

A collection of distributed *nodes*, that are each quantum computers, that are interconnected via quantum channels forms a fully fledged quantum network [4]. However, for some quantum network applications, it is possible to relax the condition of having a universal quantum computer at each node, a quantum device with a single qubit is enough as part of a functional quantum network with basic capabilities. As such, quantum networks are likely to provide some of the first practical applications of quantum technology [5]. There are fundamental differences between a quantum channel and a classical one. Although the medium can be the same, such as optical fiber, a quantum channel must have additional abilities, such as distributing entanglement, or transmitting quantum states.

Quantum networks have several applications: cryptographic-wise they allow for more secure information transmission through Quantum Key Distribution [6], secure identification [7], blind quantum computation [8] and more [5]. Outside cryptography, quantum networks find applications in metrology: entanglement can be exploited to improve clock synchronization [9], and extend telescope's baselines [10]. Furthermore, quantum networks offer more efficient solutions to distributed system problems [11], and a distributed network of quantum processors is a practical way to enable scalable quantum computing [12].

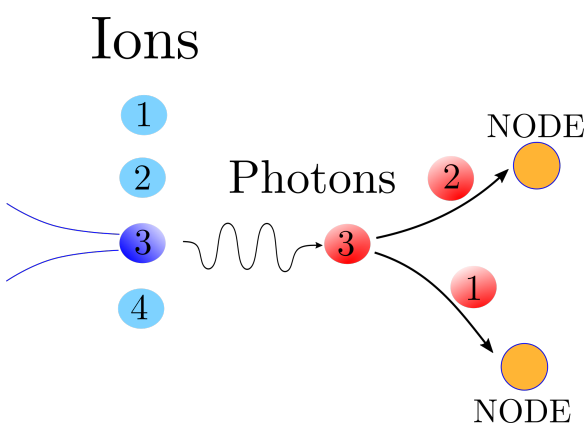
This thesis lies in the context of current efforts to enable the realization of quantum networks of light and matter. Currently there is an ongoing project to build a three node quantum network between two buildings on the Technik campus of the University of Innsbruck. The quantum nodes consist of ion traps: qubits are encoded in the electronic states of ions in a Paul trap, manipulation is done with laser pulses [13], and photons are collected with an optical cavity integrated into the ion-trap vacuum system. A 400 m

optical fiber serves as a quantum channel between the two buildings. This quantum network should have the ability to make entanglement between all three nodes simultaneously. Our approach is to develop the ability to connect multiple ions to multiple traveling direction-switchable photons, using a single-ion-focused *photon generation* beam.

Photons are generated via a cavity enhanced Raman process [14], for which a 393 nm laser is used. Before this master project, the 393 nm laser was shining on every ion in the trap. In this case, if an ion string were to be loaded, the light would couple to every ion and there would be no control over the single ion-photon pair. The same 393 nm laser will also be employed to perform ion-qubit manipulation by inducing an AC Stark shift on the qubit's ground state. A single-ion-focused laser allows the manipulation of individual ion-qubits performing thus single qubit operations as explained below.

This thesis presents the development of an optical system that focuses the 393 nm laser beam on a single ion, and has the ability to steer the beam on a timescale of a few microseconds, which is the typical time for photon generation operations and ion-qubit operations. The setup is per se not complex, but the design is critical. Ion separation is typically around 5 micrometers in our system, so the light should be focused down to  $1 - 2 \mu\text{m}$ , at the limits of the optical elements involved. The steering part is achieved with an acousto-optical deflector (AOD), which deflects the laser light on microsecond timescales proportionally to the applied input frequency allowing to control remotely the beam pointing of the system. The goal of this thesis is to perform the following experiments with the newly built setup:

## THESIS GOAL 1: CAVITY-PHOTON GENERATION FROM SELECTED IONS IN A STRING



As illustrated in the sketch on the left, the idea is to generate photons from individual ions in a string and send them to the different nodes of the network. The laser beam is focused on a single ion, a laser pulse triggers the generation of a photon, the beam is then steered and focused on another ion to repeat the process. The approach we use is an ion-cavity system: the laser pulse triggers a cavity enhanced Raman process [14] that on resonance causes the emission of a photon from one ion into the cavity. The photon subsequently exits from a preferred cavity mirror. In this thesis we set the goal of emitting photons from a particular ion without significantly exciting any other ion in the string. This is a key step towards producing and controlling multiple photon-ion pairs. Not shown here is the relationship between the emitting ion and the standing wave of the optical cavity vacuum-field, which must also be precisely controlled.

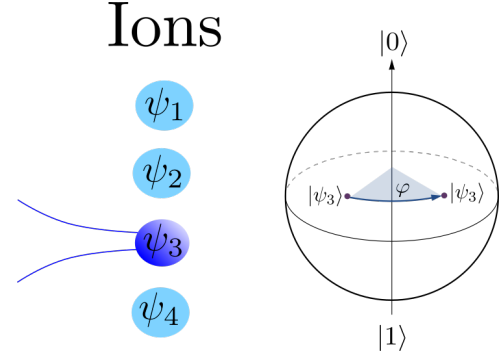
subsequently exits from a preferred cavity mirror. In this thesis we set the goal of emitting photons from a particular ion without significantly exciting any other ion in the string. This is a key step towards producing and controlling multiple photon-ion pairs. Not shown here is the relationship between the emitting ion and the standing wave of the optical cavity vacuum-field, which must also be precisely controlled.

## THESIS GOAL 2: SINGLE ION-QUBIT MANIPULATION

As illustrated in the sketch on the right, the same laser can perform quantum operations on the qubits encoded in the ions. Our goal is to manipulate the state of a single qubit without modifying the state of the others. Here the laser operates in a far-detuned regime, and induces an AC Stark shift on the  $|0\rangle = |S_{j=1/2}, m_j = -1/2\rangle$  state of the ion-qubit implementing a phase gate on a qubit encoded in this and another electronic state [15]. In order to measure the AC Stark shift we perform a Ramsey interferometry experiment [16], where a detuned Stark pulse is introduced between the two  $\pi/2$  pulses.

This pulse shifts the relative phase of the qubit and therefore the amount of Stark shift can be inferred from the final qubit state.

The rest of this thesis is presented in the following way: Chapter 2 is devoted to the theoretical background necessary to understand the rest of the work. Here, the foundations of quantum computing and networking are laid down, along with the basic concepts of ion trapping and Gaussian laser beams; Chapter 3 presents the existing experimental setup, i.e. the already built and working blocks of the experiment where the setup designed in this thesis has been added; Chapter 4 is the core of the thesis, here the final design made with the software Zemax and simulations of different aspects of the project are introduced and presented; Chapter 5 contains all the experimental results obtained. It is divided in two parts: first, the setup was built on an optical table, here we had the freedom to test different key properties of the performance of the system and decide whether or not it was satisfactory. After having the confidence that the system can work as desired, the setup was transferred and aligned on the main experiment where limited access did not allow for easy performance testing, except that which is possible with trapped ions. Here, we carried out two experiments that demonstrate the capability of the built system: to manipulate single qubits and to generate photons from single ions (the two main goals of the thesis). The description and discussion of these results are in the second part of Chapter 5. Lastly, in Chapter 6 a conclusion with a summary and a future outlook is given.





# Chapter 2

## Theoretical framework

Quantum computing is based on a general framework that does not depend on the particular physical quantum platform. In this chapter, important concepts such as qubits and quantum operations are described from a theoretical point of view, before showing how we can realize them with trapped ions. The same goes with quantum networking, the concept and the realization can be treated separately and they will be described in this chapter. Next, key properties of Gaussian beams are presented: the beam shapes emitted by our lasers. Acousto-optical interactions are then introduced and studied to give an idea of how AODs work and how they can be used to steer a laser beam. Lastly, a brief overview of two key experiments is given.

### 2.1 Quantum logic with trapped ions

#### 2.1.1 Quantum computer and quantum gates

The concepts of quantum computing are borrowed and extended from classical computation. In the classical case, information is mostly represented in terms of binary digits, the so called bit, essentially mapping information to a base-2 number. Information processing is done with gates acting on those numbers. The idea of a quantum computer is still to encode information in a binary form, but due to the nature of quantum mechanics, a quantum bit (in short qubit) gains new features that can be exploited to perform different kind of operations.

A qubit is a two-level system, which is described by the following wavefunction

$$|\psi\rangle = \alpha|0\rangle + \beta|1\rangle, \quad (2.1.1)$$

where  $|0\rangle, |1\rangle$  are two orthogonal states and  $\alpha, \beta$  are probability amplitudes, i.e. two complex numbers that satisfy the relationship  $|\alpha|^2 + |\beta|^2 = 1$ . The outcome of measuring a qubit in the logical basis (outcomes 0 or 1) will give the value 0 with a probability of  $|\alpha|^2$  and 1 with a probability of  $|\beta|^2$ .

Qubits also have a geometrical representation that can be useful. Equation (2.1.1) depends on 2 complex numbers, however since  $\psi$  is normalized, we can rewrite the expression as [15]

$$|\psi\rangle = e^{i\gamma} \left( \cos \frac{\theta}{2} |0\rangle + e^{i\varphi} \sin \frac{\theta}{2} |1\rangle \right). \quad (2.1.2)$$

The global phase factor  $e^{i\gamma}$  can be left out as it does not influence the measurement outcome, leaving only two real numbers:  $\theta$  and  $\varphi$ . A qubit can therefore be represented geometrically with normalized spherical coordinates. The so called Bloch sphere is depicted in Figure 2.1.1, every point on its surface represents a different state of the qubit. Qubit manipulation can be visualized as trajectories on the surface.

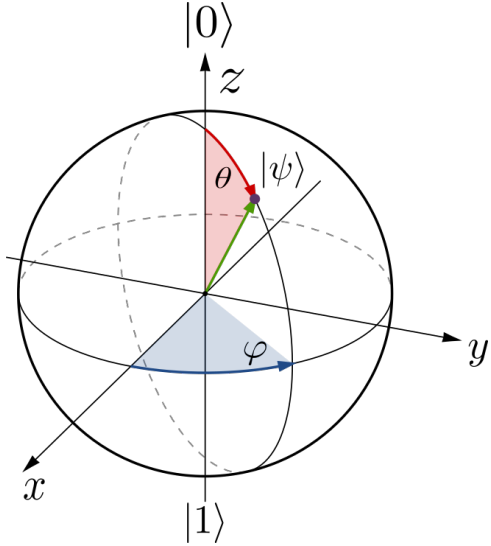


**Figure 2.1.1:** The Bloch sphere. The states  $|0\rangle$  and  $|1\rangle$  are at the poles of the sphere, every other point of the surface represents a superposition of these states. A single qubit quantum gate operations can be seen as trajectory on the surface mapping one state to another.

An alternative way of dealing with qubits is via vectors and matrices. We can assign to the states  $|0\rangle$  and  $|1\rangle$  the following:

$$|0\rangle = \begin{pmatrix} 1 \\ 0 \end{pmatrix} \quad |1\rangle = \begin{pmatrix} 0 \\ 1 \end{pmatrix} \implies |\psi\rangle = \begin{pmatrix} \alpha \\ \beta \end{pmatrix}. \quad (2.1.3)$$

In this representation, single qubit rotations are calculated using  $2 \times 2$  unitary matrices. These kind of operations are named *quantum gates* and they are the building blocks of quantum computing. Quantum algorithms can be written as a sequence of quantum gates. For a single qubit, any gate can be written as multiple combination of two operations, e.g. [17]

$$U_z(\Theta) = \begin{pmatrix} e^{-i\frac{\Theta}{2}} & 0 \\ 0 & e^{i\frac{\Theta}{2}} \end{pmatrix} \quad \text{and} \quad U_\varphi(\theta) = \begin{pmatrix} \cos \frac{\theta}{2} & -ie^{-i\varphi} \sin \frac{\theta}{2} \\ -ie^{i\varphi} \sin \frac{\theta}{2} & \cos \frac{\theta}{2} \end{pmatrix}. \quad (2.1.4)$$

These two matrices can be seen as two different rotations in the Bloch sphere,  $U_z$  is a rotation around the  $z$  axis by the angle  $\Theta$ , while  $U_\varphi$  is a rotation around an axis located in the  $x$ - $y$  plane. Important examples of single qubit gates are the Hadamard gate  $H$ , which creates a superposition of one qubit starting from the state  $|0\rangle$ , or  $|1\rangle$ , and the phase shift gate  $R_\phi$  that shifts the phase [15]:

$$H = \frac{1}{\sqrt{2}} \begin{pmatrix} 1 & 1 \\ 1 & -1 \end{pmatrix} \equiv U_{\varphi=\pi} \left( \frac{\pi}{2} \right) U_z(\pi) \quad R_\phi = \begin{pmatrix} 1 & 0 \\ 0 & e^{i\phi} \end{pmatrix} \equiv e^{i\varphi/2} U_z(\varphi). \quad (2.1.5)$$

Gates that involve  $N$  qubits are written as  $2^N \times 2^N$  unitary matrices, a famous example is the controlled not (CNOT) gate

$$\text{CNOT} = \begin{pmatrix} 1 & 0 & 0 & 0 \\ 0 & 1 & 0 & 0 \\ 0 & 0 & 0 & 1 \\ 0 & 0 & 1 & 0 \end{pmatrix}. \quad (2.1.6)$$

Which can be used to generate entanglement between two qubits. It can be shown [15] that the examples of this section:  $H$  gate, phase gate, and CNOT gate form a universal set of quantum gates, i.e. a sequence of these gates realizes (in some cases approximates) every other possible unitary quantum operation.

## 2.1.2 Ion qubits and laser-ion interactions

Qubits can be encoded in any pair of orthogonal quantum states of a physical system. In Figure 2.1.2 the level scheme of  $^{40}\text{Ca}^+$  is presented. The states  $|\text{S}_{1/2}\rangle$  and  $|\text{D}_{5/2}\rangle$  are a common choice to encode a qubit [18]. The ground state  $|\text{S}_{1/2}\rangle$  represents the state  $|0\rangle$  and the long lived ( $\sim 1$  s) excited state  $|\text{D}_{5/2}\rangle$  can be  $|1\rangle$ . As these levels are directly connected by an electric-quadrupole transition at an optical wavelength (729 nm), this kind of qubit is often referred to as an optical qubit. Lasers provide a way to directly manipulate the population of these two levels and therefore to manipulate the state of the qubit.

The laser set up in this thesis is the one at 393 nm, which interacts via a dipole transition (different from the 729 nm transition) with the atomic ion. We model therefore the atom-light interactions as dipole interaction. In the case of a quadrupole interaction, the equations below still hold with the exception of the atom-light coupling strength (defined below), which will no longer depend linearly with the electric field. For a proper treatment of the quadrupole interaction see [19].

Consider the simple two-level system in Figure 2.1.3, where the states  $|0\rangle$  and  $|1\rangle$  are separated by a frequency  $\omega_0$ , while the laser is assumed to be monochromatic with frequency  $\omega_l$ . The difference  $\Delta = \omega_l - \omega_0$  is called detuning and we assume to be in the near-resonant regime  $\Delta \ll \omega_0$ . The Hamiltonian of the atomic part can be written as:

$$H_a = \hbar\omega_0 |1\rangle\langle 1|, \quad (2.1.7)$$

where  $\omega_0$  is the frequency difference between the ground and excited state, the energy of the ground state has also been set to 0. The Hamiltonian of the interaction between the dipole atomic moment  $\mathbf{d}$  and the electric field of the laser can be written [20]

$$H_{int} = -\mathbf{d} \cdot \mathbf{E} \quad (2.1.8)$$

where the electric field of the laser will be treated classically and the dipole approximation is assumed. This means

$$\mathbf{E}(t) = \hat{\varepsilon} E_0 \cos(\omega_l t + \varphi) = \hat{\varepsilon} \frac{E_0}{2} (e^{-i(\omega_l t + \varphi)} + e^{i(\omega_l t + \varphi)}), \quad (2.1.9)$$

where  $\hat{\varepsilon}$  is the unit polarization vector, and  $\varphi$  is the laser phase at the point of the ion at time 0. The next step is to work out the dipole operator, this can be done by applying

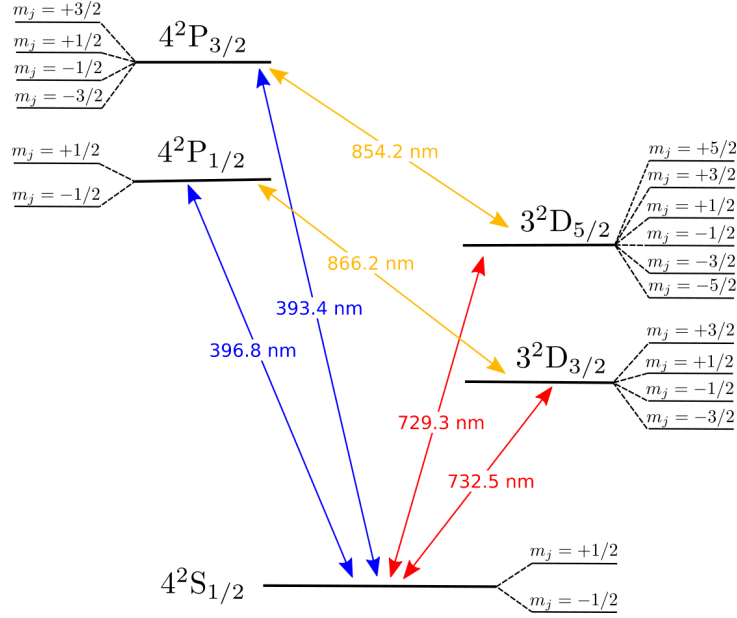


**Figure 2.1.2:** Level scheme of  $^{40}\text{Ca}^+$ , notation is  $n^{2s+1}l_{j,m_j}$ , where  $n$  is the principal quantum number,  $s$  the electron spin,  $l$  the orbital angular moment,  $j = |l \pm s|$  the total angular moment, and  $m_j$  the magnetic quantum number. For a detailed description see Section 3.1.1. For quantum computing purposes, the chosen qubit transition is the long lived quadropole transition  $|\text{S}_{1/2}\rangle \rightarrow |\text{D}_{5/2}\rangle$  at 729 nm between a single pair of Zeeman states ( $m_j$ ). Blue and orange transitions are dipole transitions suitable for cooling, and imaging. Red transitions are dipole forbidden, but accessible via an electric quadrupole transition, they are used to encode qubits. In addition, the 854 nm transition is tuned in resonance with the cavity for photon generation purposes.

the identity  $|0\rangle\langle 0| + |1\rangle\langle 1|$  on both sides of  $\mathbf{d}$ . Due to parity arguments [20], only the non diagonal terms are non-vanishing, giving

$$\mathbf{d} = \langle 0|\mathbf{d}|1\rangle (|0\rangle\langle 1| + |1\rangle\langle 0|) \equiv \langle 0|\mathbf{d}|1\rangle (\sigma + \sigma^\dagger). \quad (2.1.10)$$

Combining the last three equations yields

$$H_{int} = -\langle 0|\hat{\varepsilon}\mathbf{d}|1\rangle \frac{E_0}{2}(\sigma e^{i(\omega_l t + \varphi)} + \sigma^\dagger e^{-i(\omega_l t + \varphi)} + \sigma e^{-i(\omega_l t + \varphi)} + \sigma^\dagger e^{i(\omega_l t + \varphi)}) \quad (2.1.11)$$

A rotating wave approximation is used now: in the interaction picture, the operator  $\sigma$  ( $\sigma^\dagger$ ) evolves under the Hamiltonian  $H_a$  in time as  $\tilde{\sigma} = e^{iH_a t/\hbar} \sigma e^{-iH_a t/\hbar} = \sigma e^{-i\omega_0 t}$  ( $\tilde{\sigma}^\dagger = \sigma^\dagger e^{i\omega_0 t}$ ). Therefore, Equation 2.1.11 in the interaction picture contains terms that oscillate as  $\propto e^{\pm i(\omega_l - \omega_0)t}$ , and  $\propto e^{\pm i(\omega_l + \omega_0)t}$ . We can drop the fast oscillating terms and keeping only those that depend on time as  $\propto e^{\pm i(\omega_l - \omega_0)t}$ . The validity of this approximation is given by the fact that  $\omega$  and  $\omega_0$  are in the optical regime, thus they oscillate extremely fast compared to  $\Delta$  and average to zero, the interesting slow dynamic is given only by their difference: the detuning. Going back in the Schrödinger picture yields the final form of the interaction Hamiltonian

$$H_{int} = \frac{\hbar\Omega}{2}(\sigma e^{i(\omega_l t + \varphi)} + \sigma^\dagger e^{-i(\omega_l t + \varphi)}), \quad (2.1.12)$$

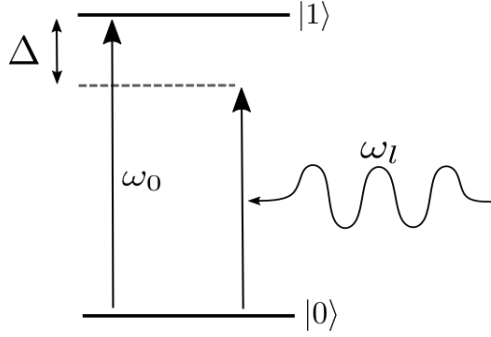


**Figure 2.1.3:** 2-level atom scheme, the ground and excited states are denoted as  $|0\rangle$ , and  $|1\rangle$ .  $\omega_l$  is the laser frequency, which is detuned by  $\Delta \equiv \omega_l - \omega_0$  from the transition frequency  $\omega_0$ .

where we defined the Rabi frequency  $\Omega \equiv -\langle 0|\hat{\mathbf{d}}|1\rangle E_0/\hbar$ . The Rabi frequency depends linearly on the applied electrical field strength and hence its square is proportional to the intensity of the laser  $\Omega^2 \propto I$ . To summarize, the total system Hamiltonian is

$$H = H_a + H_{int} = \hbar\omega_0 |1\rangle\langle 1| + \frac{\hbar\Omega}{2}(\sigma e^{i(\omega_l t + \varphi)} + \sigma^\dagger e^{-i(\omega_l t + \varphi)}). \quad (2.1.13)$$

To eliminate the time dependence, we can go in the rotating frame with the unitary transformation  $U = e^{i\omega_l t |1\rangle\langle 1|}$ , the Hamiltonian in this frame is

$$\tilde{H} = -\hbar\Delta |1\rangle\langle 1| + \frac{\hbar\Omega}{2}(e^{i\varphi}\sigma + e^{-i\varphi}\sigma^\dagger) \quad (2.1.14)$$

The time dependence is now gone, and the unitary evolution matrix can be calculated as

$$U(t) = \exp\left\{-\frac{i}{\hbar}\tilde{H}t\right\} = \begin{pmatrix} \cos\left(\frac{\tilde{\Omega}t}{2}\right) + i\frac{\Delta}{\tilde{\Omega}}\sin\left(\frac{\tilde{\Omega}t}{2}\right) & -ie^{i\varphi}\frac{\Delta}{\tilde{\Omega}}\sin\left(\frac{\tilde{\Omega}t}{2}\right) \\ -ie^{-i\varphi}\frac{\Delta}{\tilde{\Omega}}\sin\left(\frac{\tilde{\Omega}t}{2}\right) & \cos\left(\frac{\tilde{\Omega}t}{2}\right) - i\frac{\Delta}{\tilde{\Omega}}\sin\left(\frac{\tilde{\Omega}t}{2}\right) \end{pmatrix}. \quad (2.1.15)$$

Where  $\tilde{\Omega} = \sqrt{\Delta^2 + \Omega^2}$  is the generalized Rabi frequency. In the case of zero detuning ( $\Delta = 0$ ) the matrix is the same as Equation (2.1.4), thus a resonant laser pulse implements the qubit rotation  $U_\varphi(\theta)$ .

As an example, let us take the atom in the ground state  $|\psi\rangle = |0\rangle$  and apply the unitary evolution (2.1.15). The probability to be in the excited state becomes

$$\mathbb{P}\{|1\rangle\}(t) = |\langle 1|U(t)|0\rangle|^2 = \frac{\Omega^2}{\Omega^2 + \Delta^2} \sin^2\left(\frac{\tilde{\Omega}t}{2}\right) \quad (2.1.16)$$

This equation is plotted in Figure 2.1.4. For  $\Delta = 0$ , we get a cosine behaviour, the so called Rabi oscillations. The probability amplitude for the electron, under continuous drive by a laser, will oscillate between the ground and excited state at a frequency  $\Omega/2$ . Detuning reduces the amplitude of such oscillations and increases the oscillation frequency. Rabi oscillations are an important tool in quantum information, laser pulses can prepare the state of the qubit in any superposition, e.g. starting in the  $|0\rangle$  state, a  $\pi/2$  pulse ( $\Omega t = \pi/2$  and phase  $\varphi = 0$ ) will result in the state  $(|0\rangle - i|1\rangle)/\sqrt{2}$ , with a  $\pi$  pulse ( $\Omega t = \pi$ ,  $\varphi = \pi$ ) the population is completely transferred to another level  $|0\rangle \rightarrow |1\rangle$ . These

pulses can be used to implement e.g. the Hadamard gate of Equation (2.1.5).

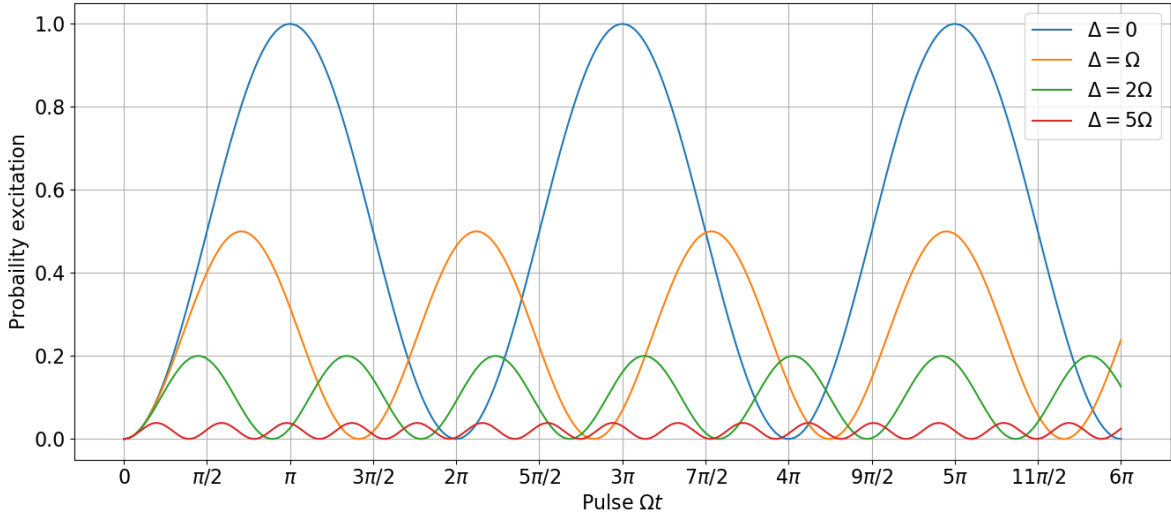


**Figure 2.1.4:** Rabi flops for different detunings  $\Delta$ , starting from the  $|0\rangle$  state. Equation (2.1.16).

As the light is detuned from the transition, Rabi oscillations are suppressed: the amplitude is reduced by a factor of 0.5 already with  $\Delta = \Omega$ , while a factor of 10 in reduction is achieved with a detuning of  $\Delta = 5\Omega$ . However, another effect occurs in the off-resonant regime, the energy levels are shifted [20]. The shift  $\delta$  can be calculated by finding the eigenvalues of the Hamiltonian (2.1.14), which can be written in matrix form and diagonalized. We find that there are two eigenstates  $|+\rangle$  and  $|-\rangle$  called dressed states with eigenvalues

$$E_{\pm} = -\frac{\hbar\Delta}{2} \pm \frac{\hbar}{2}\sqrt{\Delta^2 + \Omega^2}. \quad (2.1.17)$$

In the limit  $\Delta \gg \Omega$ , dressed states tend to the bare states  $|+\rangle \rightarrow |1\rangle$ ,  $|-\rangle \rightarrow |0\rangle$ , and the energies become

$$E_{\pm} \rightarrow -\frac{\hbar\Omega}{2} \pm \frac{\hbar\Omega}{2} \pm \frac{\hbar\Omega^2}{4\Delta} \implies \delta = \pm \frac{\Omega^2}{4\Delta}. \quad (2.1.18)$$

The effective Hamiltonian for the off-resonant regime can be derived following a Markovian approximation [21]

$$H_{AC} = \frac{1}{\hbar\Delta} [\sigma, \sigma^\dagger] = \frac{\hbar\delta}{2} \sigma_z \quad (2.1.19)$$

The corresponding evolution is

$$U(t) = \exp \left\{ -\frac{i}{\hbar} H_{AC} t \right\} = \begin{pmatrix} \exp \left\{ i \frac{\delta}{2} t \right\} & 0 \\ 0 & \exp \left\{ i \frac{\delta}{2} t \right\} \end{pmatrix}. \quad (2.1.20)$$

This matrix implements the quantum gate  $U_z(\Theta)$  from Equation (2.1.4).

### 2.1.2.1 Three-level model

We extend our model to a 3 level  $\Lambda$ -type atom driven by two lasers, which more closely resembles the real experimental situation (393 nm, 729 nm lasers and  $|S_{1/2}\rangle$ ,  $|P_{3/2}\rangle$ ,  $|S_{5/2}\rangle$ )

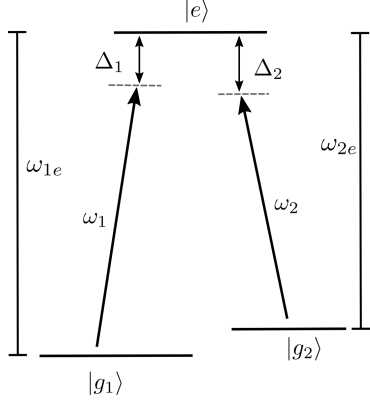


**Figure 2.1.5:** 3-level  $\Lambda$ -type atom model. Two long lived ground states  $|g_1\rangle$ ,  $|g_2\rangle$  couple to an excited level  $|e\rangle$  (atomic frequencies  $\omega_{1e}$ , and  $\omega_{2e}$  respectively) through two lasers of frequencies  $\omega_1$ ,  $\omega_2$  detuned respectively  $\Delta_1$ ,  $\Delta_2$  from the transitions.

states, see Figure 2.1.2) in the experiments in this thesis. The model contains new effects that describe photon generation and qubit gates. In particular, stimulated Raman transitions will be discussed, and we will show how, under certain conditions, the system can be approximated as an effective 2-level atom. The system is depicted in Figure 2.1.5, two ground states  $|g_1\rangle$  and  $|g_2\rangle$  are present together with a common excited state  $|e\rangle$ . Two different lasers  $\omega_1$ ,  $\omega_2$  drive the transition  $|g_1\rangle \rightarrow |e\rangle$  and  $|g_2\rangle \rightarrow |e\rangle$ , where the atomic frequencies are  $\omega_{1e}$ , and  $\omega_{2e}$  respectively. Detunings are defined as  $\Delta_1 = \omega_1 - \omega_{1e}$  and  $\Delta_2 = \omega_2 - \omega_{2e}$ . In the case of calcium, the ground states are  $|\text{S}_{1/2}\rangle$ , and  $|\text{D}_{5/2}\rangle$ . This is the qubit transition, and it is long lived ( $\sim 1$  s), such that any spontaneous emission from D to S can be neglected. The excited level is  $|\text{P}_{3/2}\rangle$  which can decay into both ground states with branching ratio of 94% from P $\rightarrow$ S ( $\sim 7.4$  ns) and 5.3% from P $\rightarrow$ D ( $\sim 101$  ns), we neglect decay to the  $|\text{D}_{3/2}\rangle$  state.

Following the approach of [20], the bare atom Hamiltonian is

$$H_a = -\hbar\omega_{1e} |g_1\rangle \langle g_1| - \hbar\omega_{2e} |g_2\rangle \langle g_2|, \quad (2.1.21)$$

with the convention of setting the excited level energy to 0. The electric field is now the sum of the two laser fields

$$\mathbf{E}(t) = \hat{\varepsilon}_{01} E_{01} \cos(\omega_1 t \varphi_1) + \hat{\varepsilon}_{02} E_{02} \cos(\omega_2 t + \varphi_2). \quad (2.1.22)$$

As in Section 2.1.2, we then consider a dipole interaction, make the dipole approximation and a rotating wave approximation. Finally, the full final Hamiltonian in the rotating frame is

$$H = \hbar\Delta_1 |g_1\rangle \langle g_1| + \hbar\Delta_2 |g_2\rangle \langle g_2| + \frac{\hbar\Omega_1}{2} \left( \sigma_1 e^{i\varphi_1} + \sigma_1^\dagger e^{i\varphi_1} \right) + \frac{\hbar\Omega_2}{2} \left( \sigma_2 e^{i\varphi_2} + \sigma_2^\dagger e^{i\varphi_2} \right), \quad (2.1.23)$$

where  $\Omega_i = -\frac{\langle g_i | \varepsilon_i \cdot \mathbf{d} | e \rangle E_i}{\hbar}$ , and  $\sigma_i = |g_i\rangle \langle e|$ . Under the conditions: equal detunings  $\Delta_1 = \Delta_2 \equiv \Delta$  (Raman resonance), and  $\Delta \gg \Omega_1, \Omega_2$ , the Hamiltonian (2.1.23) describes a Raman process, where state population is transferred coherently between  $|g_1\rangle$  and  $|g_2\rangle$ . Intuitively, this corresponds to the situation where the difference of the two driving frequencies ( $\omega_1 - \omega_2$ ) is equal to the frequency splitting between  $|g_1\rangle$ , and  $|g_2\rangle$ .

Following [22] it can be shown that, under the previous conditions, the Raman process

leads to an effective coupling directly between the two ground states. The effective Rabi frequency of the coherent population transfer  $|g_1\rangle \rightarrow |g_2\rangle$  is [20]

$$\Omega_{eff} = \frac{\Omega_1\Omega_2}{2\Delta}. \quad (2.1.24)$$

### 2.1.2.2 Dissipative processes

In our experiments spontaneous emission can play a role as the condition  $\Delta \gg \Omega_1, \Omega_2$  is only partially fulfilled. In this section therefore, we present a quantitative overview of spontaneous scattering as a function of detuning and Rabi frequency of each laser. Dissipative processes do not follow a Hermitian evolution, hence their mathematical description is done heuristically by adding terms in the Heisenberg equation

$$\frac{d\rho}{dt} = \frac{1}{i\hbar}[H, \rho] + \mathcal{L}(\rho). \quad (2.1.25)$$

This equation is usually referred to as master equation in Lindblad form, where  $\rho$  is the density matrix of the system. The superoperator  $\mathcal{L}(\rho)$  contains phenomena not included in the Hamiltonian. For spontaneous emission, the form of  $\mathcal{L}(\rho)$  is [23]

$$\mathcal{L}(\rho) = \frac{\Gamma}{2}(2\sigma\rho\sigma^\dagger - \sigma^\dagger\sigma\rho - \rho\sigma^\dagger\sigma), \quad (2.1.26)$$

where  $\Gamma$  is the spontaneous emission rate. For the three level atom, in the effective 2 level system picture, the spontaneous emission is modified as [22]

$$\Gamma_{eff} = \left( \frac{\Omega_1}{2\Delta_1} \right)^2 \cdot \Gamma. \quad (2.1.27)$$

The ratio between  $\Gamma_{eff}$  and the AC Stark shift (2.1.18)  $\delta/\Gamma_{eff} \propto \Delta$  dictates which effect is dominant, i.e. by increasing the detuning, the effective rate of spontaneous scattering can be reduced in favor of the AC Stark shift. This regime can be used to implement a phase gate where the qubit is encoded in the  $|g_1\rangle \rightarrow |g_2\rangle$  transition and the phase of  $|g_1\rangle$  is manipulated by Stark shifting the transition  $|g_1\rangle \rightarrow |e\rangle$ . In the experiment of Section 5.3.1, we implement this gate on a single ion in a string.

## 2.2 Quantum networking with trapped ions

### 2.2.1 General introduction

A quantum network is a collection of quantum processors, referred to as nodes, interconnected with quantum channels, referred to as links. Nodes are used for processing and storing quantum information, while links for quantum information distribution [4]. Links are typically realized with traveling photons (flying qubits [24]), either in free-space [25] or in optical fibers. Nodes can be realized using different physical systems: trapped ions [26], neutral atoms [27], atomic ensembles [4]. Nodes and links are connected through an interface that converts a stationary qubit in a node to a flying qubit over the network. In the next section we will explore how such an interface can be realized by placing an

ion-qubit in an optical cavity.

Faithful transmission of quantum states over long distances can be a daunting problem as quantum information cannot be cloned [28] and noisy channels can destroy the delicate nature of qubits. Quantum repeaters have been designed [29] to circumvent these problems through a series of protocols which include entanglement purification: a form of error correction [30]. Once entanglement has been established between nodes, other network functionalities become available, like for instance teleportation [31]. Entanglement generation, and quantum repeaters are just some examples of the fundamental steps necessary for building a quantum network, for a more in depth review look at [5].

## 2.2.2 Cavity QED

A single trapped ion is a single photon source and those photons can be collected either with a lens [26], with mirrors [32] or with optical cavities [33]. Photon collection from ions using an optical cavity is a powerful approach, that will now be introduced in detail. A cavity placed around ions can improve the efficiency of photon collection as the probability of a photon to be emitted in the cavity mode is enhanced with respect to emitting in free space [34].

In this Section a simple model of a two-level system in a cavity is described following the approach of [20]. We describe the cavity electric field as quantized, with  $a, a^\dagger$  the creation and annihilation operators of a single photon in the cavity mode, respectively. The quantized electric field assumes the form of

$$\mathbf{E} = A(\mathbf{f}(\mathbf{r})a + \mathbf{f}^*(\mathbf{r})a^\dagger) \quad (2.2.1)$$

where  $A$  is an amplitude, and  $\mathbf{f}(\mathbf{r})$  is the spatial mode profile. The interaction between the dipole moment of a two-level atom and the cavity field is in the dipole form

$$H_{int} = -\mathbf{d} \cdot \mathbf{E} = \hbar g(\sigma a^\dagger + \sigma^\dagger a), \quad (2.2.2)$$

where  $g = A \langle 0 | \mathbf{d} | 1 \rangle \cdot \mathbf{f}(\mathbf{r})$  is called the cavity coupling constant; it is analogous to the Rabi frequency. An important dependence of  $g$  can be found by considering that  $f(r)$  is inversely proportional to the volume of the cavity  $V$ , i.e.

$$g \propto \langle 0 | d | 1 \rangle \sqrt{\frac{\omega}{2\epsilon_0 \hbar V}}. \quad (2.2.3)$$

The coupling therefore increases with decreasing cavity volume.

The total system Hamiltonian includes also the atomic part and the free evolution of the cavity single mode field, it is written as [35]

$$H = \hbar\omega_0 |1\rangle\langle 1| + \hbar\omega a^\dagger a + \hbar g(\sigma a^\dagger + \sigma^\dagger a). \quad (2.2.4)$$

$H$  takes the name of Jaynes-Cummings Hamiltonian. We are interested in comparing the coherent process in (2.2.4) with spontaneous emission in a free-space field mode and decay in one cavity mode out of the cavity. The first is quantified with the atomic decay rate  $\Gamma = 2\gamma$ , while the latter is characterized by the cavity decay rate  $\kappa$  (half width half

maximum). The decay rate  $\kappa$  depends exclusively on the cavity parameters as [36]

$$\kappa = \frac{c\pi}{FL}, \quad (2.2.5)$$

where  $F$  is the cavity finesse, and  $L$  the length.

### 2.2.3 Photon generation

In our experiments, photons are generated from an ion-cavity system. Photon generation involves three levels and occurs via the Raman process described in Section 2.1.2.1. However, here the second laser is replaced by the vacuum electric field of the cavity in a process known as cavity-mediated Raman Process (CMRP) [14]. In Figure 2.2.1 the relevant calcium levels for the CMRP are displayed. Our choice for the three levels is

$$|S_{1/2}, -1/2\rangle \rightarrow |P_{3/2}, -3/2\rangle \rightarrow |D_{5/2}, -5/2\rangle. \quad (2.2.6)$$

In this case, the transition strengths, i.e. the projection of the laser polarization onto the dipole moment, and the same projection onto the cavity axis, are maximized over all other choices of transitions for the CMRP [14]. A single 393 nm laser pulse with Rabi frequency  $\Omega$  couples the  $S_{1/2}$  level to the  $P_{3/2}$  level, which is coupled to  $D_{5/2}$  via the vacuum mode of the cavity. Therefore, the electron state is transferred from the state  $|S_{1/2}\rangle \rightarrow |D_{5/2}\rangle$  by absorbing a laser photon and emitting a photon into the cavity. The final state is therefore  $|D_{5/2}\rangle |1\rangle$ , where  $|1\rangle$  indicates one photon in the cavity. Afterwards, the photon leaves the cavity leaving the system in the  $|D_{5/2}\rangle |0\rangle$  state. The effective Rabi frequency (2.1.24) of the population transfer is modified as [37]

$$\Omega_{eff} = \frac{\Omega g}{\Delta}, \quad (2.2.7)$$

where the Rabi frequency of the second laser is now replaced by the atom cavity coupling  $g$  in analogy to the 3-level Raman process of Equation (2.1.24). The Raman resonance appears when the detuning  $\Delta$  of the laser and the cavity are the same. The effective spontaneous decay rate from the  $P_{3/2}$  level is from Equation (2.1.27)

$$\Gamma_{eff} = \left( \frac{\Omega}{2\Delta} \right)^2 \Gamma. \quad (2.2.8)$$

Rabi oscillations (quantified by  $\Omega_{eff}$ ) and spontaneous emission (quantified by  $\Gamma_{eff}$ ) are two competitive effects, the dominant one depends on the ratio of the detuning and the laser Rabi frequency  $\Omega_{eff}/\Gamma_{eff} \propto \Delta/\Omega$ . It is therefore possible to reduce spontaneous emission effects if the detuning is large enough.

In our experiment, the cavity is near concentric with a length of  $L = 19.90$  mm, radius of curvature of 9.98 mm, and waist of 12.3  $\mu$ m. The maximum  $g$  achievable with this geometry is  $g_{max} = 2\pi \times 1.53$  MHz, while the decay rate is  $\kappa = 2\pi \times 70$  kHz. More information on our cavity can be found in [38] and in the upcoming thesis of J. Schupp. Typical numbers in our experiment for the CMRP are  $\Omega = 2\pi \times 40$  MHz, detuning  $\Delta = 2\pi \times 400$  MHz,  $g = 2\pi \times 1$  MHz, and from table 3.1.1,  $\Gamma = 2\pi \times 21.4$  MHz. With

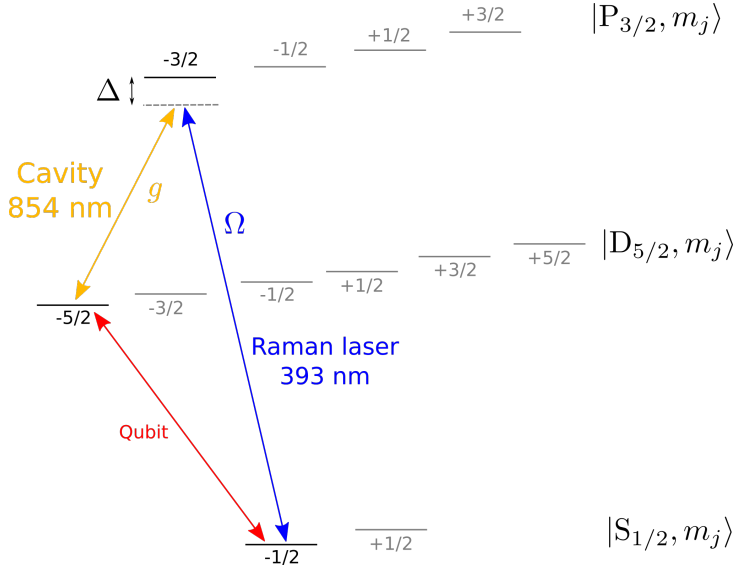


**Figure 2.2.1:** Zeeman structure of the relevant manifolds of calcium for the photon generation process. Here only one choice for the Zeeman levels is depicted, but others are also possible. If the cavity and the Raman laser have the same detuning  $\Delta$ , an electron in the ground state  $|S_{1/2}\rangle$  absorbs a 393 nm photon and ends in the  $|D_{5/2}\rangle$  state after emitting an 854 nm photon in the cavity.

these conditions we have

$$\Omega_{eff} \sim 2\pi \times 100 \text{ kHz} > \Gamma_{eff} \sim 2\pi \times 53 \text{ kHz}.$$

The regime we work in is thus  $2\kappa > \Omega_{eff} > \Gamma_{eff}$ . In Section 5.3.2, we use the laser focused on a single ion, developed in this thesis, to implement the CMRP on a single ion in a string.

## 2.3 Basics of ion trapping

### 2.3.1 Linear Paul trap

Ions are charged, therefore electric fields can be used to control and trap them. In order to achieve confinement in 3 dimensions, a potential  $\phi(x, y, z)$  with minima in all directions is needed. However, it follows directly from Laplace equation  $\nabla^2\phi = 0$  that the potential must be antitrapping at least in one direction. There are two workarounds for this problem: the first one introduces magnetic fields to trap particles in some directions, this takes the name of Penning trap [39]. The second solution is the so called Paul trap [40], and it is what we are going to describe in this section. The idea is to introduce a time varying potential, such that the antitrapping direction is constantly switching between two different dimensions. The particles will therefore experience an effective confinement in all directions if the switching is fast compared to the time it takes the particle to respond.

The shape of the trap can be adapted to load more ions in different geometries. In our work we utilize a linear Paul trap, which is elongated in one direction. The confinement in this direction is weaker and thus loaded ions will align in a single long string. This kind of trap is depicted in Figure 2.3.1. The confinement in the  $x - y$  plane is provided by 4

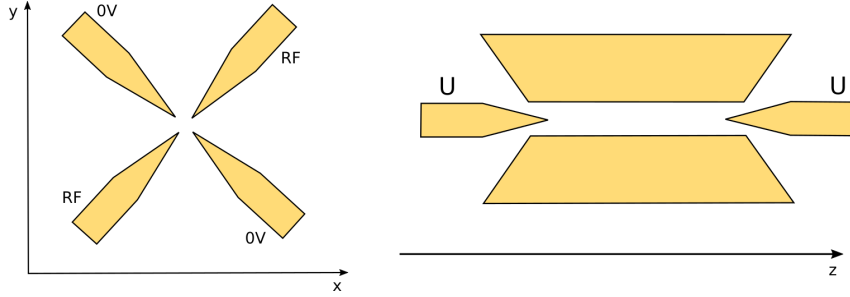


**Figure 2.3.1:** A linear paul trap. U is the voltage applied to the electrodes trapping in the  $z$  direction, while in the  $x - y$  plane trapping is achieved with a radio frequency signal.

electrodes, two of which are grounded and the other two are connected to a radio frequency source. This design is similar to a mass filter, with the difference of additional endcap electrodes in the  $z$  direction that plug the trap and confine also in the axial direction.

The potential inside the trap can be described for the  $x - y$  plane independently from the  $z$  direction. In the case of a linear Paul trap the radial potential is [41]:

$$\phi = \frac{\Phi_0}{2r_0^2} (x^2 - y^2), \quad (2.3.1)$$

where  $r_0$  is the distance from the center of the trap to the electrodes. The amplitude consists of a static part  $U_0$  and a dynamical one  $\Phi_0 = U_0 + V \cos(\Omega_{RF}t)$ . The study of the particle's motion with mass  $m$  and charge  $e$  inside the trap can be done with classical physics, Newton's second law in this case is

$$m\ddot{x} = -q \frac{\partial \phi}{\partial x} = -\frac{ex}{r_0^2} (U_0 + V \cos(\Omega_{RF}t)), \quad (2.3.2)$$

and similarly for  $\ddot{y}$ . This equation can be written in the form of a Mathieu equation [42] by defining two parameters:

$$a_x = \frac{4eU_0}{\Omega_{RF}^2 r_0^2 m}, \quad q_x = \frac{2eV}{\Omega_{RF}^2 r_0^2 m} \implies \ddot{x} + \frac{\Omega_{RF}}{4} (a_x + 2q_x \cos(\Omega_{RF}t)) x = 0 \quad (2.3.3)$$

and with a change of variable  $\tau = \frac{\Omega_{RF}t}{2}$  we end up with

$$\frac{\partial^2 x}{\partial \tau^2} + (a_x + 2q_x \cos(2\tau)) x = 0 \quad (2.3.4)$$

This kind of equation has stable solutions that can be found in a recursive way with Floquet's theorem [43]. In the limit  $a_x \ll q_x \ll 1$ , solutions to (2.3.4) are found to be

$$x(t) = x_0 \cos(\omega_x t + \phi_x) \left[ 1 + \frac{q_x}{2} \cos(\Omega_{RF}t) \right]. \quad (2.3.5)$$

Here, we recognize a oscillation  $\omega_x$ , referred to as *secular motion*, with amplitude modulated by a oscillation  $\Omega_{RF}$ , called *micromotion*. The approximation, named secular, is valid only in the case  $\omega_x \ll \Omega_{RF}$ . The frequency  $\omega_x$  is given in the solution as

$$\omega_x = \frac{\Omega_{RF}}{2} \sqrt{a_x + \frac{q_x^2}{2}}. \quad (2.3.6)$$

By imposing real solutions to (2.3.6), the stability diagram of the trap can be found in terms of  $a_x$  and  $q_x$  [41]. The other spatial dimension can be treated in the same way and the results are the same.

Confinement in the axial direction  $z$  is purposely weaker, and ions will align in this direction. Two electrodes with constant potential  $U$  are present, they create a harmonic potential

$$V = \frac{1}{2}m\omega_z^2 z^2, \quad (2.3.7)$$

where  $\omega_z$  is the axial trap frequency. In the case of a string of ions, mutual repulsions must also be included, in the next section we will consider this case.

### 2.3.2 Ion strings

For the goals of this thesis, we are interested in the separation between  $N$  ions loaded in the trap. This will give us an idea of how narrowly the beam should be focused and will set an appropriate problem spatial scale.

Following the approach of [44], let us consider the  $z$  direction where the ions are more weakly confined such that they form a string. The potential can be approximated as harmonic and hence given by

$$V = \sum_{i=0}^N \frac{1}{2}m\omega_z^2 z_i^2 + \sum_{i \neq j}^N \frac{Z^2 e^2}{8\pi\epsilon_0} \frac{1}{|z_i - z_j|}, \quad (2.3.8)$$

where  $z_i$  is the position of the  $i$ -th ion, and  $Z$  the degree of ionization of the ions. The equilibrium positions can be found at the minima of the potential, i.e. where the first derivative is zero

$$\frac{\partial V}{\partial z_i} = 0 \implies u_i - \sum_{j=1}^{i-1} \frac{1}{(u_i - u_j)^2} + \sum_{j=i+1}^N \frac{1}{(u_i - u_j)^2} = 0, \quad (2.3.9)$$

and where we defined the dimensionless quantity  $u_i = z_i/l$  and  $l^3 = \frac{Z^2 e^2}{4\pi\epsilon_0 m \omega^2}$ . The last equation can be solved analytically for 2 or 3 ions. For the case  $N = 2$  we get the system

$$\begin{cases} u_1 + \frac{1}{(u_1 - u_2)^2} = 0 \\ u_2 - \frac{1}{(u_1 - u_2)^2} = 0 \end{cases} \implies u_1 = -u_2, \quad u_1 = \left(\frac{1}{2}\right)^{2/3} \simeq 0.629 \quad (2.3.10)$$

For  ${}^{40}\text{Ca}^+$  ions (atomic mass  $\simeq 40$  u [45]) in a Paul trap with axial confinement of  $\omega_z = 2\pi \times 1$  MHz, we have  $l \simeq 4.4 \times 10^{-6}$  m, which means that 2 ions are separated by  $\simeq 5.6 \mu\text{m}$ . This size is accessible since it is above the diffraction limit (ref. Section 2.4.1) for optical atomic transitions. In Figure 2.3.2, ions positions are presented for different number of ions  $N$  trapped with an axial confinement of  $\omega_z = 2\pi \times 1$  MHz.

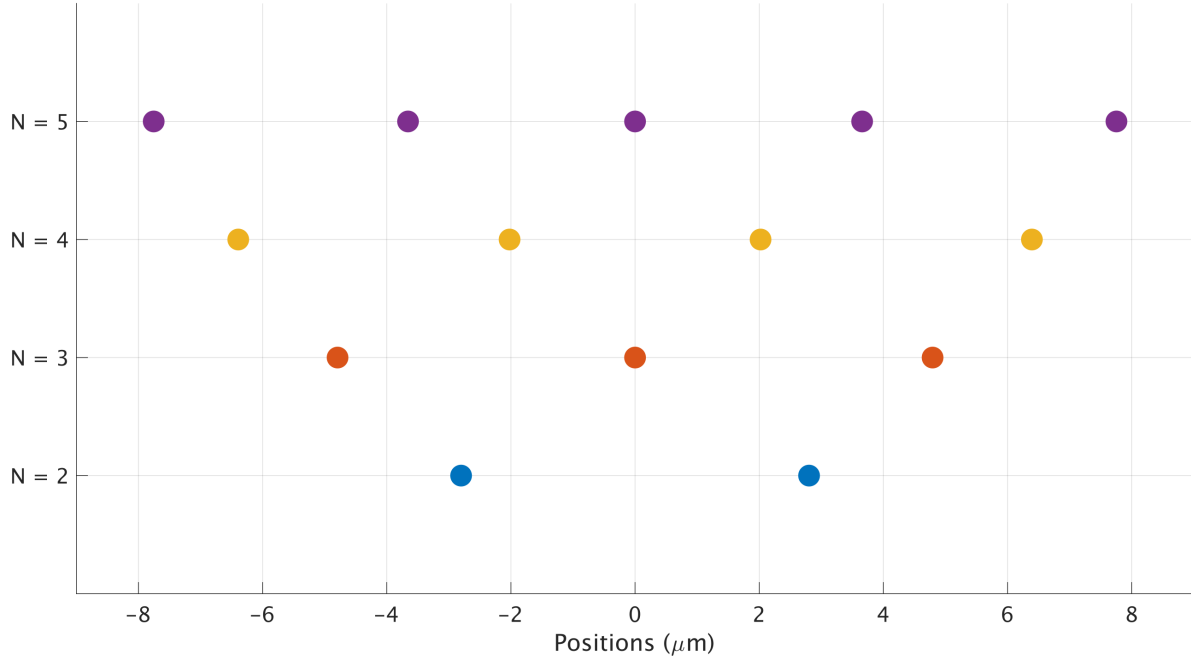


**Figure 2.3.2:** Ion position for different number  $N$  of ions in the trap. The trap frequency is  $\omega_z = 2\pi \times 1$  MHz.

### 2.3.3 Doppler cooling

Coherent manipulation of ions requires cooling them to reach at least the Lamb Dicke regime [46], where the extent of the ion wave packet is much smaller than the optical wavelengths of the lasers. The idea comes from neutral atoms [47] and can be applied to ions as well: a laser interacts with a particular transition, causing photon absorption from the laser by the atom, giving a momentum kick  $\Delta p = \hbar\mathbf{k}$  in the direction of the laser beam to the ion. The absorbed photon is emitted through spontaneous emission in a random direction, giving another kick to the ion. Over many cycles of absorption and emission, the random kick due to emission will average to zero (although presents a heating process which sets the Doppler limit), while the kick given by the laser will slow down and cool the ion in the direction of the laser.

The mathematical model is a 2-level atom interacting with a laser (Rabi frequency  $\Omega$ , and detuning  $\Delta$ ) as described in Section 2.1.2. Spontaneous emission is included with the master Equation (2.1.25), where  $\Gamma$  is the spontaneous emission rate. The master equation can be explicitly written for every component of the density matrix  $\rho_{ij}$ , in the rotating frame they are called optical Bloch equations [48]. Following the approach of [49], the system reaches equilibrium when  $\rho_{ee}(t \rightarrow \infty)$ :

$$\rho_{ee}(t \rightarrow \infty) = \frac{\Omega^2/\Gamma^2}{1 + \left(2\frac{\Delta-\mathbf{k}\cdot\mathbf{v}}{\Gamma}\right)^2 + 2\frac{\Omega^2}{\Gamma^2}} \quad (2.3.11)$$

where  $\mathbf{v}$  the velocity of the ions. The force exerted on the ions, due to the radiative pressure, is proportional to  $\rho_{ee}$  as

$$F = \hbar k \Gamma \rho_{ee} \simeq F_0 + \frac{dF}{dv} v = \hbar k \Gamma \frac{\Omega^2}{\Gamma^2 + 4\Delta^2} + F_0 \frac{8k\Delta}{\Gamma^2 + 4\Delta^2} v \quad (2.3.12)$$

where we assumed low velocities  $v \simeq 0$  and thus linearized the equation. The effect of the constant term in the force is just to displace the ion from its central position. Instead, the linear term acts as a viscous friction that cools the ions with a rate of  $\dot{E}_c = \langle Fv \rangle$ . If on one side spontaneous emission allows for Doppler cooling, it also sets the lower limit. The small fluctuations in the Brownian motion leads to diffusion which heats the ion at a rate of

$$\dot{E}_h = \frac{1}{m} \frac{d}{dt} \langle p^2 \rangle = \frac{1}{m} (\hbar k)^2 \Gamma \langle \rho_{ee}(v) \rangle. \quad (2.3.13)$$

At equilibrium, the heating rate equals the cooling rate giving the lowest temperature achievable

$$\dot{E}_h + \dot{E}_c = 0 \implies k_B T = -\frac{\hbar \Gamma}{4} \left( \frac{\Gamma}{2\Delta} + \frac{2\Delta}{\Gamma} \right). \quad (2.3.14)$$

From here it is clear that by choosing the appropriated detuning, it is possible to reach the lowest temperature

$$T_{min} = \frac{\hbar \Gamma}{2k_B}, \quad \text{for } \Delta = -\frac{\Gamma}{2}. \quad (2.3.15)$$

At this temperature, the average phonon number is  $\langle \hat{n} \rangle = \Gamma / 2\omega_z$  [50].

As an example, a single calcium ion confined in a trap with  $\omega_z = 2\pi \times 1$  MHz, can be cooled using the transition  $|S_{1/2}\rangle \rightarrow |P_{1/2}\rangle$  ( $\Gamma = 2\pi \times 20.8$  MHz), the 2-level atom model in this case gives a good estimation, even though calcium has more levels. The Doppler temperature is  $T_{min} \sim 500 \mu\text{K}$ , and the corresponding average phonon number is  $\langle \hat{n} \rangle = 10.4$ . The wavefunction extent for this phonon number can be found as the standard deviation of the operator  $\hat{z}$  for the vibrational state  $|n\rangle$

$$\sigma_z = \sqrt{\langle \hat{z}^2 \rangle} = \sqrt{\frac{\hbar}{2m\omega_z} (1 + 2\langle \hat{n} \rangle)} \simeq 52 \text{ nm}. \quad (2.3.16)$$

Such a Doppler cooled ion has therefore a spatial dimension still much smaller than the ion separations and the wavelength of the relevant lasers.

To further decrease  $\langle \hat{n} \rangle$ , sideband cooling can be used [50], here particular sideband transitions are excited to reduce the phonon number of the ions inside the trap. However in the experiments of this thesis, only Doppler cooling has been performed.

## 2.4 Laser beam

### 2.4.1 Gaussian beams

Typically, lasers emit light in the shape of Gaussian beams, so it is import to understand what Gaussian beams and their characteristics are. In this chapter we will take a closer look into such beams and introduce important quantities to characterize a Gaussian beam.

From a theoretical point of view, Gaussian beams are a solution of the Helmholtz equation  $(\nabla^2 + k^2)U(\mathbf{r}) = 0$ , with  $k$  being the wavevector, and  $U(\mathbf{r})$  the complex electric field. If we can consider a wave propagating in the  $z$  direction, we can write  $U(\mathbf{r})$  as [51]:

$$U(\mathbf{r}) = A_0 \frac{W_0}{W(z)} \exp \left\{ -\frac{x^2 + y^2}{W^2(z)} \right\} \exp \left\{ -ikz - ik \frac{x^2 + y^2}{2R(z)} + i \arctan(z/z_0) \right\}. \quad (2.4.1)$$

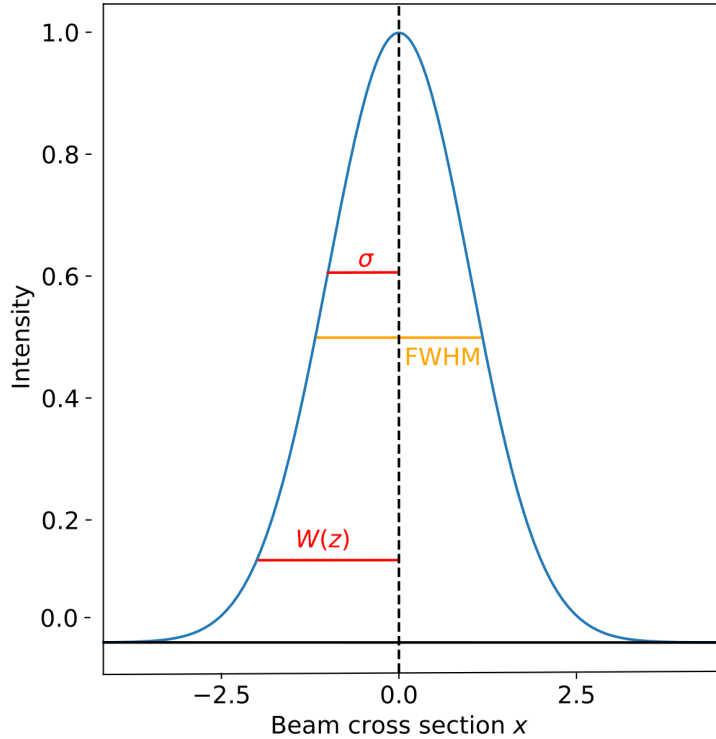


**Figure 2.4.1:** Cross section of the intensity profile of a Gaussian beam  $I(x) = e^{-x^2/2\sigma^2}$ . The beam intensity is normalized and  $\sigma = 1$ . Graphical representations of used widths:  $W(z)$  is defined as the point at which the intensity  $I$  has fallen to  $1/e^2 = 13.5\%$  of its maximum value;  $\sigma$  is the standard deviation of a Gaussian in the form  $Ae^{-\frac{x^2}{2\sigma^2}}$ ; FWHM is the full width half maximum. Relationships among these quantities are:  $W(z) = 2\sigma$ , and  $W = 0.84 \cdot \text{FWHM}$ .

Where  $A_0$  is an amplitude,  $W(z)$  the width,  $R(z)$  the curvature radius, and  $z_0$  the Rayleigh range. The intensity can be calculated by taking the square of the complex amplitude

$$I(\mathbf{r}) = |U(\mathbf{r})|^2 = I_0 \left( \frac{W_0}{W(z)} \right)^2 \exp \left\{ -\frac{2x^2 + 2y^2}{W^2(z)} \right\} \quad I_0 = |A_0|^2. \quad (2.4.2)$$

For a fixed  $z$ , the sections in the  $x - y$  plane are shaped as a two dimensional Gaussian distribution. For simplicity, let us take the profile for a fixed  $z$  and  $y = 0$ :

$$I(x, y = 0, z) = \tilde{A}(z) \exp \left\{ -\frac{2x^2}{W^2(z)} \right\} \quad \tilde{A}(z) = I_0 \left( \frac{W_0}{W(z)} \right)^2. \quad (2.4.3)$$

In Figure 2.4.1, the  $x$  cross section is depicted for this intensity profile normalized in amplitude. Parameters used to measure the width are also displayed and defined in the caption. All of those quantities are equivalent and differ only by a prefactor, so for the rest of the section, we stick to  $W(z)$  (point at which  $I$  has fallen to  $1/e^2 = 13.5\%$ ) and study its behaviour. From the Helmholtz equation [51], the profile of  $W(z)$  as a function

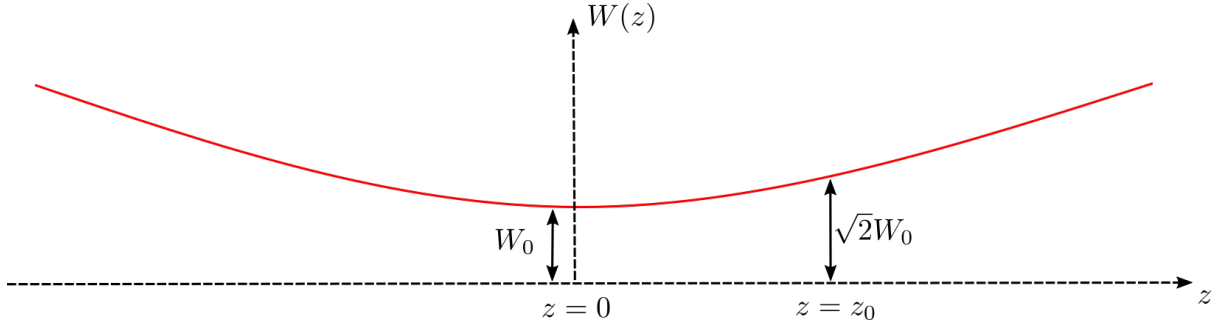


**Figure 2.4.2:** Width profile of a Gaussian beam along the direction of travel of the beam, Equation (2.4.4). The beam is focused at the position  $z = 0$ , here it assumes the minimum width  $W_0$ , also referred to as the waist.  $z_0$  is the Rayleigh range where the width is  $\sqrt{2}W_0$

of  $z$  is found to be

$$W(z) = W_0 \sqrt{1 + \left(\frac{z}{z_0}\right)^2} \quad W_0 = \sqrt{\frac{\lambda z_0}{\pi}} \quad z_0 = \frac{\pi W_0^2}{\lambda}. \quad (2.4.4)$$

A plot of Equation (2.4.4) is presented in Figure (2.4.2): the width  $W(z)$  assumes its minimum value  $W_0$  at  $z = 0$ . This position is called the beam focus and its width  $W_0$  is the waist of the beam.  $z_0$  gives an idea of how quickly the beam is expanding. Mathematically,  $z_0$  is the distance between the focus and the point where the width is  $W(z) = \sqrt{2}W_0$ .  $z_0$  is commonly referred to as Rayleigh range. For  $z \gg z_0$ , the beam profile diverges almost linearly with an angle given by  $\theta = W_0/z_0$ , which means the smaller the focus, the greater it diverges.

This property will become important later in the work, because it provides one limit on the waist of the beam in our experimental system. The optical aperture of the trap is limited by some electrodes, and a beam that diverges too rapidly can potentially clip on one electrode causing aberrations and scattered light in the trap.

A Gaussian beam can be reshaped using optical elements. In order to study such reshaping, let us consider a thin spherical lens with focal length  $f$  placed at position  $z$ . The effect of the lens on the beam is to give an extra phase factor  $k(x^2 + y^2)/2f$  to Equation (2.4.1) [52]. We can match the phase of the incoming and emerging waves, which have respectively radius of curvature  $R$ , and  $R'$ , this results in

$$\frac{1}{R'} = \frac{1}{R} - \frac{1}{f}. \quad (2.4.5)$$

The effect of the lens is to change the radius of curvature to  $R'$ . Moreover, the width of the beam at the lens is not altered  $W = W'$ . Using these last two facts, we can determine all the parameters of the outgoing wave. The most important for us is the new waist  $W'_0$

$$W'_0 = M W_0 \quad M = \frac{M_r}{\sqrt{1 + r^2}}. \quad (2.4.6)$$

Where  $M_r = \left| \frac{f}{z-f} \right|$ , and  $r = \frac{z_0}{z-f}$ .  $M$  is the magnification factor which provides an easy way to describe the change of the beam. For a better understanding of this last result,

let us consider a less general example. We place the lens at the focus  $z = 0$ , and have a collimated beam  $z_0 \rightarrow +\infty$ . In this case the new waist is

$$W'_0 = \frac{W_0}{\sqrt{1 + (z_0/f)^2}} \simeq W_0 \frac{f}{z_0} = \frac{\lambda f}{\pi W_0} \quad (2.4.7)$$

where the approximation comes from taking  $z_0 \gg f$ . There are three parameters we can act on to achieve the smallest waist. A shorter wavelength  $\lambda$  results in a smaller waist. Similarly, a lens with a shorter focal length  $f$  reduces the waist. Finally, a broader incoming beam, i.e. larger  $W_0$ , also narrows the waist. Given a certain lens and a wavelength, the smallest waist is obtained with the largest incoming beam which is limited by the lens diameter  $D$ , i.e.  $2W_0 = D$ . In this case, equation 2.4.7 becomes

$$W'_0 = \frac{2\lambda}{\pi} \frac{f}{D}. \quad (2.4.8)$$

If the size of the collimated beam is further increased, the lens becomes a finite size aperture and diffraction effects will appear at the image plane. In general, an optical system (in our example a single lens) that is limited in the sense of (2.4.8) is said to be diffraction limited [53].

## 2.4.2 Beam steering via Acousto-optical Deflectors

An acousto-optical deflector (AOD) is a common device that can change the propagation direction of a laser beam, typically on the few microsecond timescale. In this work we use an AOD to change which ion is illuminated by a laser focused on a single ion. The working principle of an AOD is based on the Acousto-optical effect. A piezo is used to create acoustic waves that propagate through a crystal. The waves modify the crystal refractive index, creating a periodic optical grating that can deflect light travelling through it.

Following the approach of [51] to model the device, let us consider a rectangular crystal like in Figure 2.4.3. The acoustic wave creates a sinusoidal pattern with frequency  $\Omega_s$  and wavenumber  $q$ , for the refractive index  $n(x, t)$

$$n(x, t) = n - \Delta n_0 \cos(\Omega_s t - qx), \quad (2.4.9)$$

where  $n$  is the refractive index of the unperturbed medium,  $\Delta n_0$  is the amplitude of the perturbation.  $\Delta n_0$  is proportional to the square root of the sound intensity. The refraction<sup>1</sup>  $r$  can be calculated by dividing the crystal in thin layers with thickness small compared to the acoustic wavelength. We assume that the refractive index  $n(x)$  is approximately constant across the layer. The total refraction is given by all the contributions  $dr/dx$  of every layer, we can therefore integrate in the  $x$  direction over the length  $L$  (see Figure 2.4.3) as follows:

$$r = \int_{L/2}^{L/2} e^{i2kx \sin \theta} \frac{dr}{dx} dx \quad (2.4.10)$$

The included phase  $e^{i2kx \sin \theta}$  takes into consideration the different phase of the input laser beam when different layers are met. The integral can be solved with a change of variable  $dr/dx = q\Delta n_0 \sin(\Omega_s t - qx) dr/dn$ . The sine function can be written as exponential and

---

<sup>1</sup>defined as  $E_r/E_i = r$ , where  $E_r$  is the refracted electric field, and  $E_i$  is the input field

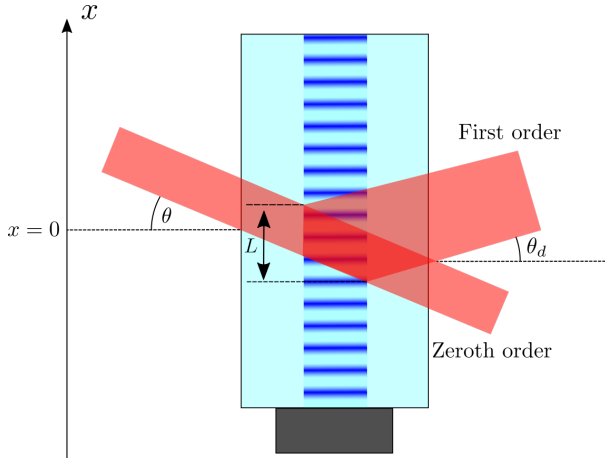


**Figure 2.4.3:** Simple model of an AOD. In black at the bottom a black piezo that generates acoustic waves through the light blue crystal. In red, a collimated beam of light enters in the crystal with an angle  $\theta$  and gets partially deflected at an angle  $\theta_d$  due to the interaction with the effective optical grating created by the acoustic waves.  $L$  is the interaction length.

now the integral contains only exponential functions which are straightforward to calculate [51]. At the end we obtain two contributions for the refracted wave  $r$ :

$$r = r_+ + r_- \quad r_{\pm} = \pm i r_0 \text{sinc} \left[ (2k \sin(\theta) \mp q) \frac{L}{2\pi} \right] e^{\pm i \Omega_s t} \quad (2.4.11)$$

These two terms are the plus and minus first order diffraction, an acousto-optical device can be operated symmetrically entering either with a positive angle or with a negative one. We will focus only on the positive term. The sinc function peaks sharply when its argument is 0, i.e. at  $2k \sin \theta = q$ , and then quickly decreases as the angle is changed. Hence, the input beam must enter with a particular angle  $\theta_B$  in order to diffract with maximum efficiency. The condition to be satisfied can be written as a function of the optical ( $\lambda$ ) and acoustic ( $\Lambda_s$ ) wavelengths as

$$\sin \theta_B = \frac{\lambda}{2\Lambda_s} \quad \Lambda_s = \frac{2\pi}{q}. \quad (2.4.12)$$

This equation is called Bragg condition, and  $\theta_B$  is referred to as the Bragg angle. If the Bragg condition is satisfied, the diffraction angle  $\theta_d$  is equal to the incident angle  $\theta_B = \theta = \theta_d$  [54]. If the condition is not perfectly matched, some light will not be diffracted and will be transmitted unaltered through the device. The ratio of the transmitted and diffracted light gives an idea of how well an acousto-optical device is performing and takes the name of diffraction efficiency.

From Equation (2.4.11) we can notice that an extra phase factor proportional to  $\Omega_s t$  is added to the reflected wave. Thus, if the incoming wave is oscillating at  $\propto e^{i\omega t}$ , the diffracted wave will oscillate as  $\propto r_+ e^{i\omega t} \implies \propto e^{i(\omega + \Omega_s)t}$ . The frequency of the diffracted optical wave  $\omega_r$  is therefore shifted by the frequency of the acoustic vibration as

$$\omega_r = \omega + \Omega_s. \quad (2.4.13)$$

The acousto-optical effect described above is common to different devices optimized for specific tasks. Two of the most common devices are Acousto-optical Deflectors (AOD) and Acousto-optical Modulators (AOM). The idea of the latter is to shift the frequency of a laser using Equation (2.4.13). Deflectors instead aim to shift the direction of the beam by exploiting the fact that the diffraction angle  $\theta_d = \theta$  changes linearly as a function of the acoustic frequency  $\Omega_s$ . Assuming that the angle  $\theta$  is small enough to approximate  $\sin \theta \sim \theta$ , the Bragg condition can be written as

$$\theta \simeq \frac{\lambda}{2v_s} f, \quad (2.4.14)$$

where  $v_s$  is the speed of sound and  $f$  the frequency of the acoustic wave. We can already see that if we change the frequency  $f$ , the deflection angle  $\theta$  changes proportionally. The bandwidth  $B$  specifies the range of frequencies over which deflectors work. Assuming that the maximum diffraction angle is  $\Delta\theta$ , Equation (2.4.14) can be written as [55]

$$\Delta\theta \simeq \frac{\lambda}{2v_s} B, \quad (2.4.15)$$

It is clear from this equation that, in order to increase the bandwidth, i.e. increasing  $\Delta\theta$ , slower acoustic velocities are preferred. AODs are therefore optimized by choosing a crystal and an acoustic mode with low acoustic velocities compared to AOMs [56].

## 2.5 Basic model of key experiments

To fulfill the goals of this thesis we perform two key experiments with ions: single-ion qubit manipulation and single-ion photon generation. This section presents a short overview of those key experiments, using the theory introduced in the previous sections.

### 2.5.1 Addressed qubit manipulation

As highlighted in Figure 2.5.1, the qubit is encoded in the  $|S\rangle$  and  $|D\rangle$  states. The 393 nm transition from  $|S\rangle \rightarrow |P\rangle$  can be used to induce a phase shift on the ground state of the qubit  $|S\rangle$ . In the off-resonant regime, the laser induces an AC Stark shift  $\delta = \Omega^2/4\Delta$  (see Section 2.1.2) on the  $|S\rangle$  and  $|P\rangle$  states with negligible excitation of the  $|P\rangle$  state. The effect of such AC Stark shifts on the qubit is to shift the relative phase between  $|S\rangle$  and  $|D\rangle$  as shown below. As discussed in Section 2.1.2.2, in order to reduce spontaneous scattering in comparison to AC Stark shift, we should have  $\delta \gg \Gamma_{eff}$ . Therefore in the experiment we decided to set the detuning such that the ratio between the Stark shift and the spontaneous scattering rate is 100

$$\frac{\delta}{\Gamma_{eff}} = \frac{2\Delta}{\Gamma} \sim 100 \implies \Delta \sim 3 \text{ GHz}. \quad (2.5.1)$$

By measuring the state of all ion qubits individually, and scanning the beam across the ions string, a beam profile can be obtained. In a single experiment we can therefore characterize the beam and demonstrate qubit manipulation. In summary, the qubit begins in the  $|S\rangle$  state, then the idea is to send a resonant  $\pi/2$  pulse at 729 nm, which brings the qubit state to a superposition  $|S\rangle + |D\rangle$ , a second identical pulse would bring the

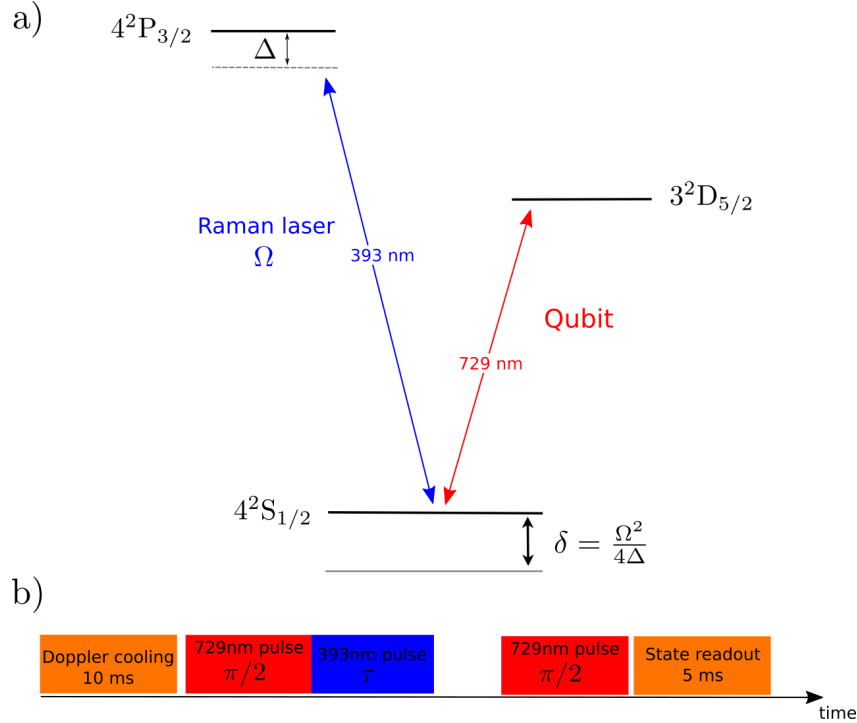


**Figure 2.5.1:** a) Relevant levels for the experiment, the qubit is encoded in the 729 nm transition, the 393 nm laser is used to shift the  $|S\rangle$  level via AC Stark shift b) Experiment pulse sequence, Doppler cooling and state readout are described in Section 3.1.2. The time  $\tau$  had a variable length.

final state to the excited level  $|D\rangle$ . However, if between the two 729 nm pulses, an AC stark shift is induced by a pulse of 393 nm light, an additional phase is added to the superposition. The phase of the second  $\pi/2$  pulse is left as a variable to be scanned, as considered below. Rigorous mathematics can be done with matrices  $U_{729}$  (Equation (2.1.15)) and  $U_{393}$  (Equation (2.1.20)). After the three pulse sequence the final state is

$$\begin{aligned} |\psi_f\rangle &= U_{729}(\pi, \phi) U_{393}(\delta) U_{729}(\pi, 0) |S\rangle \\ &= \frac{1}{2} \left( e^{-i\frac{\delta}{2}\tau} - e^{-i\phi} \right) |S\rangle - \frac{i}{2} \left( 1 + e^{-i\frac{\delta}{2}\tau} e^{-i\phi} \right) |D\rangle \end{aligned} \quad (2.5.2)$$

where  $\delta = \Omega^2/4\Delta$  is the Stark shift, and  $\Omega$  the Rabi frequency of the 393 nm light. The final probability to find the excited state  $|D\rangle$  is then

$$P_D = \cos^2 \left( 2\phi + 2 \frac{\delta\tau}{2} \right) = \cos^2 \left( 2\phi + \frac{\Omega^2\tau}{4\Delta} \right). \quad (2.5.3)$$

As we can see,  $P_D$  depends on the phase of the second 729 nm pulse  $\phi$  and on the Stark shift induced by the 393 nm laser. To get  $\Omega^2$  a simple formula inversion can be done

$$\Omega^2 = \frac{4\Delta}{\tau} \left[ \arccos \left( \sqrt{P_D} \right) - 2\phi \right]. \quad (2.5.4)$$

The phase  $\phi$  can be set experimentally. The experiment shows that ion-qubits can be used as sensitive tools for beam profiling and takes the name of Ramsey interferometry [57].

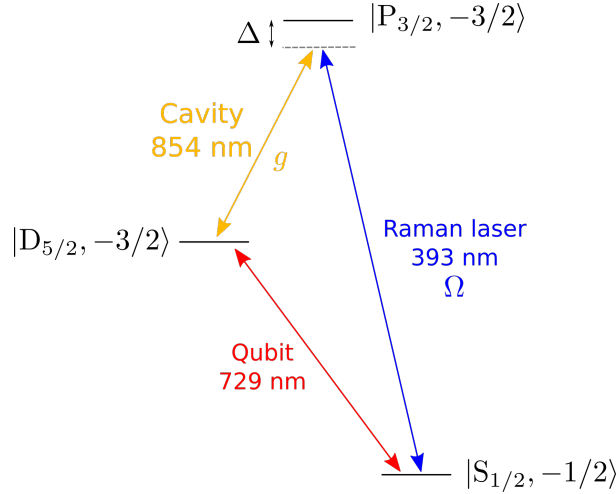


**Figure 2.5.2:** Scheme of the Raman process used to generate photons, via a cavity enhanced Raman process (Section 2.2.3). The electron in the  $|S\rangle$  state is excited to the  $|D\rangle$  level by absorbing a 393 nm photon and emitting a 854 nm photon in the cavity.

## 2.5.2 Addressed photon generation

The second key experiment consists of generating photons from one ion out of a string, using the cavity-mediated Raman process described in Section 2.2.3. In Figure 2.5.2 the relevant levels are depicted. First, the ion is positioned in a maximum of the cavity vacuum electric field such that the atom-cavity coupling  $g$  is maximized. Second, a 393 nm laser pulse triggers the generation of a photon into the cavity through the Raman process. As seen in Section 2.2.3, for the process to be stronger than the spontaneous scattering rate, we choose a detuning of  $\Delta \sim 400$  MHz. In this case, the effective Rabi frequency  $\Omega_{eff}$  (Equation (2.2.7)) is larger than the effective spontaneous scattering rate  $\Gamma_{eff}$  (Equation (2.2.8)).

In the ideal case, the population of the state  $|S\rangle$  is coherently transferred to the  $|D\rangle$  state by absorbing a 393 nm photon and emitting an 854 nm photon into the cavity, the photon then exits from the cavity out of a preferred mirror (with higher transmission). We perform the experiment using the following states

$$|S_{1/2}, -1/2\rangle \rightarrow |P_{3/2}, -3/2\rangle \rightarrow |D_{5/2}, -3/2\rangle. \quad (2.5.5)$$

These transitions are polarization dependent, the absorbed photon is  $\sigma_-$  polarized, while a  $\pi$  polarized photon is emitted. Since the magnetic field is orthogonal to the cavity, the  $\pi$  polarized photon is projected into a linearly polarized cavity photon.

Note that the effective Rabi frequency of the population transfer is proportional to the Rabi frequency  $\Omega$  as seen in Equation (2.2.7) and the AC Stark shift depends on the intensity  $\Omega^2$ . Therefore, the interaction of the addressed beam with the ion string in the Ramsey interferometry and in the photon generation experiment is different.

# Chapter 3

## Experimental system and techniques

In this chapter, the essential parts of the already existing setup on top of which the addressing system has been built are described. Calcium-40 ions are used in the experiment and the implementation of several techniques for trapping and manipulating these ions are discussed. Furthermore, the addressing setup utilizes 393 nm light and the laser emitting this light was already installed by H. Hainzer<sup>1</sup> [36], thus that setup is briefly presented. Finally, the experiment can be controlled remotely via computers, an overview of how it is implemented is also given.

### 3.1 Ion trap and key techniques

#### 3.1.1 Calcium Ions

Ions with a single valence electron are attractive given their simple level schemes and straightforward cooling schemes, examples include beryllium [58], barium [59], strontium [60], calcium [18], ytterbium [61], and magnesium [62]. In our experiment we trap  $^{40}\text{Ca}^+$ , the most abundant isotope of calcium. In Figure 2.1.2 the level scheme of the valence electron is presented. There is no hyperfine structure as  $^{40}\text{Ca}^+$  does not possess a nuclear spin. Two short lived excited states  $P_{1/2}$ , and  $P_{3/2}$  ( $1/\Gamma \sim 7.7$  ns, and  $1/\Gamma \sim 7.4$  ns, respectively) are connected to S via dipole transitions. Due to the short lifetimes of these two states, they are suitable for laser cooling and state detection. The states  $D_{3/2}$  and  $D_{5/2}$  are metastable ( $1/\Gamma \sim 1$  s) and are coupled to the S state via electric quadrupole transitions. An optical qubit can be implemented in the states  $S_{1/2}$  and  $D_{5/2}$ , as the lifetime of the  $D_{5/2}$  state is longer than typical operation times [63]. Other choices for qubit implementations have been explored, for instance in the Zeeman levels of the  $S_{1/2}$  manifold [64]. Table 3.1.1 summarizes details about the different transitions, and what they are used for. A more detailed description and implementation is discussed in the next section.

---

<sup>1</sup>In Helene's master project, the 393 nm laser (MSquared Ti:Sa) and the ion cavity were locked to an ultrastable reference cavity. The linewidth of the MSquared Ti:Sa laser was measured to be <100 Hz with a drift rate of 202(1) mHz/s

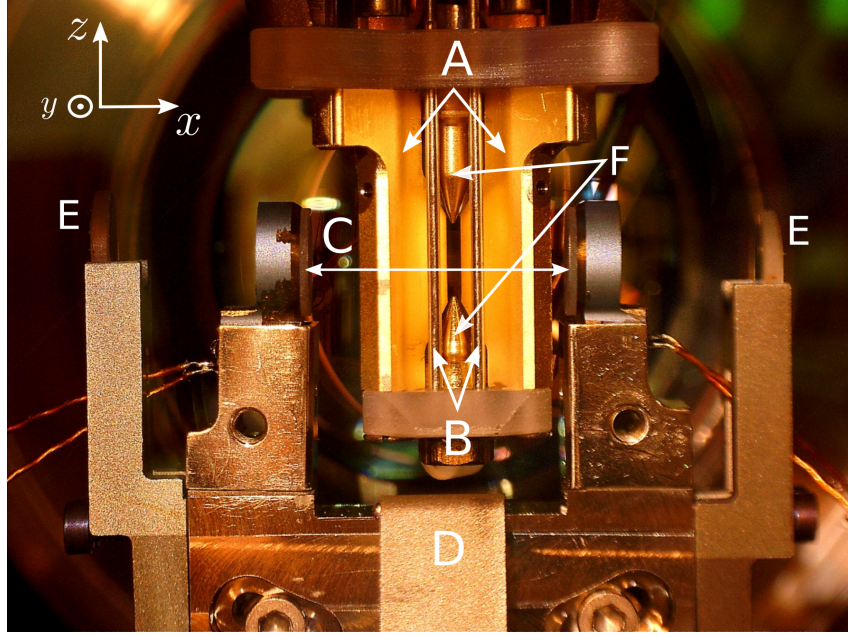


**Figure 3.1.1:** Photo of the mounted trap. The axial direction is defined along the  $z$  axis, while radial is  $r^2 = x^2 + y^2$ . Highlighted in the image there are: (A) Trap's golden blades for radial RF confinement (B) One pair of compensation electrodes (C) Cavity mirrors, The left mirror is highly reflective, the right mirror is the 854 nm photon output mirror (see Section 2.2.2), separation is  $\sim 20$  mm (D) Calcium atomic oven (E) Collimation lenses (F) Static voltage endcaps for axial confinement.

Transition	$\lambda$ (nm)	Decay rate $\Gamma$	Lifetime $\tau$	BR	Main use here
$S_{1/2} \leftrightarrow P_{1/2}$	396.847	$2\pi \times 20.8$ MHz	7.7 ns	94%	Cooling and imaging
$S_{1/2} \leftrightarrow P_{3/2}$	393.366	$2\pi \times 21.4$ MHz	7.4 ns	94%	Photon generation
$S_{1/2} \leftrightarrow D_{3/2}$	732.389	$2\pi \times 0.132$ Hz	1.080 s	-	-
$S_{1/2} \leftrightarrow D_{5/2}$	729.147	$2\pi \times 0.136$ Hz	1.045 s	-	Manipulate optical qubit
$P_{1/2} \leftrightarrow D_{3/2}$	866.214	$2\pi \times 1.70$ MHz	94.3 ns	6%	Repumping
$P_{3/2} \leftrightarrow D_{5/2}$	854.209	$2\pi \times 1.34$ MHz	101 ns	5.3%	Cavity photon
$P_{3/2} \leftrightarrow D_{3/2}$	849.802	$2\pi \times 1.52$ MHz	902 ns	0.6%	-

**Table 3.1.1:** Transitions in  $^{40}\text{Ca}^+$  and current use in the experiment.  $\lambda$  is the wavelength of the transition, and BR is the branching ratio for the different decay channels. Values are taken from [44, 65]

### 3.1.2 Trapping, cooling, and state readout

In this section we discuss how to implement important techniques for ion based quantum computing and we present further key parameters of our experiment.

#### TRAPPING AND LOADING

Our trap is a linear 3D RF Paul trap as depicted in Figure 3.1.1 where main components are highlighted. The electrodes are made of titanium and are coated in gold. The trap itself is mounted vertically on a shappire holder. The endcaps are 5 mm apart and

are usually kept at voltages on the order of 500-1000V, which results in single-ion axial frequencies of  $\omega_z \sim 2\pi \times 0.7 - 1$  MHz respectively. The four blades are 0.08 mm from the center of the trap and driven with an RF of  $\sim 24$  MHz. The RF signal from an amplifier is impedance matched with the trap using a quarter-wave bulk helical resonator (not shown). The trap also includes three pairs of electrodes that can be used to compensate for stray electric fields. The location of the compensation electrodes, with respect to the trap, is presented later in Figure 4.3.4.

Loading of ions is done with a resistively-heated oven: calcium is heated and directed towards the trap, where neutral atoms undergo 2-stage photon ionization. First, a 422 nm laser resonantly excites one electron to the  $4p^1P_1$  state, while a second 375 nm laser, brings the electron to free space, ionizing the atom [66]. This two stage process allows for isotope selection ionizing only  $^{40}\text{Ca}$ . Loading usually takes minutes or tens of minutes depending on the number of ions one wants to load. Storage time can be in the order of days, especially when a single ion is loaded.

### DOPPLER COOLING AND FLUORESCENCE IMAGING

Once loaded, ions are laser-cooled to the Doppler limit with 397 nm light on the transition  $S_{1/2} \leftrightarrow P_{1/2}$  (Section 2.3.3). An additional 866 nm repumper on the transition  $P_{1/2} \leftrightarrow D_{3/2}$  is used to avoid the electron being stuck in the  $D_{3/2}$  state. For typical experiments a stage of Doppler cooling is always included, typically lasting for a few milliseconds.

With the same lasers used for Doppler cooling, ion imaging and state readout are also done. The light shines on the ions exciting the transition  $S_{1/2} \leftrightarrow P_{1/2}$  driving the electron to the excited state, which then decays spontaneously emitting photons. A fraction of the scattered 397 nm photons is collected with a custom objective with NA of  $\sim 0.289$ , which means a maximum possible efficiency of 2.5 % of the solid angle  $4\pi$ . The objective focuses the collected photons 1.5 meters away where a CCD camera (Andor iXon Ultra 897) is placed. The geometrical path of the imaging photons is displayed in Figure 3.1.2, this setup has a magnification factor of  $\sim 18.6$ . The same objective is also used for the addressing setup built within this thesis. Therefore, the imaging optical path must be partially shared with the newly built addressing. More details of the objective are given in Section 4.2.

### STATE READOUT WITH CAMERA

Consider a qubit encoded in the states  $S_{1/2}$  and  $D_{5/2}$ , if the imaging laser is switched on, the electron will be projected either to the  $S_{1/2}$  level or to the  $D_{5/2}$ . In the first case, photons are scattered from the ion and collected on the camera, in the second case the electron is shelved and will not scatter any photon. Hence, the two cases are distinguishable by the brightness of the ion image on the camera. The camera can spatially separate the ions and therefore distinguish the individual state of each ion in the string. In order to perform this task, the camera software<sup>2</sup> needs initial calibration. This means that a region of interest, where the fluorescing ions are, is first manually selected. The program takes the image in that region, integrates spatially in one direction (perpendicular to the string) and fits a number of Gaussians equal to the number of ions, where the central value of each peak indicates the position of each ions. The software then determines the brightness in one standard deviation interval and compares it with a previously set threshold determining ultimately the ion state. We thank Daniel Heinrich for developing this software.

---

<sup>2</sup>Home developed software that works together with TrICS, see Section 3.3

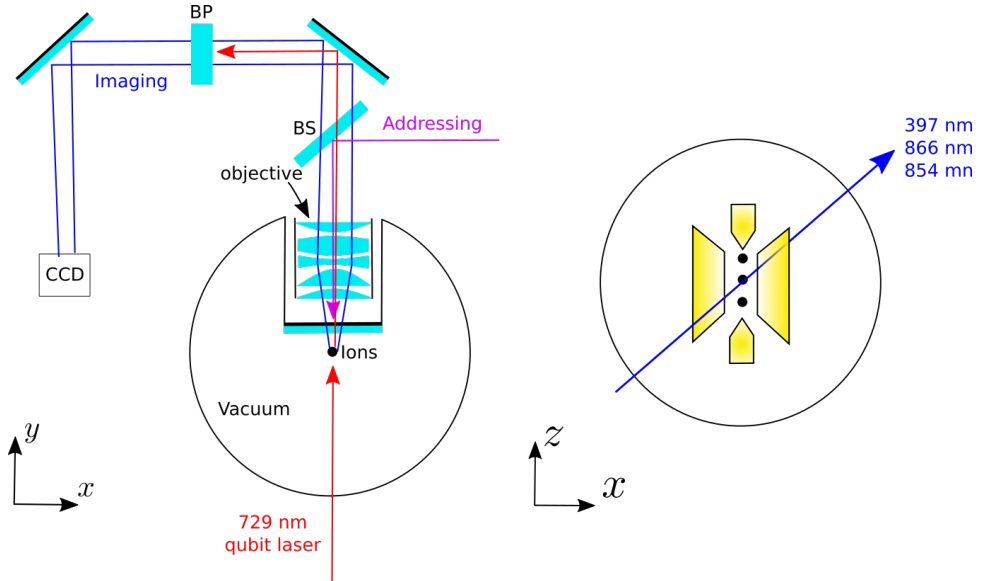


**Figure 3.1.2:** Left: top view of our ion trap system, an out-of-vacuum objective collimates and focuses the scattered 397 nm photons for imaging onto the CCD camera  $\sim 1.5$  m away from the ions. The addressing setup must share part of this path, as the same objective is used for focusing the 393 nm laser. A beam splitter (BS), installed during the course of this thesis, separates the imaging path from the addressing path. More details about the addressing path are in Section 4.1. A bandpass filter (BP) blocks the 729 nm light such that only 393 nm light can reach the camera. Right: front view of the trap, other laser directions are depicted.

## 3.2 393 nm laser

The laser used to drive the addressed Raman transition is at 393 nm. This light is obtained from a titanium-sapphire laser from MSquared. The laser is optically pumped with 8 W of light at 532 nm from a Lighthouse Photonics Sprout laser. The Ti:Sa crystal is contained in a cavity in a bow tie configuration, together with an optical diode, etalon, birefringent mirror, and tunable cavity mirror for frequency tuning and stabilization. The laser can be frequency locked to a wavemeter or to an external cavity.

The fundamental light is set to 786 nm with tunability ranging from 725 nm to 875 nm that can be controlled remotely with a computer. The fundamental light is frequency doubled to 393 nm via an MSquared ECD-X external cavity resonant doubler accessory module. 393 nm light can be obtained with up to 1 W of power. Before reaching the ion trap, 393 nm light is sent through the setup in Figure 3.2.1. The setup contains two paths: one resonant with the  $S_{1/2} \leftrightarrow P_{3/2}$  transition, which goes directly to the ion; and a second path, where the light is detuned by -380 MHz for exciting the Raman transition described in Section 2.2.3.

The introduction of an AOD in the addressing setup shifts the light by  $-125 \pm 25$  MHz. As we want to work around -400 MHz to excite the Raman transition, the setup in figure 3.2.1 had to be slightly altered to compensate for the additional AOD shift: AOM 2 was switched from -1 order to +1 order, and then driving frequencies were changed to 180 MHz for AOM 1 and 70 MHz for AOM 2.

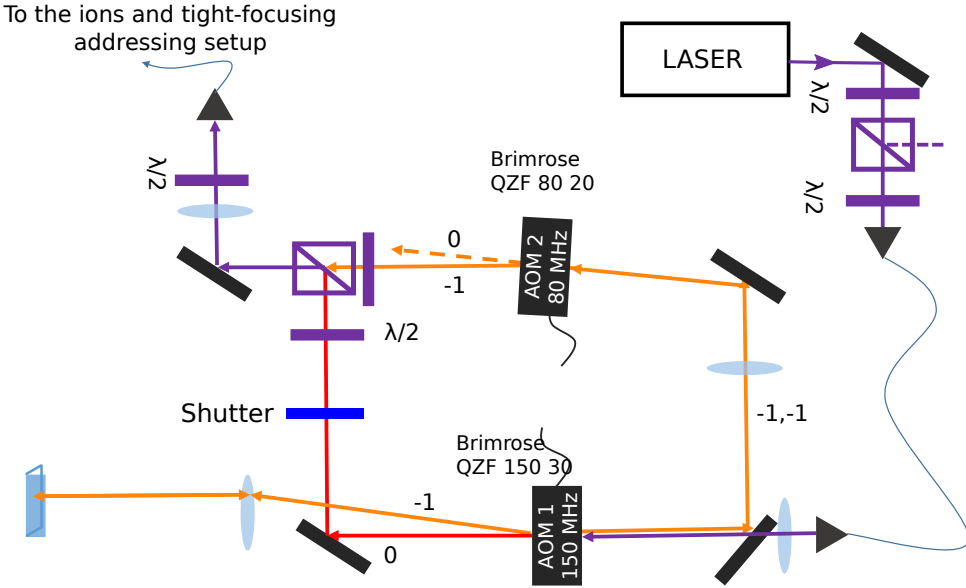


**Figure 3.2.1:** 393 nm laser optical setup before installation of the addressing system (a slight modification was required, see text). Two paths are present: a resonant path on the  $S_{1/2} \leftrightarrow P_{3/2}$  transition (in red), and a detuned path (in orange) where a double pass AOM introduces -300 MHz shift, and a single pass AOM an additional -80 MHz. Paths are overlapped on a beam splitter and coupled to a fiber. A shutter can be used to block the resonant path. Numbers on the paths indicate diffraction order, above each AOM the model, central frequencies and bandwidths are shown, respectively. Setup built by V. Krutianskii, image made by him and adapted for this thesis.

### 3.3 Experiment control

Our trapped-ion experiments require control over a large network of AOMs and other devices. Furthermore, precise control of the laser phase between sequential laser pulses, at the point of the ion, is also required, e.g. in the Ramsey experiments presented in this thesis. The need of fast and coherent pulse control is fulfilled by an electronic system that can be controlled with software on a central computer, from which every device connected to the network can be controlled. The experiment control network is sketched in Figure 3.3.1. The main components are:

- A computer: from here the experiment is controlled with TrICS (Trapped Ion Control Software)<sup>3</sup>.
- Bus system<sup>4</sup>: parallel communication system between the computer and various electronics such as Direct Digital Synthesizer (DDS).
- Pulse box: FPGA and phase coherent DDSs that receive experiment sequences from the computer and generates accordingly coherent radio frequency pulses for key AOMs.

The computer is connected to the Bus system with a NIDAQ card. DDSs, used to generate

<sup>3</sup>A custom software developed internally in the Blatt group of the University of Innsbruck used for controlling experiments based on trapped ions

<sup>4</sup>Designed in Innsbruck by G. Hendl.

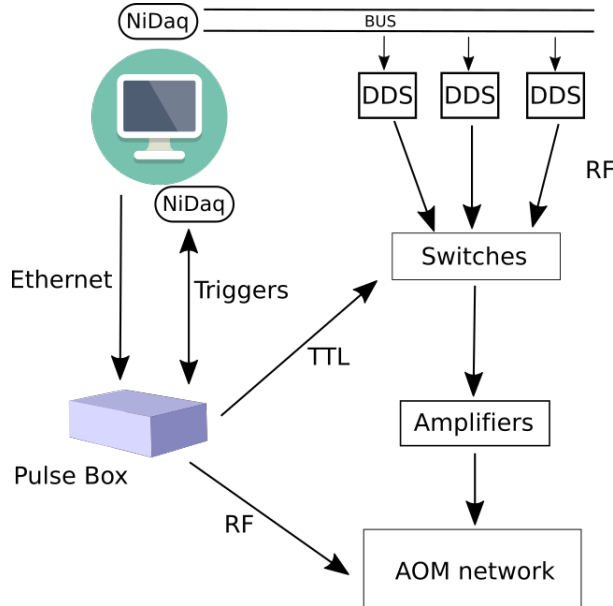


**Figure 3.3.1:** Schematic of the experimental control. Everything is controlled remotely by a PC. During a sequence a pulse box generates coherent radio frequency pulses and digital voltages and sends them to various devices.

radio frequency signal for AOMs, are connected to the Bus system through an optocoupler to avoid ground loops. The computer is connected via Ethernet and with another NIDAQ card to the Pulse Box. The card sends and receives trigger signals, while experiment sequences are uploaded to the Pulse box via the ethernet.

DDSSs are used to generate RF signals that drive the AOMs, they set the frequency and the amplitude of the RF pulses. A set of TTL switches, controlled by the Pulse box, sets the length of the pulses generated by the DDSSs connected to the Bus system. These DDSSs are controlled on the  $\mu\text{s}$  timescale, switches instead are down to few nanoseconds timescale. DDSSs in the pulse box are capable of a stable and controlled phase relationship and of switching the phase on the sub microsecond timescale. In the experiment of Section 5.3.1, Ramsey pulses need to be phase coherent, thus Pulse box DDSSs had to be used. Moreover, during an experiment sequence, the parameters of the DDSSs inside the pulse box can be varied, in contrast to DDSSs on the Bus system whose frequency and amplitude have to be changed outside a sequence.

In a typical experiment, a sequence of pulses is programmed in Python on the computer. When the experiment is run, the computer uploads the sequence to the FPGA inside the Pulse Box. Next, the computer updates the DDSSs on the Bus with the appropriate values for the experiment, sends a trigger signal to the Pulse Box and the Pulse Box generates and sends all the signals for the sequence. When the experiment is done, the Pulse box sends another trigger back to the computer, which proceeds to prepare for the next measurement point, it updates the values of the Bus DDSSs, reuploads the code to the Pulse Box, sends a trigger to start the sequence and the loop is repeated.

# Chapter 4

## Design and simulation of the addressing setup

The purpose of this thesis work was to develop a laser-system for single ion addressing. In this chapter we discuss the design and the implementation of such a system. The design is a crucial part of the work, since there are several requirements that have to be met in order to achieve the desired functionality. In the first section, the requirements are presented together with an overview of the design idea. In the setup an objective was already present, and the choice of an AOD was already made, in anticipation of my project. Hence, we discuss these components as given. The rest of the setup was simulated with the software Zemax, which was used to find the optimal additional optical components and their placement.

### 4.1 Addressing system overview and requirements

Laser systems for single ion addressing have already been developed and employed in experiments successfully in Innsbruck and elsewhere. The main idea is to focus a laser beam tighter than the ion-ion separation and steer it between different ions on a few micro-second timescale. In Innsbruck, calcium ions have been addressed in this way, where the steering was achieved with an AOD [67]. At Duke university, laser beams have also been steered with micro-electromechanical systems (MEMS) mirrors [68]. Another idea is to send a beam illuminating all the ions, but hiding those who are not addressed. This was done with Ytterbium ions by means of an inhomogeneous magnetic field that shifted the transition frequencies of selected ions [69].

Our choice was to implement the approach of Innsbruck [67] with an AOD and improve it. A possible problem of this implementation is limited addressing range as the beam clips on the edge of optics when working with strings of ten ions or more at typical confinement. Furthermore, their system is developed for 729 nm light, while our goal is to use the 393 nm transition; this requires new simulations and different optics. Therefore, the new designed system aims to exploit the full capabilities of the AOD while maintaining a waist of a few microns or less. The shorter 393 nm wavelength offer us the chance for even tighter focuses than have previously been achieved at 729 nm with similar optics. The addressing setup should be able to address single ions in a string in order to generate

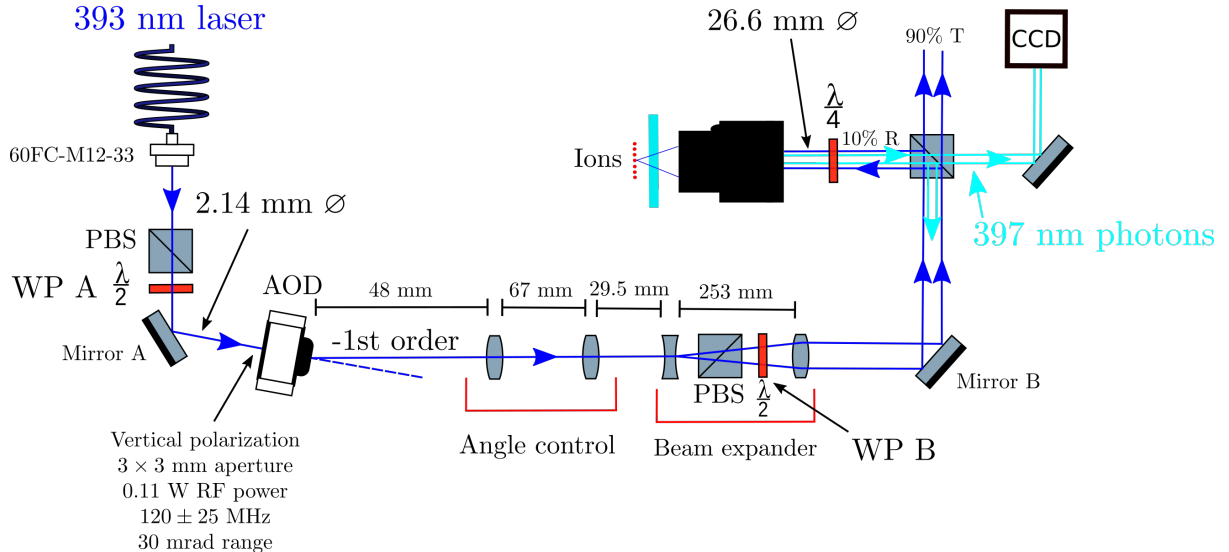


**Figure 4.1.1:** Final schematic of the 393 nm laser single-ion addressed optical setup. Light comes from a fiber, polarization is cleaned, and then sent thorough the AOD from Gooch & Housego 4120-3. -1st order diffracted light is sent into a beam expander, where the beam is broadened before being focused by the objective. All lenses are from Thorlabs, models are from left to right: LA-1509, LA-1131, LC-4252, LA-1725; all of them are AR coated for 393 nm. Critical distances between lenses are in the figure, the distance between the last lens and the first lens of the objective is 722 mm. The 90:10 Beam splitter is custom made by Laser Components GmbH. Diameters  $\varnothing$  are expressed as  $1/e^2$  of the intensity. Between objective and ions is a 6 mm thick glass of the viewport, as the objective is out of vacuum.  $\lambda/2$  waveplates are labeled as WP A, and WP B for future reference. Light blue lines represent 397 nm scattered photons coming from the ions into the imaging setup.

single photons out of single ions via the already discussed Raman process. Ion separations have been derived in Section 2.3.2. In the case of two  $^{40}\text{Ca}^+$ , the separation between the two ions is  $5.6 \mu\text{m}$  for an axial center-of-mass frequency of 1 MHz. The setup must therefore be able to focus a laser beam down to  $1\text{-}2 \mu\text{m}$  waist to minimize cross talk. As seen in Section 2.4.1, a tighter focus can be obtained with a shorter wavelength, a bigger lens, or with a shorter focal length. The focusing lens, i.e. the objective, is shared with the imaging setup, and thus it is given, the focal length (66.8 mm) is therefore a constant in the problem, see Section 4.2. The wavelength is also a constant, as the Raman process happens at 393 nm. This gives only one possibility left to tighten the focus, i.e. by making the beam as wide as possible at the objective input surface.

Figure 4.1.1 presents the final layout of the addressing setup. Some key aspects are now discussed. Beam expansion is achieved with a Galilean telescope composed of two lenses: a concave lens for diverging a collimated beam and a convex lens for collimating the diverging beam. The combination of these two lenses takes a collimated beam and expands it to another approximately collimated beam with an expansion factor of 23.9<sup>1</sup>. This expansion part is one of the two essential parts of the addressing setup. The other part is related to the addressing spatial range. We want not only to focus the beam to

<sup>1</sup>Since the beam is only approximately collimated after the beam expander, the expansion factor has been calculated as the ratio of the incoming and outgoing beam diameters of the beam expander.

a single ion, but also to move the beam as well, such that it focuses on a different ion. Therefore, there is a requirement also on the range (along the ion string axis) that can be addressed. This depends on the number of ions and their spacing. We chose to aim to address tens of ions, this requires the ability to move the focus along the ion string by 150-200  $\mu\text{m}$ . Beam steering is possible with the use of an AOD, the detailed working principle of this device has been discussed in Section 2.4.2. Basically, the angle of the output beam of the AOD changes as the driving frequency changes. However, the AOD must be placed far behind the objective to leave space for the beam expander, needing to redirect the angular change of the AOD's output. This task is accomplished with a pair of converging lenses (Angle control in Figure 4.1.1), which refocus the collimated beam into the beam expander, the beam then becomes wider, reaches the objective and is focused on the ion. The objective was not designed to focus incoming collimated blue light onto the ions, but rather to image 397 nm photons from the ions onto a camera 1.5 m away from the objective. Simulations showed that a slightly diverging 393 nm beam ( $\sim 0.5^\circ$ ), incoming into the objective, will be focused onto the ions. As such, we set the telescope to expand the beam without collimating it, leaving it diverging, so that the objective can focus it at the right position.

The setup displayed in Figure 4.1.1 contains polarization optics. As discussed in Section 2.2.3, Zeeman transitions are polarization sensitive, thus polarization control is required. In order to control the polarization at the point of the ion a half-waveplate and a quarter-waveplate are inserted in the optical path. The position of the quarter-waveplate, right before the objective, means that it is unusually big (2 inches in diameter), but if placed before in the optical path, the mirror and the beam splitter could alter the polarization. The quarter wave plate is zeroth order and custom made by CeNing Optics, in order to have a greater polarization stability.

The choice of a 90:10 beam splitter (Figure 4.1.1) to overlap the incoming 393 nm addressing laser with the outgoing 397 nm ion fluorescence for imaging is unusual: a more obvious choice would be to use a dichroic mirror. However, the light in the imaging path is 397 nm, very close to the 393 nm light of the addressing setup. This would have meant using a very narrowband dichroic element. Instead, we use a 90:10 beam splitter, where 90% of the light is transmitted and only 10% of the light is reflected. In this way, only 10% of imaging light is lost, at cost of 90% of addressing laser light, which is not such a problem as power from the laser is available. Furthermore, this light is focused so tightly that even a small amount of light can excite the ions. On the other end, it is not so straightforward to get more scattered light from the ions, so 397 nm light and the imaging setup must be as efficient as possible, with 10% losses, ions states are still distinguishable on the camera without significantly extending the detection times required.

## 4.2 Objective and AOD

The objective used to focus the light is a custom objective by Sill optics, Figure 4.2.1 presents the model and a Zeemax simulation made by Sill Optics. This objective has different purposes: collecting 397 nm photons from ions, and imaging them onto a spot 1.5 meters away from the chamber; single-ion focusing with 729 nm light, taking incoming collimated 729 nm light and focusing onto an ion. The numerical aperture is  $\text{NA} = 0.289$ , thus the effective focal length  $f = 66.8 \text{ mm}$ . Furthermore, the objective was designed to take into consideration that the light after the objective has to go through a 6 mm

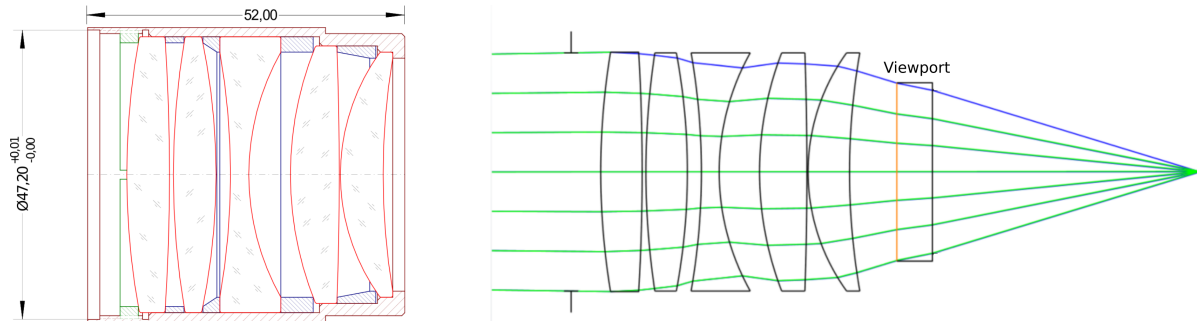


**Figure 4.2.1:** On the left, a cross section of the custom objective made by Sill Optics, in red the 5 lenses are depicted, while the rest is the mechanical housing, given dimensions are in mm. On the right, Zemax simulation for 397 nm light: 5 lenses for the objective, a 6 mm viewport, and, after 38.6 mm of vacuum, the ions.

fused silica viewport and a further 38.6 mm of vacuum before reaching the ions. The objective is mounted on a 3 dimensional manual translational stage to allow for imaging and addressing calibration.

The AOD is from Gooch & Housego, model 4120-3, the datasheet is available in Appendix A. The crystal is Tellurium dioxide ( $\text{TeO}_2$ ). The company specifies a central frequency of 120 MHz, with 50 MHz bandwidth, so the driving frequency ranges from 95 to 145 MHz with a maximum RF power of 0.3 W. The specified addressing spatial range is 30 mrad, i.e. angle of deflection  $\pm 0.86^\circ$ . In this bandwidth the diffraction efficiency should remain above 75 % and have an average of 83 %, further 3% of light is lost due to insertion losses. The active aperture measures  $3 \times 3$  mm, and the polarization has to be horizontal when entering the AOD, while the specified output polarization is vertical.

## 4.3 Design simulation

The simulation of the setup in Figure 4.1.1 was done with the software Zemax<sup>2</sup>. The simulation had the purpose of assessing the performance of the setup and to find suitable lenses and their optimal locations. The simulation included: the four lenses, the objective, and the viewport. As there is no option to simulate an AOD, it was not taken into consideration, instead the simulation started at the output of the AOD as described below. Mirrors and beam splitters were not included in the simulation as their contributions should be negligible. The simulation starts by specifying the input fields, representing the physical light beam at the output facet of the AOD. To account for the ability to change the output angle from the AOD, three different fields have been simulated. One is along the optical axis, while the other two are simulated starting with an angle of  $\pm 0.86^\circ$  with respect to the optical axis. The propagation of these fields represents three different AOD deflection angles, one corresponds to the deflection angle when the AOD is operating at the center of the bandwidth, and the other two when the AOD is operating at the extrema of the bandwidth. Next, the four lenses of the setup were inserted in Zemax, initially with variable radii, thicknesses and separations. Initial positions and lens focal lengths were set according to geometrical boundaries given by physical constraints on the optical table where the setup had to be built. In fact, the setup has to be built inside the

<sup>2</sup>Zemax OpticStudio is a commercial software based on ray tracing used for designing optical systems.

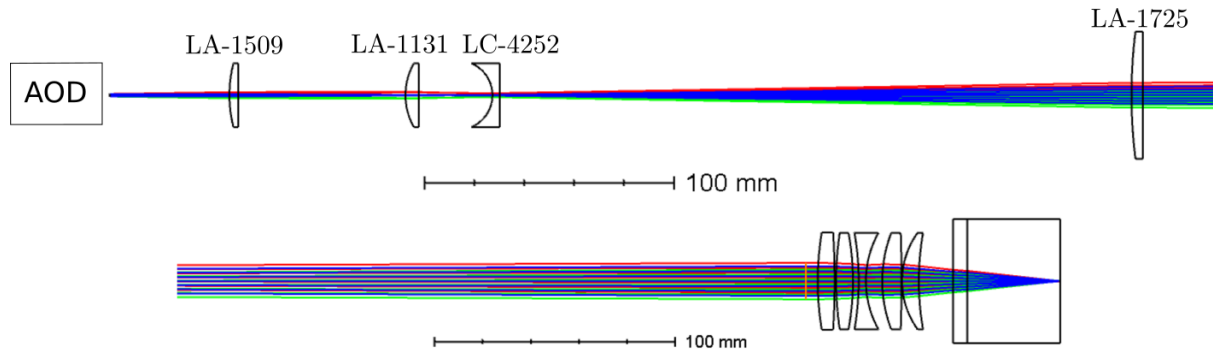


**Figure 4.3.1:** Zemax simulation of the setup. Rays propagate from left to right starting from top left. The simulation layout has been separated in two for displaying purposes. In the top part, the four lenses are depicted, the rays continue in the bottom part where the objective and image plane are located. Different colors indicate different beams emerging from the AOD at different angles, rays with the same color belong to the same beam. The blue one is the central beam emerging from the AOD with a  $0^\circ$  angle, the red and the green beams emerge respectively with  $\pm 0.86^\circ$ .

mu-metal chamber surrounding the ion-trap experiment. The Zemax file of the objective was provided by the company which designed it<sup>3</sup> and was simply imported in the project. After the objective the 6 mm viewport glass was included and then vacuum for 38.6 mm, which is the expected distance between the outer facet of the glass and the ion axis. The image plane was therefore set 38.6 mm after the viewport. In the experiment, the distance between the objective and the viewport could not be measured (the objective is mounted inside an inverted viewport and there is no access space for distance measurement at the mm level). However, this distance was inferred from a Zemax simulation of the imaging path, for which we assumed that the ions are focused on the camera 1.5 m away. We determined a space between the viewport and the objective of 14 mm.

The simulation was carried out with the Zemax tool Physical Optics Propagation (POP). POP works by propagating a wavefront represented by an array of discrete points<sup>4</sup>. The array is propagated through every optical component and free space. This method can be used to simulate Gaussian beams as well as wave phenomena such as diffraction and aberrations. The initial value given to the propagator was the waist of the collimated beam out of the AOD. Since the beam going to the AOD comes from a fiber collimator, the value specified was taken from the datasheet of the fiber collimator, namely Schäfter + Kirchhoff 60FC-M12-33 [70], as 1.07 mm. The first step of the simulation work was to find the appropriate lenses to build the setup. The thicknesses and the radii of curvature were optimized trying to achieve the smallest focus spot while maintaining the desired addressing range. The lenses were found with the Zemax tool *Stock Lens Matching*. Basically, the tool compares the simulated lenses with those in a catalogue from different companies and finds the closest match. We opted to rely on the provider Thorlabs, so the search was limited to this company. Found lenses were in order from left to right LA-1509,

<sup>3</sup>There are currently 2 versions of the files. Both contain the same objective but with slightly different composite lenses. Effectively, the difference in the simulation is the focal length: 54 mm and 52 mm. However, by adjusting the distance between the objective and the viewport (which is unknown at the mm level in the experiment), this difference is compensated and their performance is identical. In the simulation the 54 mm version is used.

<sup>4</sup>grid of  $30.6 \times 30.6$  mm, sampled with  $256 \times 256$  points.

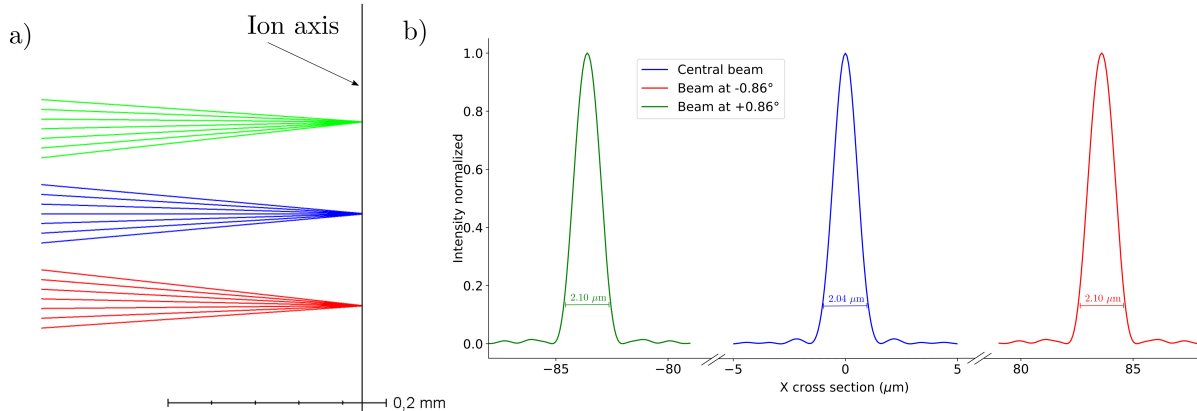


**Figure 4.3.2:** Zemax simulation at the image plane, where the ions are. a) Addressing range from Zemax simulation, the three beams emerge from the AOD at different angles. The full addressing range here displayed is 168 μm. b) Physical Optics Propagation of the three Gaussian beams with angles of 0, ±0.86°, and waist at AOD of 1.07 mm. Displayed is the  $x$  cross section at the ion axis. Beam diameters (13.5%) are also displayed, the central beam at 2.04 μm is slightly narrower with respect to the outer ones 2.10 μm.

LA-1131, LC-4252, and LA-1725 and can be seen in Figure 4.3.1. Once the desired lenses were found, their Zemax files provided by the company were imported in the project.

The second step was to optimize the lenses position's always trying to keep the focus spot as small as possible, and the desired addressing rage of 150-200 μm. This was done using the optimizing tools of Zemax and the merit function. The software can perform multivariate analysis and minimize the focus spot depending on all the assigned variables, which in this case were the distances between the lenses. The final results, for the lens setup shown in figure 4.1.1, is presented in Figure 4.3.2, the addressing range is 168 μm limited by the bandwidth of the AOD from the specification sheet. The waist of the central beam is 1.02 μm, and beam profiles at the border of the addressing range are 3% wider, with a waist of 1.05 μm.

Another important parameter for the performance of the setup is the addressing error. Qualitatively speaking, in the case of the beam focused on one ion, the addressing error is caused by the light interacting with the neighbouring ions. It can be a particular problem in the case of aberrations that produce bumps on the side of the main Gaussian peak. In the case of a diffraction limited system, the profile of the beam is a sinc function that has more local maxima around the central peak. To estimate the addressing error in a simulation, we consider two ions 5.6 microns apart, centered on the optical axis of the addressing system, the respective addressing beams have been simulated. In Figure 4.3.3 the intensity profile and the electric field of the addressing beams are plotted. The addressing error is different for different physical process, in the case of AC Stark shifts, as the experiment discussed in 2.5.1, the shift is proportional to the intensity, so the addressing error is calculated as  $I_1(x_2)/I_1(x_1) \simeq 10^{-4}$ , where  $I_1$  is the intensity profile of the beam focused on ion 1, and  $x_1, x_2$  are respectively the position of ion 1 and ion 2. In the case of the cavity mediated Raman process, as in the experiment discussed in Section 2.5.2, the strength of the process is proportional to the Rabi frequency, i.e. the electric field. Therefore, the addressing error is given as  $\sqrt{I_1(x_2)/I_1(x_1)} \simeq 10^{-2}$ .

Another aspect that was simulated is the beam profile inside our ion trap system. Optical access to the trap is limited and a tightly focused beam also has correspondingly

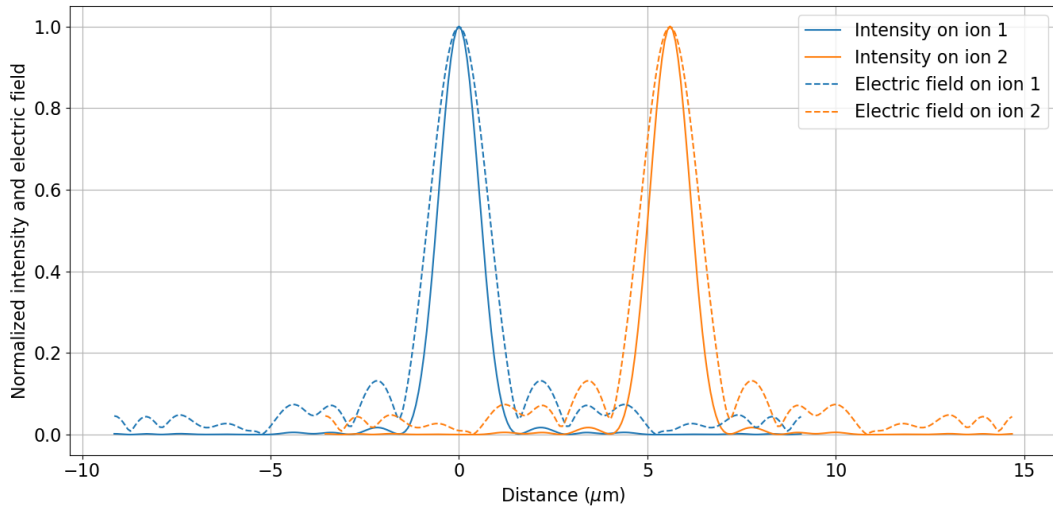


**Figure 4.3.3:** Zemax simulating of the beam focused in two different places separated by  $5.6 \mu\text{m}$  corresponding to the theoretical equilibrium positions of two ions with axial center of mass frequency of 1 MHz. Addressing error for AC Stark shift is calculated as the ratio of intensities at ion positions:  $I_1(x_2)/I_1(x_1) \simeq 10^{-4}$ . For Raman transition, the ratio of electric fields is taken:  $\sqrt{I_1(x_2)/I_1(x_1)} \simeq 10^{-2}$ .

a large divergence, which could lead to clipping on the trap's blades or compensation electrodes, scattering light all around the trap. In Figure 4.3.4 the top view of the trap is plotted, here we included the three pairs of compensation electrodes, the RF blades, and the cavity mirrors. The blue line represents the radius  $W(z)$  from Equation 2.4.4 of the addressing beam in the case of a waist  $W_0$  of  $1 \mu\text{m}$ . To determine the fraction of power lost due to clipping on the compensation electrodes, we can calculate the transmitted power through the top electrodes:

$$P_t = \int_{-\infty}^{\infty} dy \int_{-x_c/2}^{x_c/2} dx P(x, y, z), \quad (4.3.1)$$

where  $P(z)$  is the power of the Gaussian beam, and  $x_c$  is the horizontal position of the compensation electrode. The integral can be computed numerically at position  $z$  of the electrodes. The result is plotted in Figure 4.3.4, where the lost power  $1 - P_t$  is plotted as a function of the waist  $W_0$ . At the expected waist of  $1.02 \mu\text{m}$ , the power lost is less than 1%, i.e. for  $2 \mu\text{W}$  AOD input power, after considering all the losses in the setup, it means losing less than a nW. The previous calculation holds only if the beam is perpendicular to the  $x$  direction so it is important to align it carefully.

To conclude this section, we discuss some aspects of the design. Waist and addressing range were the two key aspects. In the last stage of the simulation, the distances between the lenses were optimized, and their position is a compromise between small waist and large addressing range, it is possible therefore to sacrifice one to improve the other. We found that the addressing range can be broadened by moving the beam expander closer to the objective, simulations yielded an addressing range of  $180 \mu\text{m}$  for a distance between objective and lens LA-1725 of 622 mm, in this case the distance between this lens and lens LC-4252 is 262 mm to keep the focus at the same position. In this configuration a greater addressing range is achieved, but the waist at the ions is  $1.10 \mu\text{m}$ , broader than the  $1.02 \mu\text{m}$

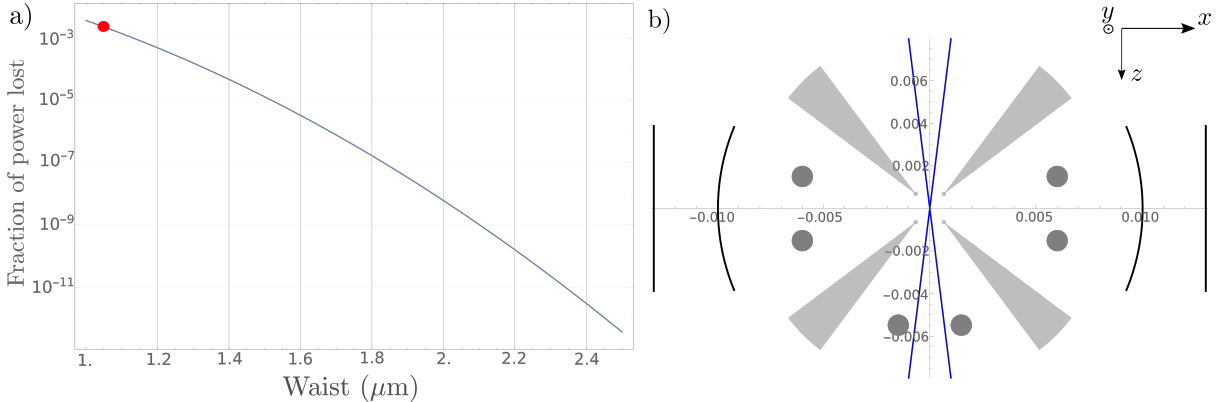


**Figure 4.3.4:** a) Fraction of power lost due to clipping on the compensation electrodes as a function of the beam waist when focused on the ion. The red point represents the waist  $1.02\ \mu\text{m}$ , obtained from the simulation. b) Top view of the trap and addressing beam. Grey circles are the compensation electrodes, blue is the radius  $1/e^2$  of the beam focused on the ions with waist of  $1.02\ \mu\text{m}$ , while the black arches represent the mirrors of the cavity. All units are in meters.

presented in this section. In the simulation, an attempt to decrease the addressing range and obtain a smaller waist by moving the beam expander farther away from the objective fails; the addressing range is reduced, but the waist does not significantly diminish as the full diameter of the objective is being used. Moreover, aberrations, already noticeable in Figure 4.3.3, get worse, the small bumps on the side of the main peak increase in height. This could suggest that the system is diffraction limited at the entrance of the objective, the bumps are in fact attributable to an Airy pattern commonly associated with diffraction limited system [71].

## 4.4 Physical implementation

Once the simulation gave satisfactory results, a test setup was built. The idea of building first a test setup on a different optical table from the main experiment was to check if the system was working as intended, and to assess its performance. Due to physical access problems in the final system there is no space to place a beam profiler, or a polarimeter, and after the objective there is no access to the vacuum and the trap. While on another table everything could be checked and tested. The results of the measurements obtained on this test setup are presented in Chapter 5.

Afterwards, the system was moved and implemented on the optical table containing the ion trap. For the initial alignment, a counter propagating 729 nm red beam was sent in the opposite direction: starting from the front of the chamber, through the ions, and through to the objective and back through the addressing path. Since the lenses of the addressing are antireflection coated for 393 nm, the reflection of the red beam was visible and it was possible to align the components such that the beam passed approximately through the center and perpendicular to the surfaces. Calibration was also done with ions and the beam position was indirectly observed on the camera via the excited fluorescence of the ions. A string of ions was used as a probe by constantly imaging the ions with 397 nm (illuminating the entire string equally) and 393 nm (illuminating ideally a single ion) light on the camera. The 393 nm laser drives the transition  $S_{1/2} \leftrightarrow P_{3/2}$ . From  $P_{3/2}$  the

electron has two other decay channels,  $D_{3/2}$ , and  $D_{5/2}$ , which means that the electron will eventually end up in one of these two states. Repumping with 854 nm and 866 nm light the transitions  $D_{5/2} \rightarrow P_{3/2}$ , and  $D_{3/2} \rightarrow P_{1/2}$  avoids this problem and brings the electron back to the fluorescence cycle. To observe where the addressed 393 nm beam is, we send pulses of 854 nm light such that when the 854 nm light is off the ions addressed by the 393 nm laser become dark after decaying from  $P_{3/2} \rightarrow D_{5/2}$ . The ions become bright again when a new pulse of 854 nm light is sent, therefore if the pulse rate is slow enough it is possible to see the addressed ions as blinking on the CCD camera. This process was used for initial alignment of the addressing beam focus and direction on the ion string. Once done, the next stage is to directly measure and optimize the AC stark shifts, as presented later in section 5.3.1.

A photo of the installed system is shown in Figure 4.4.1. Here, the collimating lens is mounted on a 3D manual screw-gauge translation stage for fine tuning calibration position of the focus w.r.t. the ion string. Manual screws were later replaced with remote controlled ones from Newport, model PZA12 so that beam alignment is possible without opening the mu-metal enclosure. The AOD is placed on a rotation mount that allows us to tilt it in two directions. One direction was used to find the Bragg angle of the AOD to achieve maximum diffraction efficiency, the other can be used to tilt the axis over which the AOD sweeps to compensate for an ion string which is not exactly parallel to the AOD sweeping direction.



**Figure 4.4.1:** Photo of the setup for the addressing unit. The blue dashed line is the beam path starting from bottom left at the fiber collimator, all the way to the top where a mirror deflects the beam and send it to the 90:10 beam splitter (Figure 4.1.1). The following elements are visible: (A) Fiber collimator 60FC-M12-33 (B) Polarizing beam splitter (C)  $\lambda/2$  (D) AOD (E) Lens LA-1059 (F) Iris to block 0th order (G) Lens LA-1131 (H) Diverging lens LA-4252 (I) Iris (L) Lens LA-1725 on the 3D manual screw-gauge translation stage (M) Mirror.

# Chapter 5

## Experimental results

This chapter summarizes the key experimental results obtained during this master's work:

- Section 5.1 contains the characterization of the AOD.
- In Section 5.2 the characterization of the test setup is presented. Polarization, stability, and focus spot have been checked. In particular, two methods have been used to measure a  $\mu\text{m}$  focus spot: razor blade scans, and a small pixel size camera.
- In Section 5.3 the results from experiments with trapped ions are presented. First, single-qubit manipulation via Ramsey interferometry, which also allowed for a check of the addressing performance. Second, a cQED experiment where single photons were generated from a single ion in a string, via a cavity-mediated Raman process (Section 2.2.3).

### 5.1 AOD

The two main parameters we are interested in here are the diffraction efficiency and the response time. For the diffraction efficiency we measured the total output power of the light  $P_{tot}$  and then the power of the first diffracted order  $P_1$ . Diffraction efficiency is defined as the ratio between the two

$$\text{DE} = \frac{P_1}{P_{tot}}. \quad (5.1.1)$$

The response time is the time it takes for the light to move to a new position corresponding to an RF frequency change. The measurement of the response time gives us an idea of how long it takes to switch from one ion to the other.

Before measuring the diffraction, the optimal RF power to drive the AOD has been found by maximizing the power of the first diffracted order with the AOD set at its central frequency. Power measurements of the light were made with a Thorlabs PM100D, and the AOD was driven with an amplifier and an RF signal generator. The highest efficiency at the central frequency was found for an RF power of 0.11 W, and for the rest of the measurements it was kept at that value. Furthermore, to optimize the linear input polarization, a PBS followed by a half-waveplate were placed before the AOD, and the waveplate was rotated to maximize the power of the diffracted light. In Figure 5.1.1 a plot of the measured diffraction efficiency as a function of the RF frequency is displayed. Within a bandwidth of 50 MHz from 105 MHz to 155 MHz, we can see that more than 70 % of the light is in the first diffracted order as expected from the datasheet (Appendix A)

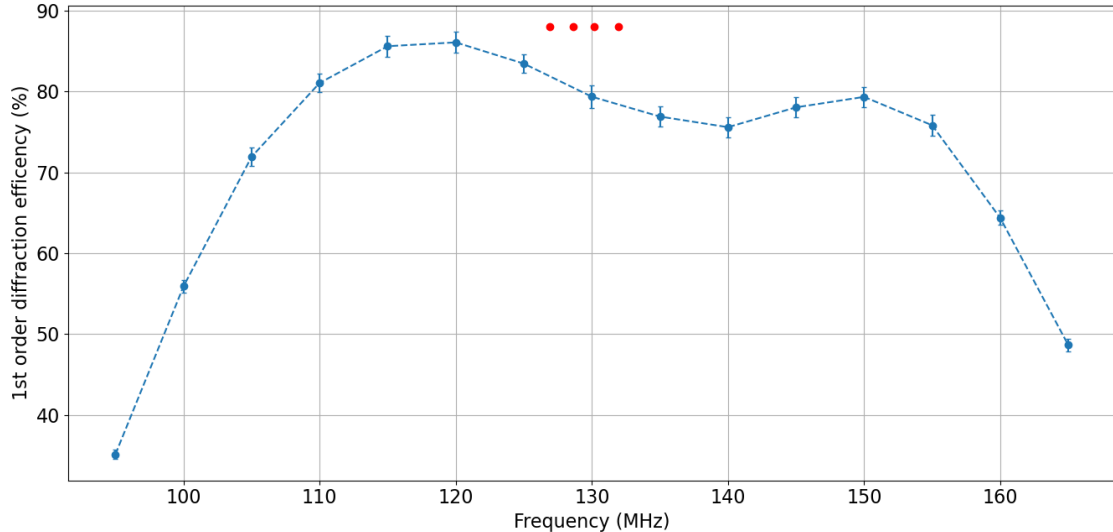


**Figure 5.1.1:** Measurement of the diffraction efficiency of the AOD as a function of the RF driving frequency (Equation (5.1.1)). Blu dots indicate the measured points. Red points indicate the expected frequencies associated with addressing 4 ions for an axial COM frequency of 780 kHz (the conditions for the experiment are presented in Section 5.3.1), the theoretical separations are 5.15  $\mu\text{m}$  for the two outer ions, and 4.77  $\mu\text{m}$  for the inner ions.

In order to measure the response time, a voltage controlled oscillator (VCO)<sup>1</sup> was used to generate the RF signal. The VCO was supplied a square wave that alternated between two voltages corresponding to two different frequencies  $\sim 96$  and  $\sim 127$  MHz. The laser light diffracted into the -1 order was measured with a photodiode. The photodiode was aligned with the light at one particular frequency, such that when the light moves, the beam would not hit the diode and the signal generated changes. In Figure 5.1.2, the signal of the photodiode, together with the supplied VCO signal are plotted. The response time is  $\sim 8 \mu\text{s}$ , with  $3 \mu\text{s}$  delay and  $5 \mu\text{s}$  rise time. From the beam diameter (2.14 mm,  $1/e^2$  of intensity) and the acoustic velocity in the crystal (0.65 mm/ $\mu\text{s}$ , Appendix A) we expect  $4.9 \mu\text{s}$  rise time, while the delay indicates that the distance between the piezo and the edge of the beam is 1.95 mm.

## 5.2 Full test setup characterization

The test setup was built on an optical table with a spare objective since the one installed in the vacuum chamber was already in use for ion imaging. The layout of the system in Figure 4.1.1 was replicated.

<sup>1</sup>Minicircuit ZOS-150+, response time 130 ns.

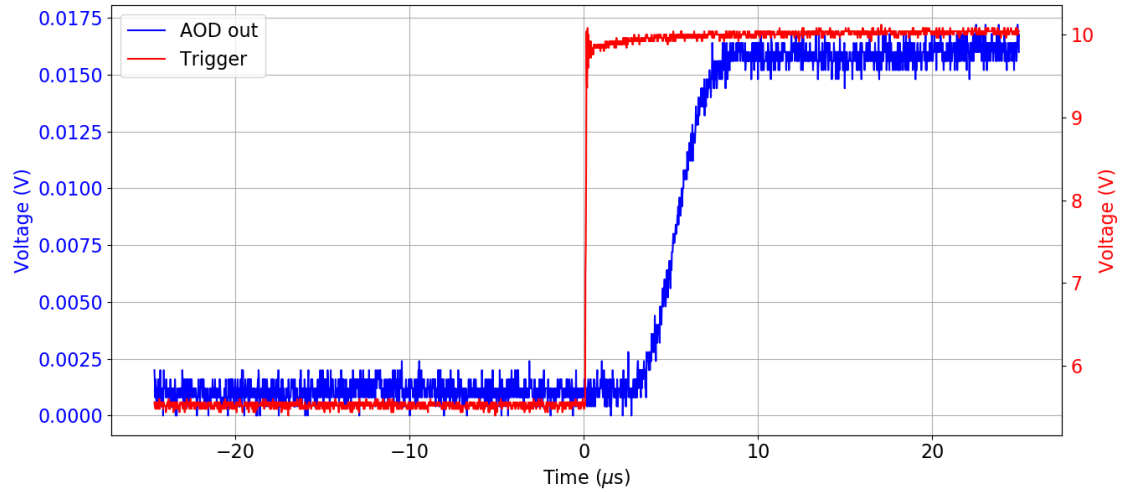


**Figure 5.1.2:** Measured response time of the AOD, plotted are the photodiode signal in blue on the left  $y$  axis, and the VCO voltage is in red on the right axis. The voltage of the VCO determines the frequency of the RF sent to the AOD. The change here corresponds to a frequency shift of  $\sim 31$  MHz between  $\sim 96$  and  $\sim 127$  MHz. At the highest voltage, the photodiode measures the -1st order diffracted light.

### 5.2.1 Waist: Knife-Edge method

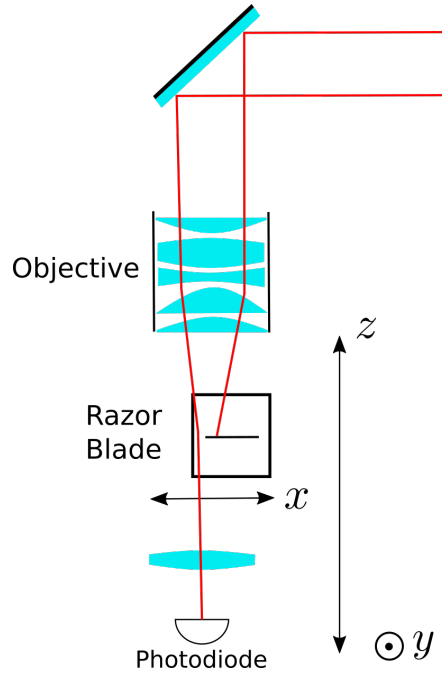


**Figure 5.2.1:** Scheme of the razor scan. A translation stage allows for moving the blade in the direction  $x$ , perpendicular to the beam, and  $z$ , along the beam.

Measuring a micrometer scale waist is not an easy task, the first method applied consisted of mounting a razor blade on a translational stage. The setup used is shown in Figure 5.2.1, after the objective the blade is present, and since the beam is quickly diverging after the focus, a lens is used to refocus the light into a photodiode. The stage is moved

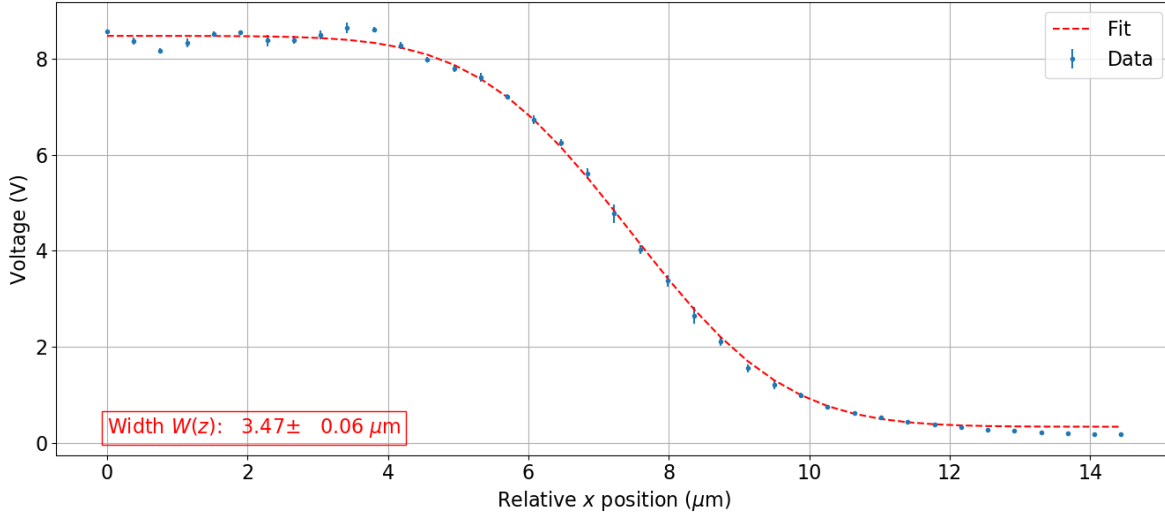


**Figure 5.2.2:** Razor blade scan with the lowest width obtained. Blue dots are the data points, while the red curve is a fit of equation (5.2.1).

in the  $x$  direction cutting the beam perpendicularly such that the blade is scanning the beam profile. A filter was inserted in order to avoid saturation of the photodiode. In the  $z$  direction the stage was controlled with a manual screw with resolution of  $1\text{ }\mu\text{m}$ . While in the  $x$  direction, the stage had to be moved with sub-micrometer precision, so instead there was a piezo actuator controlled with a computer. The same computer also controlled a multimeter that measured the voltage of the photodiode. To get the profile  $W(z)$  (Equation (2.4.4)) of the beam, the measurement procedure was as follows

- Position blade at desired  $z$  coordinate
- Scan beam in  $x$  direction with blade
- Shift  $z$  direction

The procedure is repeated for different values of  $z$ . The beam width can be calculated from the scans by fitting the data with the following equation [72]

$$P(x, z) = \frac{P_0}{2} \operatorname{erfc} \left[ \frac{\sqrt{2}(x - x_0)}{W(z)} \right]. \quad (5.2.1)$$

Where the fitting parameters are  $P_0$ ,  $x_0$ , and the width  $W(z)$ .

In Figure 5.2.2 we report an example of a scan that gave a minimal waist. The errorbars come from statistical average, every data point is a mean over 5 measurements, and the error is the standard deviation. The fit in this case gave a width  $W$  (beam width  $1/e^2$ ) of  $3.47 \pm 0.06\text{ }\mu\text{m}$ , the smallest width obtained with this method, but significantly broader than the  $1\text{ }\mu\text{m}$  simulated waist. Furthermore, the profile  $W(z)$  was not symmetric and could not be fitted with Equation (2.4.4). A possible explanation is that with this commercially-available razor blade, the accuracy is limited by the positioner and the blade roughness. The latter was not known at the few micrometer scale of the beam waist. In comparison, authors of [73] have used, instead of a common razor blade, a glass substrate etched with an effective knife-edge features with which they were able to measure a  $1\text{ }\mu\text{m}$  waist.

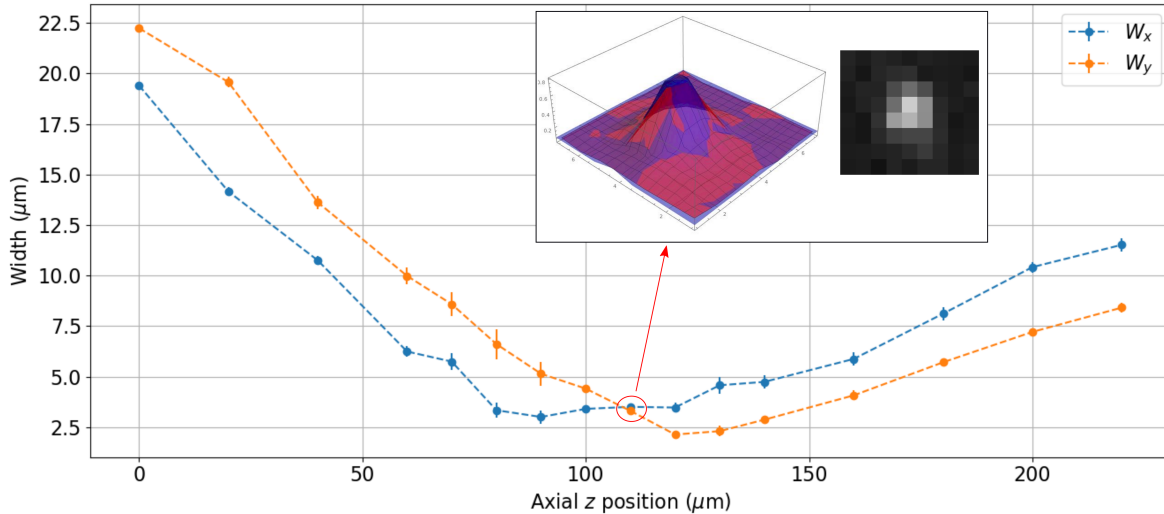


**Figure 5.2.3:** Profile of the Gaussian beam along  $z$  measured with the IDS camera. Errorbars are estimated from fit. In the inset an example of raw data and Gaussian fit. In red color, the normalized pixel value is displayed, while the blue curve is a fitted 2D Gaussian. On the axis there is the pixel number.

### 5.2.2 Waist: Camera

Since the Knife-Edge method did not prove that we had achieved our desired waist, a more direct approach has been subsequently adopted. We measured directly the beam with a camera from IDS model UI-1490LE-M-GL. This camera has a pixel size of  $1.67 \mu\text{m}$  with no spacing between pixels. It should therefore be suitable to measure a focus spot with a  $\mu\text{m}$  precision. A  $1 \mu\text{m}$  focus should hit one single pixel, and if aligned between two pixels, a Gaussian profile could also be fitted. In addition, unlike the Knife-Edge technique, a camera provides 2-dimensional information about the beam shape and can be exploited to look for aberrations in the system. The setup is almost the same as Figure 5.2.1, but the camera now replaces the razor blade, and there is no need for scanning in the  $x$  direction, as the  $z$  is enough to reconstruct the profile  $W(z)$ . An additional filter was used to optimize the light reaching the camera in order to not saturate it. For every desired  $z$  displacement, a photo with the camera is taken, post processed, and then the camera is displaced to the new  $z$  coordinate. Post processing is done by fitting the pixel values with a 2-dimensional Gaussian

$$P = A \exp \left\{ -\frac{(x - x_0)^2}{2\sigma_x^2} \right\} \exp \left\{ -\frac{(y - y_0)^2}{2\sigma_y^2} \right\}. \quad (5.2.2)$$

The fit parameters are  $A$ ,  $x_0$ ,  $y_0$ ,  $\sigma_x$ , and  $\sigma_y$ . From the standard deviations  $\sigma_x$  and  $\sigma_y$  the beam width in the  $x$  and  $y$  direction at position  $z$ :  $W_x(z)$ ,  $W_y(z)$  can be determined as  $W_x(z) = 2 \cdot 1.67 \cdot \sigma_x$  and respectively  $W_y(z) = 2 \cdot 1.67 \cdot \sigma_y$ , where  $1.67 \mu\text{m}$  is the pixel size (see caption of Figure 2.4.1). The full profiles  $W_x(z)$  and  $W_y(z)$  can be found in Figure 5.2.3. Here anomalies can be noticed. The profile is asymmetric and does not follow Equation 2.4.4, nonetheless a width  $< 2.5 \mu\text{m}$  has been measured. We decided to install the system and measure more accurately the waist with a single ion.

Desired polarization	$\lambda/2$ WP B ( $^{\circ}$ )	$\lambda/4$ ( $^{\circ}$ )	Stokes 1	Stokes 2	Stokes 3
Horizontal	$267.2 \pm 0.1$	$49.7 \pm 0.1$	1.00	-0.01	0.01
Vertical	$312.5 \pm 0.1$	$48.1 \pm 0.1$	0.96	0.12	-0.26
Right circular	$267.2 \pm 0.1$	$4 \pm 0.1$	0.05	-0.02	1.00
Right circular	$312.5 \pm 0.1$	$93.1 \pm 0.1$	0.10	0.01	1.00
Left circular	$267.2 \pm 0.1$	$95.4 \pm 0.1$	0.06	0.01	-1.00
Left circular	$312.5 \pm 0.1$	$3.1 \pm 0.1$	-0.20	0.06	-0.98

**Table 5.2.1:** Desired polarization at the ion position and angles of the waveplates  $\lambda/2$  WP B and  $\lambda/4$  (Ref. Figure 4.1.1) that set the polarization. Numbers are found as maxima or minima of a sine fit of the polarization data in appendix B. Measured Stokes parameters of the achieved polarization are given.

### 5.2.3 Polarization

As discussed in the design Section 4.1 and in the Raman process 2.2.3, polarization is an important component as atomic transitions are polarization sensitive, thus the polarization capabilities of the system had to be tested. The goal is to allow for the generation of vertical, horizontal, left circular, and right circular polarization at the ion position and test how well they are achieved. Polarization can be changed with two plates: a half wave plate after the AOD, and a quarter wave plate right before the objective, see Figure 4.1.1. In order to characterize the polarization at various points in the optical path of the addressing setup, the three Stokes parameters  $S_i$  [74] were measured with a polarimeter from Schäfter + Kirchhoff series SK010PA.

Stokes parameters quantify the type of polarization of an electric field. Linear polarized light has Stokes parameters  $S_2, S_3 = 0$ , while  $S_1 = \pm 1$  for horizontal and vertical polarization respectively. Circular polarized light has  $S_1, S_2 = 0$  and  $S_3 = \pm 1$  for right hand and left hand circular polarization respectively.

The first step was to characterize the polarization after the waveplate after the AOD ( $\lambda/2$ , WP B, Figure 4.1.1), the main result from this characterization is that horizontal polarization can be achieved immediately after WP B when the angle of WP B is set to  $267.2 \pm 0.1^{\circ}$ , and vertical is achieved with an angle of  $312.5 \pm 0.1^{\circ}$  obtained from fitting a sine on the first Stokes parameter. From the same fit, the semiperiod of the polarization is  $45.3 \pm 0.6^{\circ}$  consistent with the  $45^{\circ}$  expected for a half waveplate.

Afterwards, we measured the polarization after the objective at the focus spot where the ions ideally sit. For this measurement we set the  $\lambda/2$  WP B first at  $267.2 \pm 0.1^{\circ}$ , and then at  $312.5 \pm 0.1^{\circ}$ , for both numbers we measured the three Stokes parameters as a function of the  $\lambda/4$  angle. Results are summarized in table 5.2.1, in appendix B the full plots are reported.

### 5.2.4 Stability

It is imperative to know the stability of the system in terms of polarization and beam pointing to determine over which timescale the setup needs to be re-optimized or calibrated.

First we measured polarization, it was set to be right circular at the ion position:  $\lambda/2$  set to  $267^{\circ}$ , and  $\lambda/4$  set to  $4^{\circ}$ . We recorded the three Stokes parameters for a total of one

hour, this data is plotted in Figure 5.2.4. It can be seen that the polarization was stable.

Beam pointing stability is the movement of the focus position, which could drift in any direction. To test it, we recorded the position of the focus for a period of one hour with the camera. The camera was positioned at the focus with the same setup as discussed in Section 5.2.2, and then a video was recorded. The video was later analyzed by tracking the brightest pixel over time. In Figure 5.2.5 we can see the horizontal ( $x$ ) and vertical ( $y$ ) position of such pixel drawn as a function of time. In the horizontal direction, fluctuations of one single pixel can be noticed, which could be a result of the light hitting between two pixels. In the vertical direction the fluctuations are in the order of two pixels, this could indicate that the position might have shifted by one entire pixel over this period. This means that the focus position was stable in the test setup within an upper bound of  $1.6 \mu\text{m}/\text{hr}$ . We have to consider that this measurement was taken on a open table, a more precise beam pointing stability measurement is carried out with ions in the closed mu-metal shield, see Section 5.3.1.

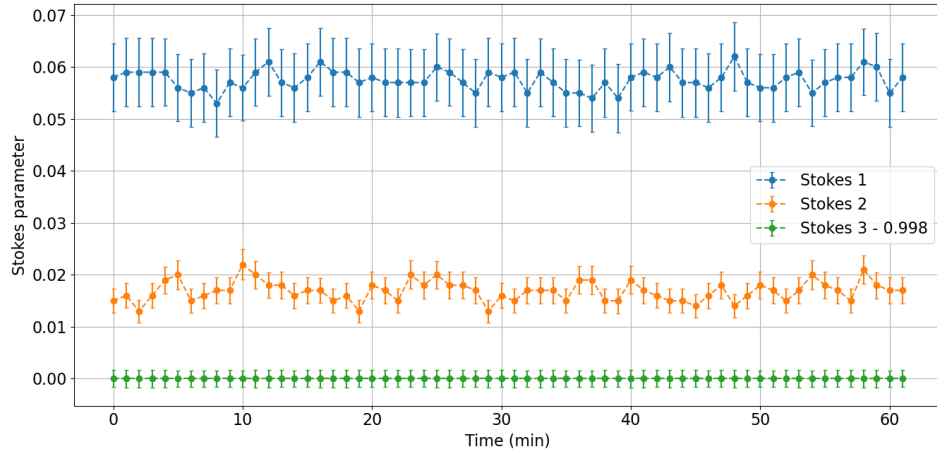


**Figure 5.2.4:** Right circular polarization stability at the ion position over a period of one hour. To the third parameter  $S_3$ , 0.998 has been subtracted for displaying purposes.

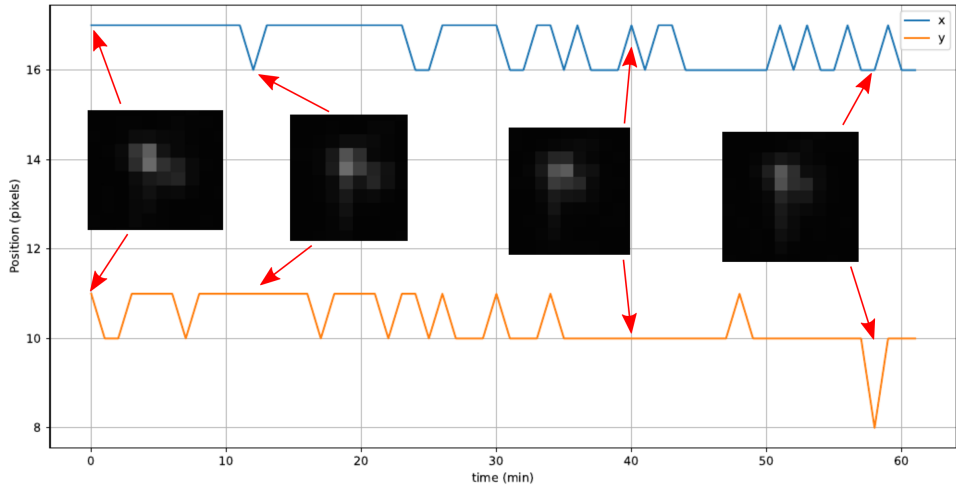


**Figure 5.2.5:** Beam pointing stability at the focus position over a period of one hour. The 2 lines represent the horizontal  $x$  and vertical  $y$  position of the beam in unit of pixels. In the insets, some examples of raw data are given.

## 5.3 Final installed system

After the tests presented in the previous sections, the setup was installed next to the ion chamber and focused on the ions as described in Section 4.4. As there is no more physical access to the focus spot, more advanced quantum optics experiments have to be carried out in order to measure properties of the system, such as focus spot size and addressing error. The first experiment designed aimed at measuring these two quantities: a Ramsey experiment was performed on four loaded ions, from which the beam shape in one direction (along the ion string) due to addressed AC Stark shifts on the ions could be measured. The second experiment involves three ions and the goal was to generate photons via a Raman process from one single ion leaving the states of the other two unaltered, demonstrating therefore the new possibility to emit single photons into the cavity, from individual ions in a string.

### 5.3.1 Single qubit manipulation



**Figure 5.3.1:** Pulse sequence of the Ramsey experiment. The sequence is repeated for different AOD frequencies which moves the 3-GHz-detuned addressed 393 nm beam across the ion string. From the ion excitations, measured by the imaging CCD camera, the Rabi frequency of the 393 nm laser can be inferred. All operations are on all ions simultaneously, except the 393 nm pulse which is ideally addressed. The length  $\tau$  was varying.

The goal of this experiment is to perform the Ramsey experiment discussed in Section 2.5.1. In summary, we want to sweep the 393 nm beam along the ion string, the sequence in Figure 5.3.1 is repeated for different AOD frequencies, and from the ion excitation we can infer the Rabi frequency of the 393 nm laser. The Rabi frequency can then be fitted to obtain the focus spot size. Before the experiment, some preliminary measurements have to be taken, thus in this section we show first the following:

- Global Rabi flops with 729 nm on the qubit transition, from this we can measure the  $\pi/2$  pulse time and show individual ion readout with the camera.
- Ramsey fringes without 393 nm, showing coherent control over the ion qubits.
- Addressed 393 nm pulse length scan, to determine the length  $\tau$  of the Raman pulse to achieve particular  $\sigma_z$  rotations and furthermore to estimate the addressing error.

These experiments were done with four ions loaded in the trap with endcap voltages of 714 V and 700V, for which numerical simulations yield an axial COM frequency of  $\sim 767$  kHz. The 393 nm laser was locked to the wavemeter and detuned from resonance by  $\sim 3$  GHz, ref. Section 2.5.1.

Global Rabi flops are shown in Figure 5.3.2. Some points are missing in the plot due to a melting event of the ion crystal. The system took the data points while ions were melted, therefore they have been removed. Rabi flops are damped due to the residual thermal distribution. Since we only perform Doppler cooling, ions are not in the ground

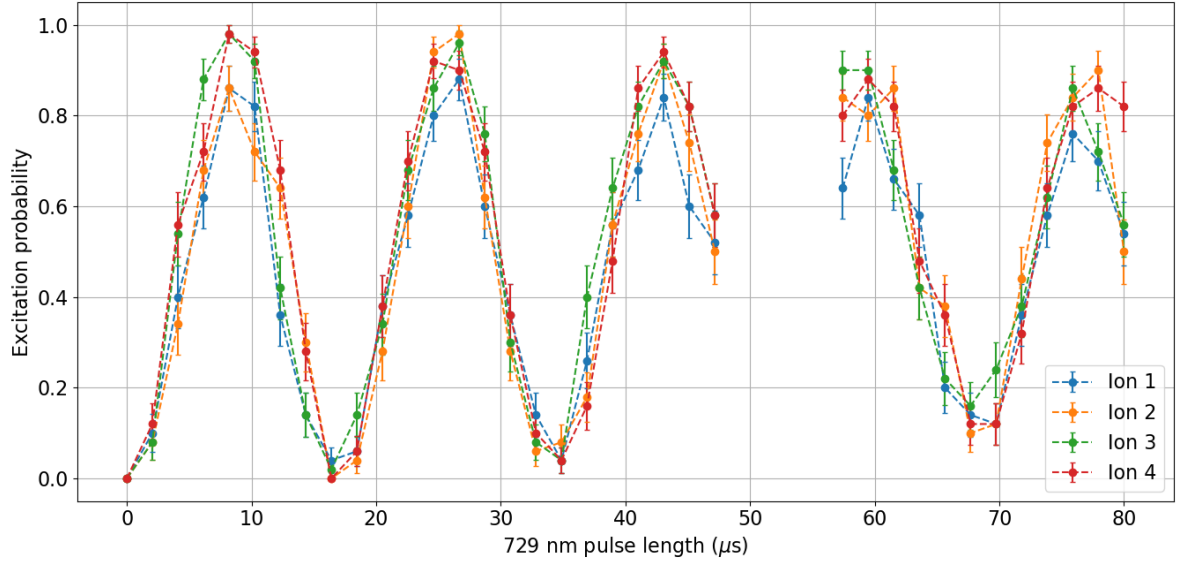


**Figure 5.3.2:** 729 nm global Rabi flops on 4 ions measured with the camera. Errorbars on the excitation probability ( $P_D$ ) have been assigned according to the error on estimating the probability of a binomial distribution. Some points were removed due to a melting event.

state, but rather in a thermal state [19]. The  $\pi/2$  time is extrapolated from the first flop as the time it takes for the ions to first reach excitation probability  $P_D = 0.5$ , we estimated  $4.2 \mu\text{s}$ . Errorbars on the excitation probability have been assigned according to the error on estimating the probability of a binomial distribution [75]

$$\sigma = \sqrt{\frac{P_D(1 - P_D)}{N}}, \quad (5.3.1)$$

where  $N = 50$  is the number of repetitions. Ramsey fringes without the 393 nm pulse are presented in Figure 5.3.3, the  $\pi/2$  time was set to  $4.2 \mu\text{s}$ . The phase  $\phi$  between the two pulses was scanned, and afterwards it was set to  $\phi = \pi/2$  for the rest of the experiment. The 393 nm pulse length  $\tau$  was scanned inside the Ramsey experiment, the flops are shown in Figure 5.3.4. For the next experiment, to get the beam profile across the ion string, we chose  $\tau$  of  $25 \mu\text{s}$ ; in this case, the ion is not fully flipped and the later analysis is therefore simpler. It was checked that  $\tau$  is the same for every ion. Finally, the AOD frequency is scanned, during this scan the beam is moved from ion to ion, for each beam position, the excitation probability of all ions is measured, this is then translated to a Rabi frequency with Equation (2.5.4). The square of the Rabi frequency, determined from the probability  $P_D$ , gives the laser intensity of the beam. The obtained intensity profile as a function of the AOD driving frequency is presented in Figure 5.3.5. To calibrate the beam position scale in micrometers, the axial COM mode (767 kHz) of the trap is measured by performing 729 nm spectroscopy on the carrier and motional sideband. Ion positions can be then numerically calculated (cf. Section 2.3.2). AOD frequencies corresponding to the maxima in Figure 5.3.5 are attributed to the ion positions, and corresponding frequency shifts to distances. By comparison, we found a conversion factor of  $3.03 \mu\text{m}/\text{MHz}$ . The four peaks have been fitted with a Gaussian function to obtain the waist of the beam when focused on the different ions. The waists yielded by the fits are from right to left

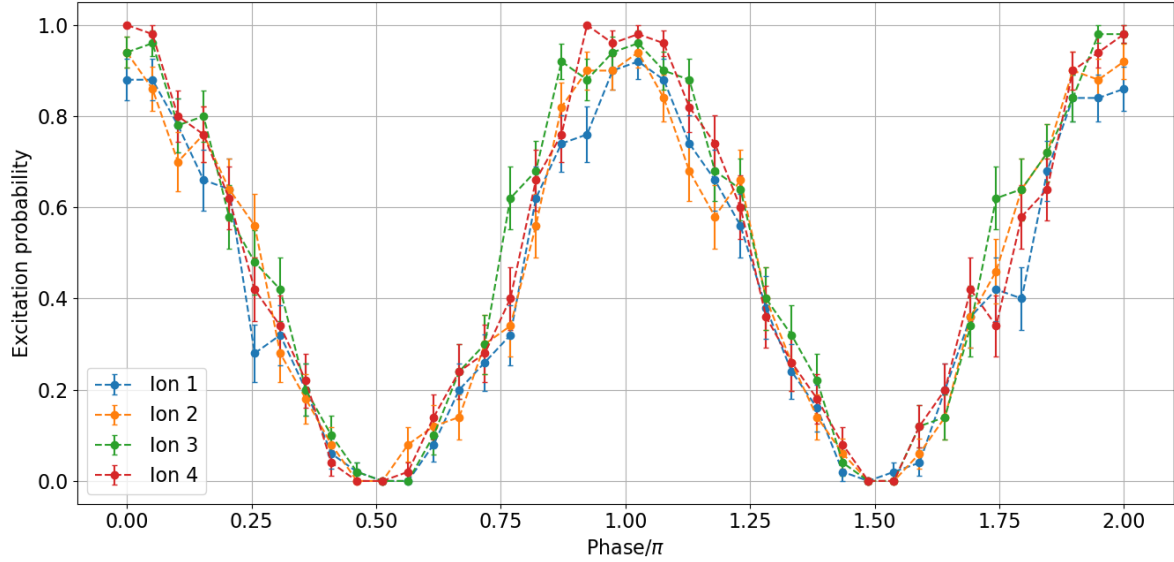


**Figure 5.3.3:** Ramsey fringes for 4 ions without 393 nm. A  $\cos^2(\phi)$  behavior can be noticed showing coherent control of the ion states.

$$\omega_1 = 1.23 \pm 0.20 \mu\text{m}, \omega_2 = 1.25 \pm 0.19 \mu\text{m}, \omega_3 = 1.35 \pm 0.22 \mu\text{m}, \omega_4 = 1.39 \pm 0.20 \mu\text{m}.$$

Figure 5.3.4 allows the addressing error to be determined, when aiming at ion 3. In this measurement, the addressing beam was focused on one ion and the Raman length  $\tau$  is scanned. This increases the interaction time of the laser with the ions, and if the interaction is long enough even the tail of a Gaussian can induce some excitation on the ions on the side of the one being addressed. In the scan displayed, the pulse length reached  $300 \mu\text{s}$  and there is no statistically significant excitation on any ion apart from the one flopping. Other scans went up to  $500 \mu\text{s}$ , and still no visual excitation was present. While this means that no quantitative number can be determined for the addressing error, an upper bound can still be given. A sinusoidal fit  $B \sin^2(A\tau)$  has been done on the data, it is not perfect probably due to intensity fluctuations of the lasers, or magnetic field fluctuations. Nonetheless, from the fit we can determine the Rabi frequency on the third ion as  $\Omega_3 = \sqrt{4\Delta \cdot A} = 2\pi \times 22 \text{ MHz}$ , see Equation (2.5.3). Assuming in the worst case scenario that an excitation  $P_D > 0.05$  on the second ion appears right after  $500 \mu\text{s}$ , i.e. the Rabi frequency of the non-addressed ion is  $2\pi \times 2 \text{ MHz}$ , the addressing error on the intensity should be at most  $\Omega_2^2/\Omega_3^2 < 10^{-2}$ .

During this experiment we scanned the AOD twice with an interval of 30 minutes to measure the beam pointing stability of the system. In Figure 5.3.6 the beam profile on the third ion has been overlapped between the two scans. A Gaussian fit gives the central frequencies, and their difference determines the beam pointing stability over a period of 30 minutes, we estimated a stability of  $0.20 \pm 0.07 \mu\text{m}/\text{hr}$ .

To conclude, we remark that in the presented experiments of this section the 393 nm pulse acts as a single qubit gate on individual ions. The Ramsey experiment carried out by scanning the AOD frequency demonstrated the ability of the system to manipulate single qubits as it includes a single qubit rotation  $\sigma_z$  first introduced in Section 2.1.1. The Ramsey experiment therefore fulfills Goal 2 of this thesis, however the gate quality of  $\sigma_z$  needs to be studied more carefully in the future.

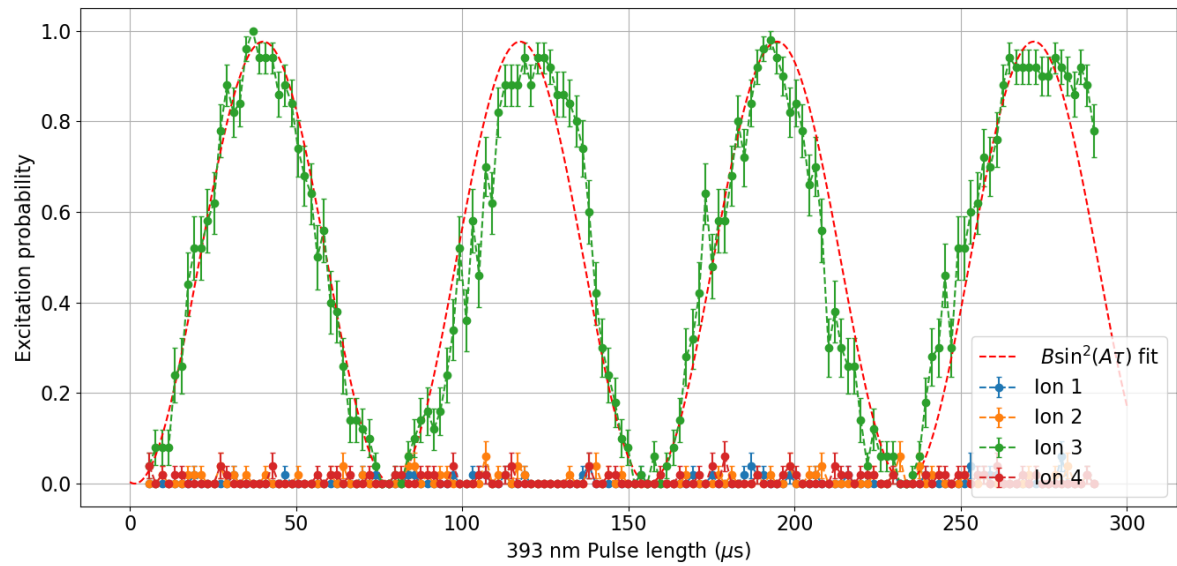


**Figure 5.3.4:** 393 nm AC Stark flops. The pulse length  $\tau$  of the 393 nm laser is scanned while shining over one single ion. The red curve is a fit of  $B \sin^2(A\tau)$ , where  $A$  is proportional to the Rabi frequency of the laser focused on the third ion.

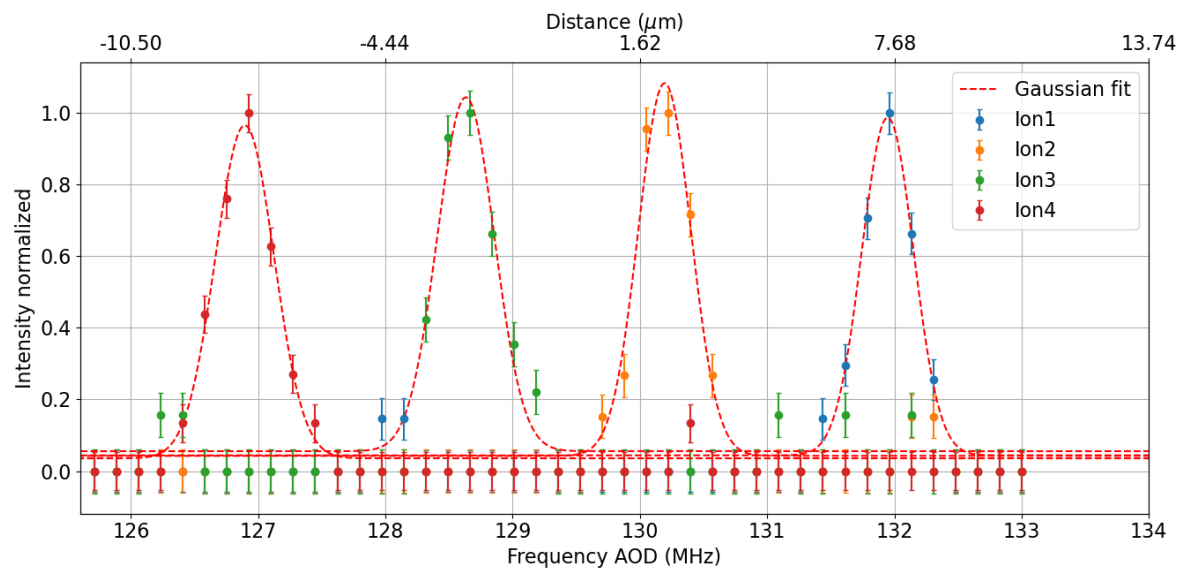


**Figure 5.3.5:** AOD scanning of four ions via Ramsey interferometry. The normalized intensity comes from the Rabi frequency calculated from the measured excitation probability  $P_D$  using formula (2.5.4). The upper micrometer scale is calibrated by comparing the center of the Gaussian fit with the numerically calculated ion positions.

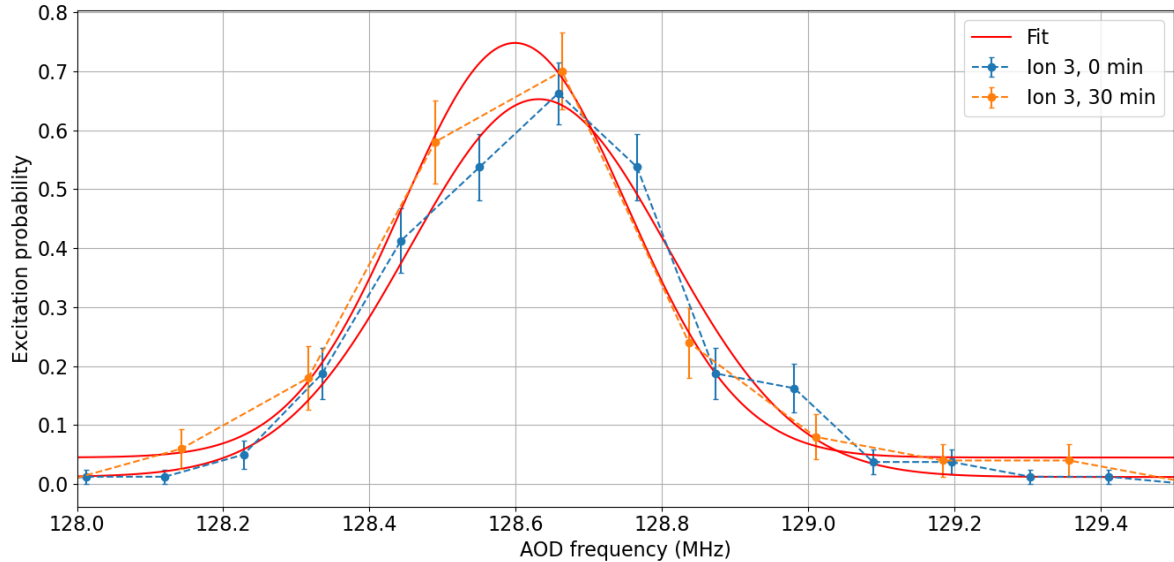


**Figure 5.3.6:** AOD scanning on one single ion repeated after 30 minutes to measure the beam pointing stability as difference of the center of the two peaks:  $0.20 \pm 0.07 \mu\text{m}/\text{hr}$ . Processing of the data has been done as in Figure 5.3.5.

### 5.3.2 Photon production

The second thesis goal is to generate single cavity photons from individual ions in a chain. Photons are produced by a pulse of 393 nm light focused on the central ion of three via the cavity-mediated Raman process described in Section 2.5.2. The length of the Raman pulse is scanned and the integrated photon detection probability is recorded, measured leaving the cavity. The generated photon is emitted into the cavity, transmitted through the output mirror of the cavity, coupled into an optical fiber, and passes through waveplates and a PBS before reaching a superconducting nanowire single-photon detector (SNSPD)<sup>2</sup>. In contrast to the previous experiment where the 393 nm laser is used to impart an AC Stark shift, here the precise (to the kHz level) frequency of the Raman laser is key to generating cavity photons (the cavity has a linewidth of  $\sim 70$  kHz and the laser should be significantly less for efficient photon generation). Therefore, to generate photons, the 393 nm laser is locked to an external cavity (linewidth  $\sim 100$  Hz Ref. [36]). The existing AOM network was established to leave the Raman laser 400 MHz detuned from the S-P transition. To account for the additional 127 MHz detuning of the AOD, we shifted the frequency of two AOMs in the 393 nm setup (see Section 3.2).

We loaded three ions in the trap with a measured axial COM frequency of  $\sim 820$  kHz, which means ion separations of  $5.4 \mu\text{m}$ . We locked the 393 nm laser to the cavity and scanned the frequency with the double pass AOM 1 (ref. Figure 3.2.1). The transition chosen is  $|S_{1/2}, -\frac{1}{2}\rangle \rightarrow |D_{5/2}, -\frac{3}{2}\rangle$ , see details in Section 2.5.2. The cavity position along its principal axis was optimized using a piezo in order to maximize overall 854 nm photon count rate when driving the Raman process with the addressed beam aligned to the central ion, and simultaneously repumping the 854 nm transition (so multiple photons can be generated to enhance the signal). Assuming that the central ion is at a maximum of the

<sup>2</sup>Scontel SNSPD model FCOPRS-CCR, 854 nm detectors:  $\sim 87\%$  efficiency,  $\sim 0.5$  dark counts per second.

cavity field and that the cavity-trap angle is  $4.6^\circ$ , we calculated that the two outer ions are at 82 % of the cavity maximum. In the experiment we included an initial stage of Doppler cooling and a final stage of ion qubit-state detection with the camera. Furthermore, the 806 nm cavity locking light was switched off during the photon generation process, in this time the cavity maintained its position with a sample and hold. For each Raman pulse length, the experiment is repeated  $N = 200$  times to get an estimate for the average photon probability and the ion excitation probability ( $P_D$  the probability to find the ion in the D<sub>5/2</sub> manifold). Errorbars on the excitation probability are calculated as in the previous section (Equation (5.3.1)), while for the photon probability the error is modelled by Poissonian statistics [76]

$$\sigma_{ph} = \frac{\sqrt{N_{click}}}{N}, \quad (5.3.2)$$

where  $N_{click}$  is the number of times a photon has been detected with respect to the total  $N$  repetitions.

The experiment consisted of scanning the Raman pulse length, and for each length, the photon detection probability and the ion excitation probability  $P_D$  have been measured. In Figure 5.3.7, the photon detection probability is plotted. From polarization selection rules, we expect a  $\pi$  polarized photon to be emitted. As the cavity is perpendicular to the magnetic field, the photon in the cavity is linearly polarized and is then rotated with waveplates such that it goes to one output port of the PBS. Consistent with the expectations, we can see that we measured mostly vertical polarized photons. The photons are not perfectly polarized which could be due to imperfections of the polarization analysis, e.g. errors in the settings of waveplates.

The excitation probability  $P_D$  is plotted in Figure 5.3.8. In this figure, we can see that only the addressed ion is excited to the D<sub>5/2</sub> state, while the others show no excitation at all.  $P_D$  does not reach 1, perfect population transfer is not achieved due to non-zero spontaneous emission from the P<sub>3/2</sub> state to the D<sub>3/2</sub> state, or to the  $|S_{1/2}, +\frac{1}{2}\rangle$  state. Unfortunately, we were not able to simulate theoretical curves for both of the plots, as the experiment was carried out in one day at the end of the time available for my master work. As such, no careful optimization was done on the polarization of the driving addressing beam, which means that the parameters (specifically, the Rabi frequency of the addressed laser) are not well known enough to do a theoretical model. We remind that the two outer ions are still coupled to the cavity to a significant extent (82% coupling expected) such that they are in a condition to generate photons if the addressed beam were to drive them. In fact, we also observed photon generations when addressing outer ions.

In conclusion, we observed the addressed ion getting excited to the D<sub>5/2</sub> state and simultaneously detected vertical polarized photons. Therefore, these data are consistent with only the addressed ion emitting a cavity photons.

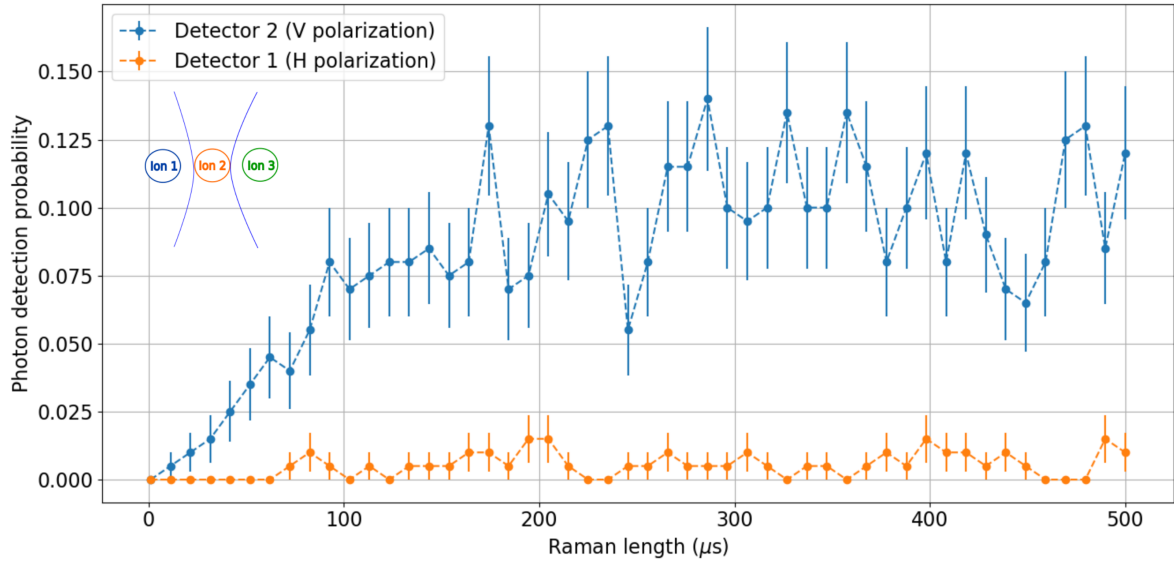


**Figure 5.3.7:** Measured cavity photon detection probability as a function of addressed Raman laser pulse length. The two detectors measure the Horizontal (orange data points) and Vertical (blue data points) photons emitted by the ion, in Figure 5.3.8 excitations of the ions during the process are plotted. Inset: diagram of the situation where only the middle ion is addressed.

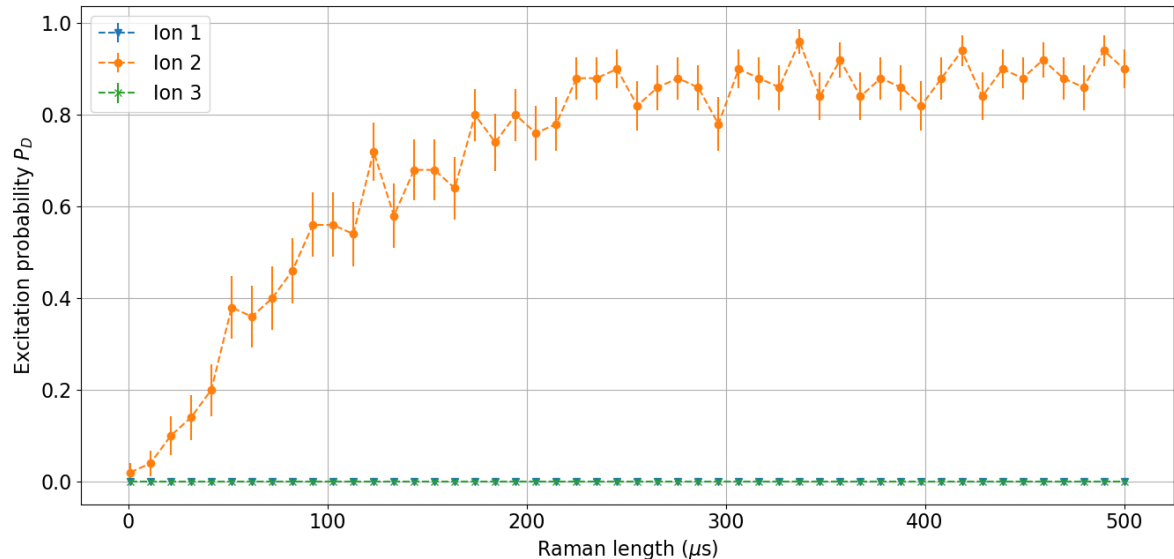


**Figure 5.3.8:** Qubit excitation state of the ions  $P_D$  as a function of addressed Raman laser pulse length. In Figure 5.3.7 photon detection probability during the same experiment is plotted.

# Chapter 6

## Conclusions and outlook

In this thesis, an optical setup for single ion focusing of a 393 nm laser has been designed, built and tested. The design was based on the setups built in other experiments, but it has been improved to avoid clipping that limited the addressing range. The software Zemax was used to design and check the performance of the design. Optimal lenses for the construction were found with the software. Once the simulation was satisfactory, a test setup was built on an optical table where it has been characterized in terms of focal spot size, polarization capabilities, and stability. Here the smallest waist measured was 2.4  $\mu\text{m}$ , the switching time of the AOD was in the order of 7-8  $\mu\text{s}$ , and addressing range  $>150 \mu\text{m}$ . Afterwards, the setup was moved and aligned on the ions, where limited physical access did not allow for such easy checks, but instead more advanced quantum optics experiments have been performed.

The setup was used for single photon generation and single qubit manipulation. Both of the purposes has been fulfilled: the photon generation was demonstrated in the experiment in Section 5.3.2, here a string of three ions was loaded into the trap and the focused laser aligned with the central one. A laser pulse triggered the photon generation exclusively from the intended ion. The photon detection probability was  $\sim 12\%$ , and can be further improved as particular attention was not given to the polarization of the addressed Raman beam, but the system already has the capabilities for precise polarization setting. One method to improve photon generation efficiency is to change the principle quantization axes, set by permanent magnets, to a direction parallel to the addressed laser direction.

Qubit manipulation was carried out in the Ramsey interferometer experiment, here we measured the AC stark shift caused by the 393 nm light by imprinting a phase on the qubit encoded in the 729 nm transition. We were able to rotate individual qubits around the z axis, and flip the state of an individual qubit with a quality of 97%. Moreover, with this experiment the waist of beam was measured to be  $1.2 - 1.3 \mu\text{m}$  over a  $15 \mu\text{m}$  string of 4 ions, and no addressing error was measured up to  $10^{-2}$ , for 4 ions separated by 4.7-5.1  $\mu\text{m}$ . In a neighboring advanced trapped-ion quantum simulation experiment a waist of  $1.44 \mu\text{m}$  was achieved using the same objective but at 729 nm [17].

Improvements are possible in this addressing system: the switching speed can be reduced, by e.g. reducing the beam diameter and moving it closer to the piezo. The waist is limited by the objective aperture, so increasing the size of the objective would help achieving a smaller waist.

The next natural step is the generation of sequential photons from different ions and this is currently undergoing at the moment of this thesis writing. Afterwards, entanglement can also be produced between a single ion and a photon. Once entanglement is achieved

different investigation prospects will open. We can investigate sending trains of entangled photons to improve the bandwidth of establishing long-distance entanglement [38], or investigate distribution of multi-partite photon entanglement over distance, which requires mapping multi-partite entanglement onto the travelling photons [77].

# Bibliography

- [1] Antonio Acín, Immanuel Bloch, Harry Buhrman, Tommaso Calarco, Christopher Eichler, Jens Eisert, Daniel Esteve, Nicolas Gisin, Steffen J Glaser, Fedor Jelezko, Stefan Kuhr, Maciej Lewenstein, Max F Riedel, Piet O Schmidt, Rob Thew, Andreas Wallraff, Ian Walmsley, and Frank K Wilhelm. The quantum technologies roadmap: a european community view. *New Journal of Physics*, 20(8):080201, aug 2018.
- [2] Peter W. Shor. Polynomial-time algorithms for prime factorization and discrete logarithms on a quantum computer. *SIAM J. Comput.*, 26(5):1484–1509, oct 1997.
- [3] I. M. Georgescu, S. Ashhab, and Franco Nori. Quantum simulation. *Rev. Mod. Phys.*, 86:153–185, Mar 2014.
- [4] H. J. Kimble. The quantum internet. *Nature*, 453(7198):1023–1030, jun 2008.
- [5] Stephanie Wehner, David Elkouss, and Ronald Hanson. Quantum internet: A vision for the road ahead. *Science*, 362(6412), 2018.
- [6] *Proceedings of IEEE International Conference on Computers, Systems and Signal Processing*, 1984.
- [7] Ivan B. Damgård, Serge Fehr, Louis Salvail, and Christian Schaffner. Cryptography in the bounded quantum-storage model. In *Proceedings of the 46th Annual IEEE Symposium on Foundations of Computer Science*, FOCS ’05, pages 449–458, Washington, DC, USA, 2005. IEEE Computer Society.
- [8] Joseph F. Fitzsimons. Private quantum computation: an introduction to blind quantum computing and related protocols. *npj Quantum Information*, 3(1), jun 2017.
- [9] P. Kómár, E. M. Kessler, M. Bishof, L. Jiang, A. S. Sørensen, J. Ye, and M. D. Lukin. A quantum network of clocks. *Nature Physics*, 10(8):582–587, jun 2014.
- [10] Daniel Gottesman, Thomas Jennewein, and Sarah Croke. Longer-baseline telescopes using quantum repeaters. *Phys. Rev. Lett.*, 109:070503, Aug 2012.
- [11] Vasil S. Denchev and Gopal Pandurangan. Distributed quantum computing: A new frontier in distributed systems or science fiction? *SIGACT News*, 39(3):77–95, September 2008.
- [12] C. Monroe, R. Raussendorf, A. Ruthven, K. R. Brown, P. Maunz, L.-M. Duan, and J. Kim. Large-scale modular quantum-computer architecture with atomic memory and photonic interconnects. *Phys. Rev. A*, 89:022317, Feb 2014.
- [13] J. I. Cirac and P. Zoller. Quantum computations with cold trapped ions. *Phys. Rev. Lett.*, 74:4091–4094, May 1995.
- [14] Andreas Stute, Bernardo Casabone, Bernhard Brandstätter, Dr. M. Habicher, H. G. Barros, Piet O. Schmidt, Tracy E. Northup, and Rainer Blatt. Toward an ion–photon quantum interface in an optical cavity. *Applied Physics B*, 107:1145–1157, 2012.
- [15] Isaac L. Chuang Michael A. Nielsen. *Quantum computation and quantum information*. Cambridge Series on Information and the Natural Sciences. Cambridge University

- Press, 1 edition, 2004.
- [16] H. Häffner, S. Gulde, M. Riebe, G. Lancaster, C. Becher, J. Eschner, F. Schmidt-Kaler, and R. Blatt. Precision measurement and compensation of optical stark shifts for an ion-trap quantum processor. *Phys. Rev. Lett.*, 90:143602, Apr 2003.
  - [17] Cornelius Hempel. *Digital quantum simulation, Schroedinger cat state spectroscopy and setting up a linear ion trap*. PhD thesis, University of Innsbruck, 2014.
  - [18] H. C. Nägerl, Ch. Roos, D. Leibfried, H. Rohde, G. Thalhammer, J. Eschner, F. Schmidt-Kaler, and R. Blatt. Investigating a qubit candidate: Spectroscopy on the  $S_{1/2}$  to  $D_{5/2}$  transition of a trapped calcium ion in a linear paul trap. *Phys. Rev. A*, 61:023405, Jan 2000.
  - [19] Christian Roos. *Controlling the quantum state of trapped ions*. PhD thesis, University of Innsbruck, 2000.
  - [20] Daniel Adam Steck. Quantum and atom optics.
  - [21] D.F.V. James. Quantum computation with hot and cold ions: An assessment of proposed schemes. *Fortschritte der Physik*, 48(9-11):823–837, 2000.
  - [22] Carlos Manuel da Silva Baptista Russo. *Photon statistics of a single ion coupled to a high-finesse cavity*. PhD thesis, University of Innsbruck, 2008.
  - [23] P. Zoller C. Gardiner. *Quantum Noise*. Springer-Verlag Berlin Heidelberg, 2004.
  - [24] David P. DiVincenzo. The physical implementation of quantum computation. *Fortschritte der Physik*, 48(9-11):771–783, 2000.
  - [25] Richard J Hughes, Jane E Nordholt, Derek Derkacs, and Charles G Peterson. Practical free-space quantum key distribution over 10 km in daylight and at night. *New Journal of Physics*, 4:43–43, July 2002.
  - [26] L.-M. Duan and C. Monroe. Colloquium: Quantum networks with trapped ions. *Rev. Mod. Phys.*, 82:1209–1224, Apr 2010.
  - [27] Stephan Ritter, Christian Nölleke, Carolin Hahn, Andreas Reiserer, Andreas Neuzner, Manuel Uphoff, Martin Mücke, Eden Figueroa, Joerg Bochmann, and Gerhard Rempe. An elementary quantum network of single atoms in optical cavities. *Nature*, 484(7393):195–200, apr 2012.
  - [28] W. K. Wootters and W. H. Zurek. A single quantum cannot be cloned. *Nature*, 299(5886):802–803, oct 1982.
  - [29] H.-J. Briegel, W. Dür, J. I. Cirac, and P. Zoller. Quantum repeaters: The role of imperfect local operations in quantum communication. *Phys. Rev. Lett.*, 81:5932–5935, Dec 1998.
  - [30] Jian-Wei Pan, Christoph Simon, Časlav Brukner, and Anton Zeilinger. Entanglement purification for quantum communication. *Nature*, 410(6832):1067–1070, April 2001.
  - [31] Charles H. Bennett, Gilles Brassard, Claude Crépeau, Richard Jozsa, Asher Peres, and William K. Wootters. Teleporting an unknown quantum state via dual classical and einstein-podolsky-rosen channels. *Phys. Rev. Lett.*, 70:1895–1899, Mar 1993.
  - [32] G. Araneda, D. B. Higginbottom, L. Slodička, Y. Colombe, and R. Blatt. Interference of single photons emitted by entangled atoms in free space. *Phys. Rev. Lett.*, 120:193603, May 2018.
  - [33] Matthias Keller, Birgit Lange, Kazuhiro Hayasaka, Wolfgang Lange, and Herbert Walther. Continuous generation of single photons with controlled waveform in an ion-trap cavity system. *Nature*, 431(7012):1075–1078, October 2004.
  - [34] H. J. Kimble. Strong interactions of single atoms and photons in cavity QED. *Physica*

- Scripta*, T76(1):127, 1998.
- [35] Helmut Ritsch, Peter Domokos, Ferdinand Brennecke, and Tilman Esslinger. Cold atoms in cavity-generated dynamical optical potentials. *Rev. Mod. Phys.*, 85:553–601, Apr 2013.
  - [36] Helene Hainzer. Laser locking for trapped-ion quantum networks. Master’s thesis, University of Innsbruck, 2018.
  - [37] H. G. Barros, A. Stute, T. E. Northup, C. Russo, P. O. Schmidt, and R. Blatt. Deterministic single-photon source from a single ion. *New Journal of Physics*, 11(10):103004, October 2009.
  - [38] V. Krutyanskiy, M. Meraner, J. Schupp, V. Krcmarsky, H. Hainzer, and B. P. Lanyon. Light-matter entanglement over 50 km of optical fibre. *npj Quantum Information*, 5(1), August 2019.
  - [39] Lowell S. Brown and Gerald Gabrielse. Geonium theory: Physics of a single electron or ion in a penning trap. *Rev. Mod. Phys.*, 58:233–311, Jan 1986.
  - [40] Wolfgang Paul. Electromagnetic traps for charged and neutral particles. *Rev. Mod. Phys.*, 62:531–540, Jul 1990.
  - [41] Philip E. Miller and M. Bonner Denton. The quadrupole mass filter: Basic operating concepts. *Journal of Chemical Education*, 63(7):617, 1986.
  - [42] J. A. Richards. *The Mathieu Equation*, pages 93–107. Springer Berlin Heidelberg, Berlin, Heidelberg, 1983.
  - [43] D. Leibfried, R. Blatt, C. Monroe, and D. Wineland. Quantum dynamics of single trapped ions. *Rev. Mod. Phys.*, 75:281–324, Mar 2003.
  - [44] D. F. V. James. Quantum dynamics of cold trapped ions with application to quantum computation. *Applied Physics B: Lasers and Optics*, 66(2):pp. 181–90.
  - [45] G. Audi, A.H. Wapstra, and C. Thibault. The ame2003 atomic mass evaluation: (ii). tables, graphs and references. *Nuclear Physics A*, 729(1):337 – 676, 2003. The 2003 NUBASE and Atomic Mass Evaluations.
  - [46] D.J. Wineland, C. Monroe, W.M. Itano, D. Leibfried, B.E. King, and D.M. Meekhof. Experimental issues in coherent quantum-state manipulation of trapped atomic ions. *Journal of Research of the National Institute of Standards and Technology*, 103(3):259, May 1998.
  - [47] T. W. Hansch and A. L. Schawlow. Cooling of gases by laser radiation. *Optics Communications*, 13(1):68–69, Jan 1975.
  - [48] C.J. Foot. *Atomic Physics*. Oxford Master Series in Physics, 2004.
  - [49] Gabriel Andres Areneda Machuca. *Experiments with single photons emitted by single atoms*. PhD thesis, University of Innsbruck, 2019.
  - [50] Jürgen Eschner, Giovanna Morigi, Ferdinand Schmidt-Kaler, and Rainer Blatt. Laser cooling of trapped ions. *J. Opt. Soc. Am. B*, 20(5):1003–1015, May 2003.
  - [51] Bahaa E. A. Saleh and Malvin Carl Teich. *Fundamentals of photonics*. Wiley Series in Pure and Applied Optics, 2 edition, 2007.
  - [52] C. S. Williams. Gaussian beam formulas from diffraction theory. *Appl. Opt.*, 12(4):872–876, Apr 1973.
  - [53] Wolfgang Demtroeder. *Laser Spectroscopy 1: Basic Principles*. Springer, 2014.
  - [54] A. Korpel. Acousto-optics—a review of fundamentals. *Proceedings of the IEEE*, 69(1):48–53, 1981.
  - [55] G.R.B.E. Römer and P. Bechtold. Electro-optic and acousto-optic laser beam scanners.

- Physics Procedia*, 56:29–39, 2014.
- [56] Michael Bass, Eric W. Van Stryland, David R. Williams, and Williams L. Wolfe. *Handbook of Optics Volume II Devices, Measurements, and Properties 2nd edition*. 1995.
  - [57] Norman F. Ramsey. A molecular beam resonance method with separated oscillating fields. *Physical Review*, 78(6):695–699, jun 1950.
  - [58] H. Ball, M. W. Lee, S. D. Gensemer, and M. J. Biercuk. A high-power 626 nm diode laser system for beryllium ion trapping. *Review of Scientific Instruments*, 84(6):063107, 2013.
  - [59] M. R. Dietrich, N. Kurz, T. Noel, G. Shu, and B. B. Blinov. Hyperfine and optical barium ion qubits. *Phys. Rev. A*, 81:052328, May 2010.
  - [60] D. J. Berkeland. Linear paul trap for strontium ions. *Review of Scientific Instruments*, 73(8):2856–2860, 2002.
  - [61] A. S. Bell, P. Gill, H. A. Klein, A. P. Levick, Chr. Tamm, and D. Schnier. Laser cooling of trapped ytterbium ions using a four-level optical-excitation scheme. *Phys. Rev. A*, 44:R20–R23, Jul 1991.
  - [62] R.C. Thompson, G.P. Barwood, and P. Gill. Laser cooling of magnesium ions confined in a penning trap. *Optica Acta: International Journal of Optics*, 33(4):535–543, 1986.
  - [63] R. Blatt, H. Haeffner, C. F. Roos, C. Becher, and F. Schmidt-Kaler. Ion trap quantum computing with ca+ ions. *Quantum Information Processing*, 3(1-5):61–73, October 2004.
  - [64] T. Ruster, C. T. Schmiegelow, H. Kaufmann, C. Warschburger, F. Schmidt-Kaler, and U. G. Poschinger. A long-lived zeeman trapped-ion qubit. *Applied Physics B*, 122(10), September 2016.
  - [65] Andreas tute. *A light-matter quantum interface: ion-photon entanglement and state mapping*. PhD thesis, University of Innsbruck, 2012.
  - [66] S. Gulde, D. Rotter, P. Barton, F. Schmidt-Kaler, R. Blatt, and W. Hogervorst. Simple and efficient photo-ionization loading of ions for precision ion-trapping experiments. *Applied Physics B*, 73(8):861–863, December 2001.
  - [67] H. C. Nägerl, D. Leibfried, H. Rohde, G. Thalhammer, J. Eschner, F. Schmidt-Kaler, and R. Blatt. Laser addressing of individual ions in a linear ion trap. *Phys. Rev. A*, 60:145–148, Jul 1999.
  - [68] S. Crain, E. Mount, S. Baek, and J. Kim. Individual addressing of trapped 171yb+ ion qubits using a microelectromechanical systems-based beam steering system. *Applied Physics Letters*, 105(18):181115, 2014.
  - [69] M. Johanning, A. Braun, N. Timoney, V. Elman, W. Neuhauser, and Chr. Wunderlich. Individual addressing of trapped ions and coupling of motional and spin states using rf radiation. *Phys. Rev. Lett.*, 102:073004, Feb 2009.
  - [70] Fiber Collimators 60FC. <https://www.sukhamburg.com/download/fibercollimators60fc.pdf>.
  - [71] M. Riedl. *Optical Design Fundamentals for Infrared Systems*. SPIE Press, 2011.
  - [72] Yasuzi Suzuki and Atsushi Tachibana. Measurement of the  $\mu\text{m}$  sized radius of gaussian laser beam using the scanning knife-edge. *Applied Optics*, 14(12):2809, December 1975.
  - [73] Bruce Cannon, Timothy S. Gardner, and Donald K. Cohen. Measurement of 1- $\mu\text{m}$  diam beams. *Appl. Opt.*, 25(17):2981–2983, Sep 1986.
  - [74] William H. McMaster. Polarization and the stokes parameters. *American Journal of*

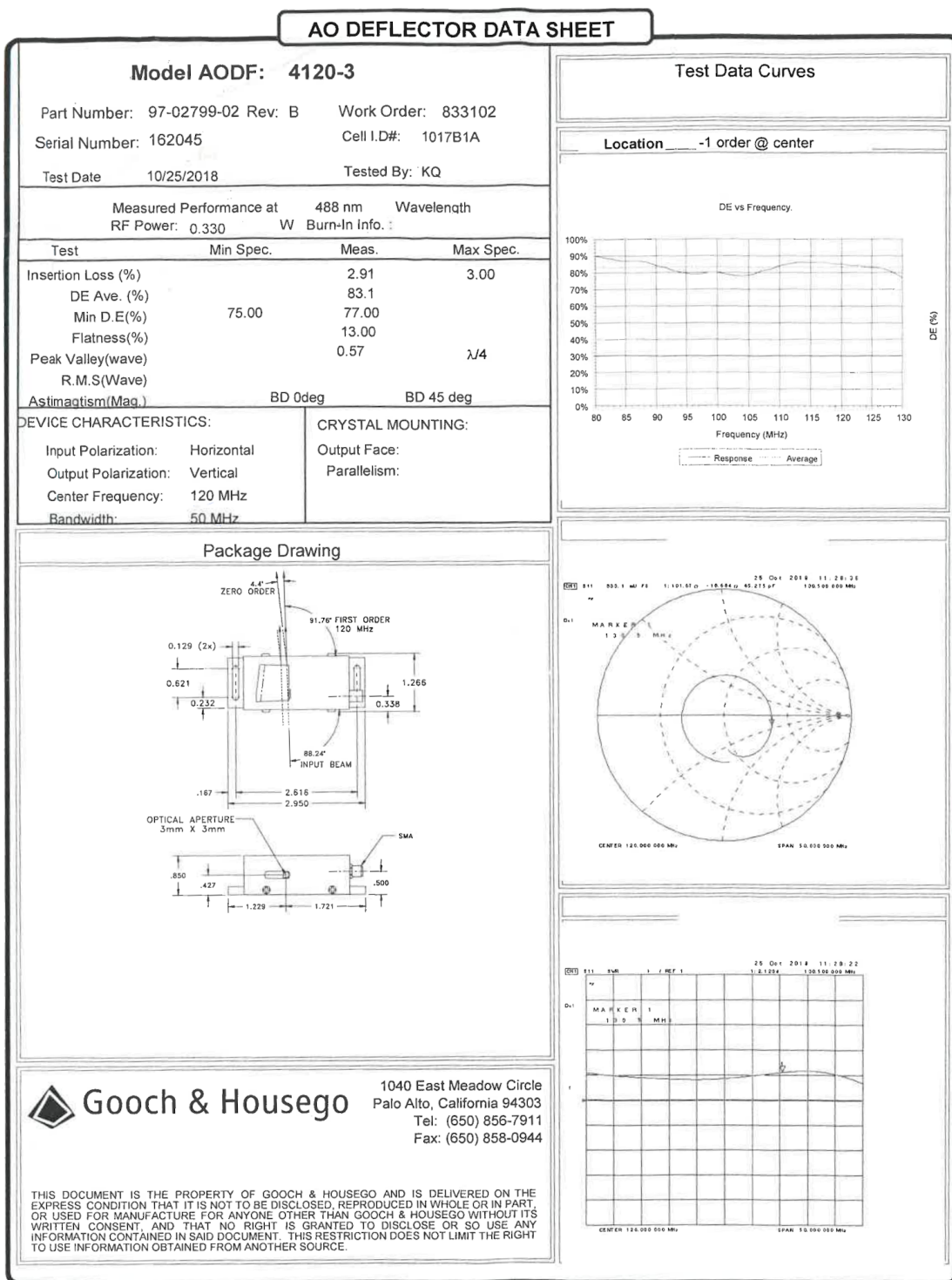
- Physics*, 22(6):351–362, 1954.
- [75] Richard J. Rossi. *Mathematical Statistics: An Introduction to Likelihood Based Inference*. Wiley, 2008.
- [76] Mark Fox. *Quantum optics: an introduction*. Oxford Master Series in Physics, 6. Oxford University Press, USA, 2006.
- [77] Jan Arenskötter, Stephan Kucera, Matthias Kreis, Floriane Brunei, Pascal Eich, Philipp Müller, and Jürgen Eschner. Atom-to-photon state mapping by quantum teleportation. In *Quantum Information and Measurement (QIM) V: Quantum Technologies*, page T5A.71. Optical Society of America, 2019.





# Appendix A

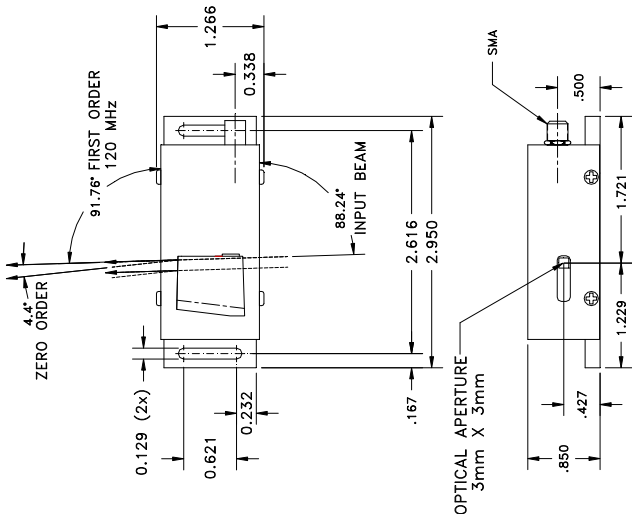
## AOD datasheet



## SPECIFICATIONS

AO Medium	TeO2
Acoustic Mode	Shear, off axis
Acoustic Velocity	.65 mm/ $\mu$ s
Wavelength	413 nm
Input Polarization	Horizontal
Output Polarization	Vertical
Insertion Loss	3%
Center Frequency ( $F_c$ )	120 MHz
RF Bandwidth	50 MHz
RF Power	<0.3 W
Active Aperture	3mm Diameter
Average Diffraction Efficiency	N/A
Flatness Across Bandwidth	N/A
Min Diffraction Efficiency	75%
Peak Valley at 633 nm	$\lambda/4$
RMS at 633 nm	N/A
VSWR	2.2:1
Scan Angle	N/A
Time Bandwidth	N/A

## OUTLINE DRAWING



### Notes:

1. First order @ 120mHz collinear to input +/- 45'
2. Impedance matching frequency range 80-145MHz

THIS DOCUMENT IS THE PROPERTY OF GOOCH & HOUSEGO. IT IS NOT TO BE REPRODUCED OR DISCLOSED IN WHOLE OR IN PART OTHER THAN BY EMPLOYEES OF GOOCH & HOUSEGO AND ITS CONTRACTED REPRESENTATIVES AND DISTRIBUTERS. ANY EXCEPTION REQUIRES THE WRITTEN CONSENT OF AN AUTHORIZED REPRESENTATIVE OF GOOCH & HOUSEGO.

TOLERANCES: .XXX ± .005	DR	T.Ng 9/3/2013	DESCRIPTION: AODF 4120-3
MATERIAL: CHK	APP		3MM APERTURE
FINISH: APP	APP		PART NUMBER: 97-02799-02
			REV: B SHEET 1 OF 1



# Appendix B

## Polarization characterization

Here we report the figures for the polarization characterization of section 5.2.3. Every figure contains a fit of a sine function  $A \sin(\omega x + \phi)$ , where  $x$  is the angle of the corresponding waveplate. The fits are used to determine the maxima and minima of the curves which indicates the closest point to the desired polarization, see table 5.2.1 for results.

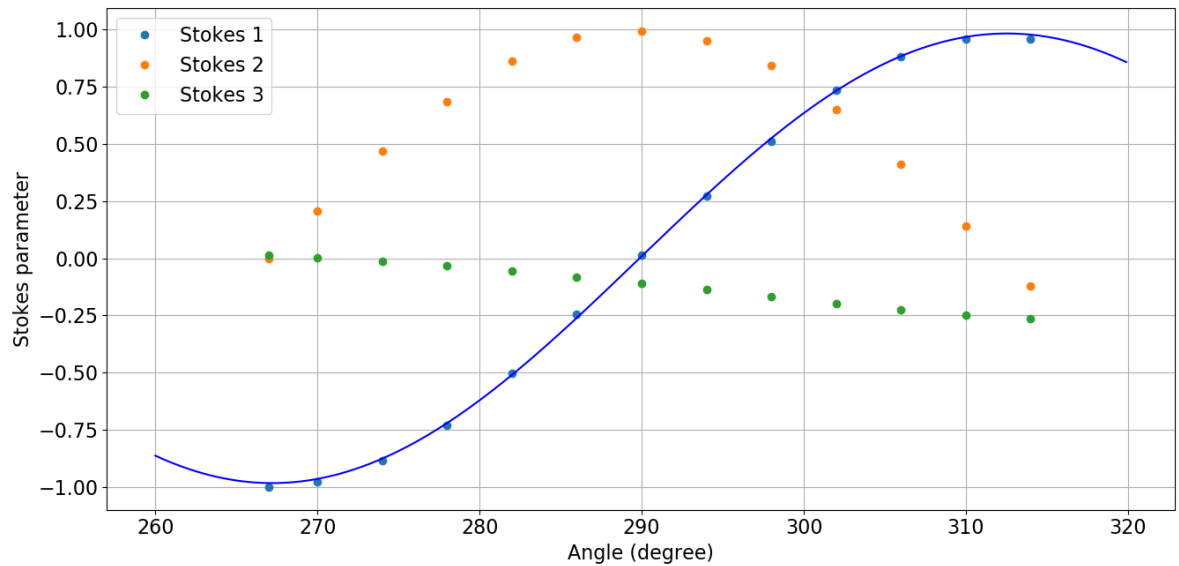


**Figure B.0.1:** Polarization after the  $\lambda/2$  WP B (see figure 4.1.1) as a function of the  $\lambda/2$  WP B angle. Blue line is a sine function fit:  $A = 0.983 \pm 0.007$ ,  $\pi/\omega = 45.3 \pm 0.6^\circ$ ,  $\phi = -2.20 \pm 0.05$  rad.

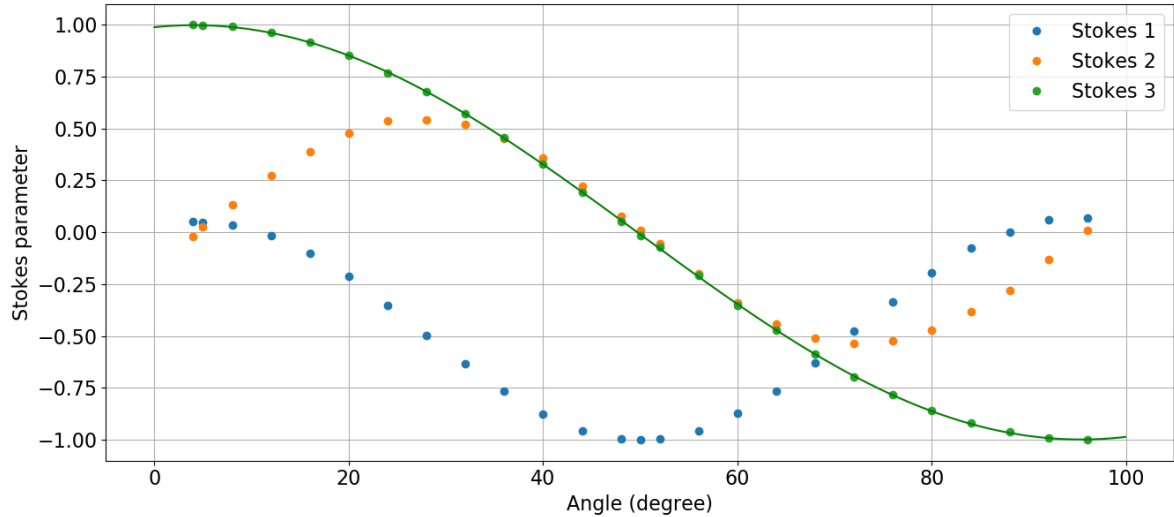


**Figure B.0.2:** Polarization after the objective at the focus spot as a function of the  $\lambda/4$  angle with  $\lambda/2$  WP B set to horizontal ( $267^\circ$ ). Green line is a sine function fit:  $A = 0.998 \pm 0.02$ ,  $\pi/\omega = 91.3 \pm 0.3^\circ$ ,  $\phi = -1.43 \pm 0.01$  rad.

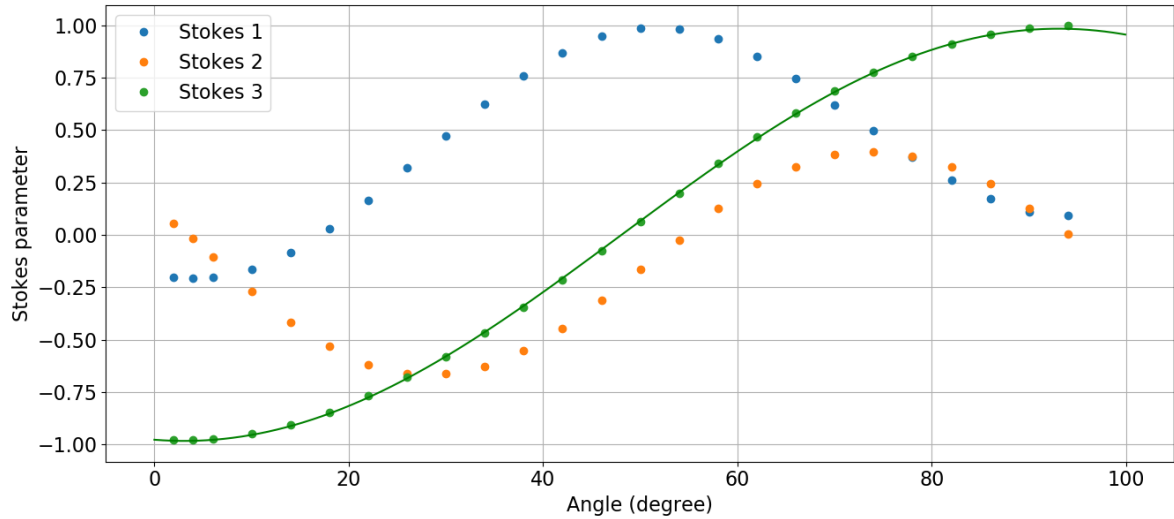


**Figure B.0.3:** Polarization after the objective at the focus spot as a function of the  $\lambda/4$  angle with  $\lambda/2$  WP B set to vertical ( $314^\circ$ ). Green line is a sine function fit:  $A = 0.982 \pm 0.003$ ,  $\pi/\omega = 90.0 \pm 0.5^\circ$ ,  $\phi = -1.68 \pm 0.01$  rad.